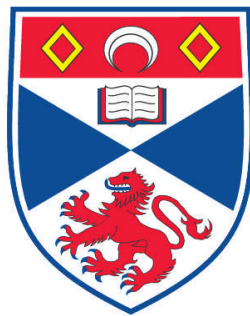


**STUDIES OF NOVEL BEAM SHAPES AND APPLICATIONS TO
OPTICAL MANIPULATION**

Jill E. Morris

**A Thesis Submitted for the Degree of PhD
at the
University of St. Andrews**



2010

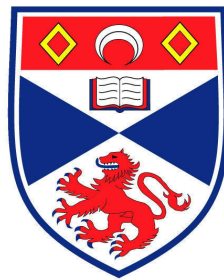
**Full metadata for this item is available in
Research@StAndrews:FullText
at:
<https://research-repository.st-andrews.ac.uk/>**

**Please use this identifier to cite or link to this item:
<http://hdl.handle.net/10023/1699>**

This item is protected by original copyright

Studies of novel beam shapes and applications to optical manipulation

Jill E Morris



University
of
St Andrews

A thesis submitted to the
University of St Andrews in
application for the degree of
Doctor of Philosophy

October 2010

Abstract

In this thesis an investigation into novel beams and optical manipulation is presented. Sculpting the phase profile of a Gaussian beam can result in the generation of a beam with unusual properties. Described in this thesis are optical vortices, Bessel beams and Airy beams. Additionally, optical manipulation was investigated using both novel beams and Gaussian beams with an emphasis on the use of a broad bandwidth laser source. The generation of multiple broadband optical trap sites was explored, and the transfer of orbital angular momentum from a broadband optical vortex to trapped microspheres was demonstrated.

An introduction to the thesis and an overview of laser sources used for optical manipulation is presented in Chapters 1 and 2. Chapters 3 and 4 detail the background of optical manipulation and novel beam shaping. In Chapter 5, an investigation into the generation of multiple broadband optical trap sites is presented. Chapter 6 details the use of a ‘white light’ optical vortex to transfer orbital angular momentum to trapped microspheres. Chapter 7 presents the results of an investigation carried out using a supercontinuum source to characterise the wavelength and spatial coherence dependence of the properties of an optical Airy beam. The use of a monochromatic laser to generate Bessel beams that propagate along curved trajectories is detailed in Chapter 8. Chapter 9 summarises the thesis and suggests future work.

Declaration

1. Candidate's declarations:

I, Jill Elizabeth Morris, hereby certify that this thesis, which is approximately 36,000 words in length, has been written by me, that it is the record of work carried out by me and that it has not been submitted in any previous application for a higher degree.

I was admitted as a research student in October 2006 and as a candidate for the degree of Doctor of Philosophy in October 2006; the higher study for which this is a record was carried out in the University of St Andrews between 2006 and 2010.

Date Signature of candidate

2. Supervisor's declaration:

I hereby certify that the candidate has fulfilled the conditions of the Resolution and Regulations appropriate for the degree of Doctor of Philosophy in the University of St Andrews and that the candidate is qualified to submit this thesis in application for that degree.

Date Signature of supervisor

3. Permission for electronic publication:

In submitting this thesis to the University of St Andrews I understand that I am giving permission for it to be made available for use in accordance with the regulations of the University Library for the time being in force, subject to any copyright vested in the work not being affected thereby. I also understand that the title and the abstract will be published, and that a copy of the work may be made and supplied to any bona fide library or research worker, that my thesis will be electronically accessible for personal or research use unless exempt by award of an embargo as requested below, and that the library has the right to migrate my thesis into new electronic forms as required to ensure continued access to the thesis. I have obtained any third-party copyright permissions that may be required in order to allow such access and migration, or have requested the appropriate embargo below.

The following is an agreed request by candidate and supervisor regarding the electronic publication of this thesis:

Access to printed copy and electronic publication of thesis through the University of St Andrews.

Date Signature of candidate

Date Signature of supervisor

Acknowledgements

I would first like to thank my supervisor Kishan Dholakia for this opportunity and for all of his help and support throughout my PhD (and during the several short projects that I undertook in his group as an undergraduate). I will be sad to leave such a wonderful research group after having been involved for so many years.

I would like to thank the people that I have worked with directly for their help and advice: Jörg Baumgartl, Tomáš Čížmár, Heather Dalgarno, Toni Carruthers, Michael Mazilu, Peter Reece, Pascal Fischer and Rob Marchington. I'd also like to thank everyone else in the group who gave help or advice at any stage, in particular Steve Lee and Martin Plöschner. Thanks also to Chris Leburn for help in the early stages of my PhD.

For all of the great coffee breaks and entertainment outside of the lab, thanks to: Fiona, Areti, Jörg, Sebastian, Anna Chiara, Ronan, Lani, Maria, Dave M^c, Peter S, Elisabetta and Janelle... Thanks also to Dave M, Gary, Steve H and Andrew B for many entertaining conversations and for helping to keep me sane. To my flatmates, Fiona and Keeley: it was great living with you guys, I will miss you both. To Zoe, Jo and Kirstin: thanks for all of the support, it's great to know you guys are always there (Belize, London, Oxford, Derry, Edinburgh - wherever 'there' may be).

I'd like to thank my boyfriend Mark for his unwavering support and encouragement from across the pond. To my family: thank you for all of the support you have given me over the years, I really couldn't have done this without you all.

Publications

J.E. Morris, A.E. Carruthers, M. Mazilu, P.J. Reece, T. Čižmár, P. Fischer and K. Dholakia. “Optical micromanipulation using supercontinuum Laguerre-Gaussian and Gaussian beams.” *Opt. Express*, **16** (14) 10117-10129 (2008).

J.E. Morris, M. Mazilu, J. Baumgartl, T. Čižmár and K. Dholakia. “Supercontinuum Airy beams.” SPIE annual meeting, *Proceedings of SPIE: laser beam shaping X*, **7430**, W1–W9 (2009).

J.E. Morris, M. Mazilu, J. Baumgartl, T. Čižmár and K. Dholakia. “Propagation characteristics of Airy beams: dependence upon spatial coherence and wavelength.” *Opt. Express*, **17** (15) 13236-13245 (2009).

J.E. Morris, T. Čižmár, H.I.C. Dalgarno, R.F. Marchington, F.J. Gunn-Moore and K. Dholakia. “Realization of curved Bessel beams: propagation around obstructions.” *Journal of Optics* (accepted 2010).

Conference presentations

J.E. Morris, A.E. Carruthers, M. Mazilu, P.J. Reece, T. Čižmár, P. Fischer and K. Dholakia. “Optical micromanipulation using supercontinuum Laguerre-Gaussian and Gaussian beams.” Photon’08, Herriot Watt university, Edinburgh, 2008 (Presentation).

J.E. Morris, M. Mazilu, J. Baumgartl, T. Čižmár and K. Dholakia. “Supercontinuum Airy beams.” SPIE: laser beam shaping X, conference centre, San Diego, 2009 (presentation).

Symbols

Unless otherwise stated, the following symbols have the meanings listed below:

A	Vector potential
a	Radius of a microsphere
a_0	Aperture coefficient
b_0	Deflection coefficient
c	Speed of light
D_E	Einstein diffusion coefficient
D_{lens}	Diameter of a lens
d_a	Diameter of an annulus used for Bessel beam generation
d_m	Diameter of a parabolic mirror
E	Electric field vector
F	Force
F_{grad}	Gradient force
F_{scat}	Scattering force
F_{drag}	Drag force
F_z	Axial force
f	Optical frequency
f_0	Corner frequency
f_{lens}	Focal length of a lens
f_{rate}	Frame rate of a camera
H	Magnetic field vector
h	Planck's constant
\hbar	$h/2\pi$
I	Intensity
i	$\sqrt{-1}$
J	Total orbital angular momentum of a field

\mathbf{J}_t	Total angular momentum of a field
J_m	Bessel function of order m
\mathbf{j}	Angular momentum density
k	Wavenumber
k_B	Boltzmann's constant
l	Azimuthal index of an optical vortex
l_c	Temporal coherence length
l_h	Side length of a hologram
M^2	Optical beam quality
m	Azimuthal index of a Bessel beam
N_r	Number of concentric bright rings in an optical vortex
N_{fr}	Video frame number
$N.A._{PM}$	Numerical aperture of a parabolic mirror
$N.A._L$	Numerical aperture of a lens
n_0	Refractive index of air
n_{lens}	Refractive index of a lens
n_m	Refractive index of the medium surrounding a microsphere
n_s	Refractive index of a microsphere
n_x	Refractive index of an axicon
P	Power
P_{scat}	Scattered power
P_{trap}	Power of a laser used in an optical trap
P_0	Total power of a laser beam
p	Linear momentum of a photon
Δp	Change in photon momentum
Q	Q value
R	Radius of curvature of the surface of a lens

$R(z)$	Radius of wavefront curvature
R_{lens}	Radius of a lens
R_m	Radius of curvature of a parabolic mirror
r	Radial co-ordinate
r_{obs}	Radius of obstruction
$r_{max I}(z)$	Radius of maximum intensity of an optical vortex
\mathbf{r}	Radius vector
\mathbf{S}	Poynting vector
$S_\lambda(\lambda)$	Power spectrum
T	Temperature
T_d	Distance from the centre of a microsphere to the sample chamber edge
t	Time
$U(r)$	Optical trapping potential
$u(x, y, z)$	Scalar field
V	Voltage
v_{fluid}	Velocity of fluid around a microsphere
W	Spectral density function
$w(z)$	Beam waist at position z
w_0	Beam waist at focus
w_{inc}	Incident beam waist on an axicon
w_{SLM}	Beam waist incident on an SLM
x	Cartesian co-ordinate
x_0	Characteristic length of an Airy beam in the x axis
y	Cartesian co-ordinate
y_0	Characteristic length of an Airy beam in the y axis
z	Cartesian co-ordinate
z_r	Rayleigh range
z_{max}	Maximum diffraction-free propagation distance of a Bessel beam

z_{\min}	Minimum reconstruction distance of a Bessel beam after an obstruction
α	Base angle of an axicon
α_p	Polarizability
β	Faxen correction
Δ	Deviation of spiralling or snaking Bessel beam from the optic axis
ε_0	Permittivity of free space
ϕ	Cylindrical co-ordinate
γ	Angle of wavevectors in a Bessel beam
γ_d	Direction cosine
γ_0	Friction coefficient
η	Viscosity of fluid around a microsphere
$\eta_{st}(t)$	Stochastic motion
φ	Maximal phase shift across a hologram
κ	Trap stiffness value
Λ	Period of a grating
λ	Wavelength
μ_0	Permeability of free space
μ_λ	Spectral degree of coherence
π	3.14159265...
$\rho(x)$	Position probability
ρ_{laser}	Laser power optical density
σ_{sc}	Scattering cross-section
σ_μ	Spatial coherence length
τ	Total torque acting on a microsphere
τ_{drag}	Drag torque
τ_{OAM}	Torque resulting from orbital angular momentum
Ω	Rotation rate of microspheres in an optical vortex

ω_r

Angular velocity of a rotating object

$\psi(r)$

Phase imposed on a beam by a hologram displayed on an SLM

Acronyms

2D	Two dimensional
3D	Three dimensional
CCD	Charged coupled device
EM	Electromagnetic
FWHM	Full width half maximum
IR	Infrared
LCOS	Liquid crystal on silicon
LED	Light emitting diode
LG	Laguerre Gaussian
N.A.	Numerical aperture
NADH	Nicotinamide adenine dinucleotide
Nd:YAG	Neodymium-doped yttrium aluminium garnet
Nd:YLF	Neodymium-doped yttrium lithium fluoride
OAM	Orbital angular momentum
OCT	Optical coherence tomography
PDMS	Polydimethylsiloxane
QPD	Quadrant photodiode
SAM	Spin angular momentum
SC	Supercontinuum
SLM	Spatial light modulator
SnBB	Snaking Bessel beam
SpBB	Spiralling Bessel beam
UV	Ultraviolet
WLSI	White light scanning interferometry

Contents

1. Introduction

1.1 Introduction.....	1
1.2 Optical manipulation.....	2
1.3 Novel beams.....	5
1.4 Light sources for optical manipulation.....	7
1.5 Thesis outline.....	8

2. Light sources for optical manipulation applications

2.1 Synopsis.....	12
2.2 Introduction.....	12
2.3 Light sources for optical manipulation.....	13
2.4 The supercontinuum source.....	15
2.4.1 Properties.....	15
2.4.2 Applications.....	18
2.5 Conclusion.....	23

3. Optical manipulation: an introduction

3.1 Synopsis.....	28
3.2 Optical manipulation: an explanation.....	29
3.3 Characterising an optical trap.....	35
3.3.1 Introduction to Q values.....	35
3.3.2 Trap stiffness.....	37
3.3.2.1 Power spectrum method.....	38
3.3.2.2 Optical potential analysis method.....	42
3.4 Review of experiments.....	43
3.5 Conclusion.....	45

4. Novel beam shaping

4.1 Synopsis.....	47
4.2 Optical vortices.....	48
4.2.1 What are optical vortices?.....	48
4.2.2 Angular momentum.....	50

4.2.2.1 Spin angular momentum.....	50
4.2.2.2 Orbital angular momentum.....	52
4.2.3 Generating optical vortices.....	54
4.3 Bessel beams.....	56
4.3.1 Introduction to Bessel beams.....	56
4.3.2 Generating Bessel beams.....	57
4.4 Airy beams.....	61
4.4.1 Introduction to Airy beams.....	61
4.4.2 Generating an Airy beam.....	62
4.4.3 Properties of Airy beams.....	64
4.5 The spatial light modulator.....	66
4.6 Generating novel beams using a spatial light modulator.....	68
4.7 Broadband novel beams.....	70
4.8 Conclusion.....	71

5. Optical manipulation using a supercontinuum source

5.1 Synopsis and motivation.....	75
5.2 Single beam optical manipulation using a supercontinuum source.....	77
5.2.1 Illuminating the sample.....	77
5.2.2 Determining the Q value of an optical trap.....	81
5.2.3 Optical tweezing of silica spheres.....	83
5.2.4 Optical trapping of polymer spheres.....	87
5.3 Multiple beam optical manipulation.....	89
5.3.1 Using a spatial light modulator for optical manipulation with a supercontinuum source.....	89
5.3.2 The twin trap.....	90
5.4 Multiple optical manipulation using a parabolic micromirror array.....	96
5.4.1 Introduction.....	96
5.4.2 The parabolic micromirror array.....	97
5.4.3 Broadband multiple optical manipulation using a parabolic micromirror array.....	98
5.5 Discussion.....	101

6. Transfer of orbital angular momentum from a ‘white light’ optical vortex to trapped microspheres	
6.1 Synopsis and motivation.....	106
6.2 Transfer of orbital angular momentum.....	107
6.2.1 Experimental setup and method.....	107
6.2.2 Results.....	111
6.3 Discussion.....	113
7. Propagation characteristics of Airy beams	
7.1 Synopsis and motivation.....	116
7.2 Investigating the properties of Airy beams.....	117
7.2.1 Experimental setup and methods.....	117
7.2.2 Results.....	121
7.3 Discussion.....	126
8. Characterisation of spiralling and snaking Bessel beams	
8.1 Synopsis and motivation.....	129
8.2 Background to spiralling and snaking Bessel beams.....	130
8.3 Experimental realisation of spiralling and snaking Bessel beams.....	133
8.3.1 Experimental setup.....	133
8.3.2 Spiralling Bessel beams.....	134
8.3.3 Snaking Bessel beams.....	138
8.4 Discussion.....	142
9. Summary and outlook	
9.1 Summary and outlook.....	145
Appendix A	
A.1 Wavefront correction.....	A.1
Appendix B	
B.1 Laguerre Gaussian beam propagation.....	B.1
B.2 Torques acting on microspheres in a Laguerre Gaussian beam.....	B.4
Appendix C	
C.1 Coherent Airy beam propagation.....	C.1
C.2 Partially coherent Airy beam propagation.....	C.4

Chapter 1

Introduction

1.1 Introduction

The invention of the laser¹ in May 1960 started a wave of excitement as the research field of laser physics was born. As the vast scope of potential applications for this device became clear, laser physics began to branch out into many new areas, one of the most significant of which was optical manipulation. This area focuses on the use of light to manipulate matter. The basis for this actually dates back to the 20th century when Einstein postulated that light can be thought of as packets of energy called photons. De Broglie then postulated that each photon carries momentum and that the magnitude of this momentum depends on the wavelength of the photon. De Broglie determined that the momentum of a photon is equal to h/λ , where h is Planck's constant and λ is the wavelength of the photon.

The collective momentum of photons emerging from a laser source is significant enough to exert a small force, on the order of picoNewtons, on a microscopic object. This knowledge has been used to develop techniques to optically 'grasp' and manipulate transparent microscopic objects²⁻⁴ and even nanometer scale objects.⁵ Also, a laser emitting at a wavelength that is absorbed by an object allows the ablation of the object through heating. The versatility of the laser source therefore allows micro-surgery to be

performed on individual cells. Cellular components can be grasped, moved, cut and probed.⁶ By acting as a force transducer for picoNewton forces, similar to the way a torque wrench is used, optical manipulation can also be used to gain information about the hydrodynamics of single molecules.⁷⁻¹⁰ Information about how single molecules behave can give medically valuable insight into biological processes such as DNA transcription⁸ and protein folding.¹¹

Using holographic techniques,¹² it is now possible to optically manipulate multiple objects simultaneously¹³⁻¹⁶ or generate novel beams capable of rotating objects.^{17,18} The use of novel laser beams to rotate microscopic objects has led to the invention of an optical pump¹⁹ used to channel fluid through microfluidic devices. The ability to generate controllable fluid flow in microfluidic devices is essential for the development of lab-on-a-chip devices. Additionally, by measuring the forces and torques acting on an optically rotating object, information can be gathered about the fluid environment surrounding the object using a technique called microrheology.^{20,21} Novel beams can also be used to optically sort objects that have different intrinsic physical properties.²² This is a particularly promising technique because it could be used to sort biological items to aid in the analysis of medical samples. It is even possible to generate novel beams that do not propagate in a straight line.^{23,24} These beams can use photon momentum (radiation pressure) to optically ‘push’ microscopic objects in a curved path.²⁵

In this chapter, there is an introduction to optical manipulation techniques and a brief introduction to the novel beam shapes that are relevant to this thesis. The supercontinuum source is introduced, and the thesis outline will be presented.

1.2 Optical manipulation

A large scale example of light exerting a force on an object is that of a comet whose dust particles are optically ‘pushed’ by radiation pressure from the Sun’s light. The use of laser light to manipulate objects is a scaled down example of the same idea. Laser light has a high degree of coherence, good directionality and a high intensity. All of these properties are what make it possible to use laser light to manipulate objects. Arthur

Ashkin carried out the initial work. He realised that when photons interact with an object they transfer some momentum to that object. The pressure exerted on the object is called radiation pressure. He investigated how radiation pressure could be used to influence microscopic objects. In 1970, Ashkin began by focusing a laser into a solution of latex microspheres immersed in water.²⁶ The spheres were pushed in the direction of beam propagation by radiation pressure from the laser light. This technique has become known as optical guiding and is illustrated in Figure 1.2(a). In the same paper,²⁶ Ashkin presented a way to use counter-propagating laser beams to generate an optical potential well to trap microspheres. He used the counter-propagating beams to balance the radiation pressure acting on the microspheres. This arrangement was termed a ‘dual beam trap,’ see Figure 1.2(b). In both the optical guiding arrangement and the dual beam trap, Ashkin noticed that the microspheres were drawn into the most intense region of the beam, i.e. the beam’s propagation axis. The Gaussian profile of the laser beam gives rise to an intensity gradient in the transverse plane. For the case where an object has a higher refractive index than the surrounding medium, Figure 1.1 illustrates how the light rays are refracted through a transparent object. The change in direction of the photons as a result of refraction results in a change in their momentum. From Newton’s laws it is known that momentum is related to force, and that when a force is exerted on a body, a force of equal magnitude acting in the opposite direction must result. The sphere exerts a force on the photons as they are refracted, so the photons must exert a force on the sphere. In the case presented in Figure 1.1, the change in direction of the light rays results in a force that draws the sphere towards the most intense part of the beam. This force is known as the gradient force. A more detailed explanation is given in Chapter 3.

Ashkin then aimed to develop a method to optically confine an object in just a single laser beam. His first attempt became known as ‘optical levitation.’²⁷ A beam propagating vertically upwards was used to balance the force of gravity acting on a glass microsphere, see Figure 1.2(c). Then came probably the most significant discovery: optical tweezers. By tightly focusing a laser beam, the gradient force can be used to confine an object in the axial direction as well as in the transverse plane.²⁸ Figure 1.2(e) illustrates the optical tweezers geometry whilst Figure 1.2(f) illustrates an inverted optical tweezers geometry.

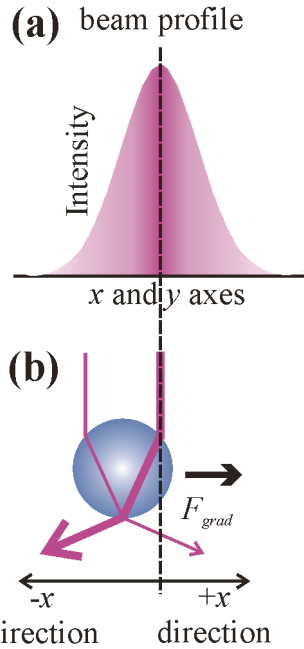


Figure 1.1. Image (a) depicts the transverse intensity profile of a Gaussian beam. Image (b) depicts the refraction of light rays from a Gaussian beam through a microsphere. The thickness of the line indicates the intensity of the light ray. The net force acting on the object, F_{grad} , draws it towards the centre of the Gaussian beam.

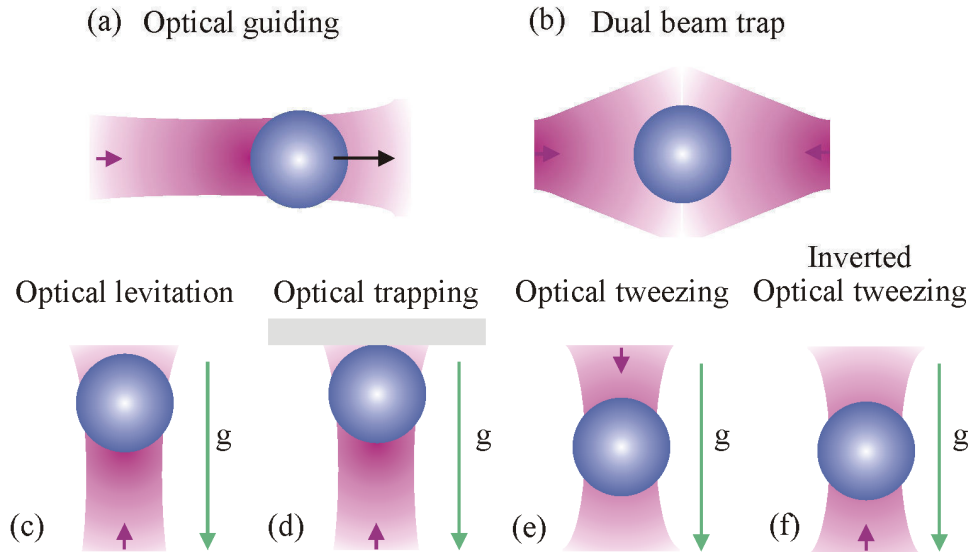


Figure 1.2. The images above illustrate the different types of optical manipulation. Gravity is denoted by 'g' where it is necessary to define it. The short pink arrow indicates the direction in which the beam is propagating. If the sphere is travelling in a particular direction then this is indicated by a black arrow. (a) illustrates a sphere pushed along the beam axis by radiation pressure (optical guiding). (b) depicts two counter propagating beams. (c) illustrates that gravity can be balanced by the radiation pressure from a beam propagating upwards. (d) illustrates the 2D confinement of a microsphere using a laser beam (the axial confinement in this case is due to a physical barrier, but the buoyancy force could be used instead if the geometry of the trap was inverted). (e) illustrates the 3D confinement of a microsphere using a tightly focused laser beam. Axial confinement is achieved in this case because of the high axial intensity gradient caused by the tight focusing. (f) illustrates the 3D confinement of a microsphere using a tightly focused laser beam but in the 'inverted' optical tweezers arrangement.

If the beam is not focused tightly enough, the axial gradient force is not sufficient to confine the object and the object is only confined in the transverse plane. This situation is known as optical trapping and is illustrated in Figure 1.2(d). In this case, confinement in the axial direction can be achieved using a solid surface, such as a coverslide, or by balancing the radiation pressure force with the buoyancy of the object in a liquid.

The opportunity to study biological processes in a quantifiable way was not lost on Ashkin. Within a few years of his big discovery he used optical tweezers to manipulate filaments of cytoplasm inside a cell giving insight into its viscoelastic properties.²⁹ One of the great advantages of optical manipulation is that it is non-invasive. An object can be isolated and probed without any physical contact.

1.3 Novel beams

Although optical manipulation using basic Gaussian beams has resulted in many applications, the scope for innovation expands dramatically with the addition of novel optical beam shapes: beams that are not only able to confine objects, but rotate them, beams with unusual transverse intensity profiles that are capable of optically sorting objects²² and even beams that do not propagate in a straight line.^{23,24} Such discoveries have turned the world of optical manipulation upside down. The possibilities are seemingly endless.

Three of these novel beams will now be described. The Laguerre Gaussian (LG) beam, or optical vortex, has, in general, an annular transverse intensity profile. It has a spiral phase front with a $2\pi l$ phase shift around the circumference of the beam, where l is an integer. Just like the Gaussian beam, the optical vortex is able to draw objects with a higher refractive index than their surroundings into the most intense region of light. Objects that are small compared to the size of the beam become trapped off-axis in the bright ring of the beam. Objects that are large compared to the size of the beam are trapped on-axis. An optical vortex has a spiral phase front which gives rise to an azimuthal component of the Poynting vector $\mathbf{S} \propto \mathbf{E} \times \mathbf{B}$. Therefore, the momentum also has an azimuthal component. This momentum is called ‘orbital angular momentum.’ Note that orbital angular

momentum is distinct from spin angular momentum, which is related to the polarization of the light field. Orbital angular momentum can be transferred from an optical vortex to objects to make them rotate.^{17,30,31} The transverse intensity profile of an optical vortex is shown in Figure 1.3(a).

Bessel beams have a transverse intensity profile based on the family of Bessel functions. A zero order Bessel beam has a transverse intensity profile with a bright central core surrounded by bright concentric rings. Remarkably, an experimentally generated Bessel beam can propagate seemingly unaffected by diffraction for a limited distance. Unlike Gaussian beams, the transverse intensity profile of a Bessel beam does not spread as the beam propagates over a finite distance. One of the most notable qualities of the Bessel beam is that it can reconstruct around obstructions placed in the beam path. This property makes the beam useful for stacking multiple objects along the beam's central core.³² The transverse intensity profile of a zero order Bessel beam is shown in Figure 1.3(b).

The final novel beam that is relevant to this thesis is the Airy beam, which has a transverse intensity profile based on the Airy function as illustrated in Figure 1.3(c). Like the Bessel beam, the Airy beam is 'non-diffracting' and can reconstruct around obstructions. But this beam has an even more surprising ability: it propagates along a parabolic path. The Airy beam has been used for optical manipulation. It can draw objects into the beam's brightest lobe and push them along a parabolic trajectory. This has proved useful for optical clearing applications.²⁵ More detailed information about all of the beams introduced in this section is given in Chapter 4.

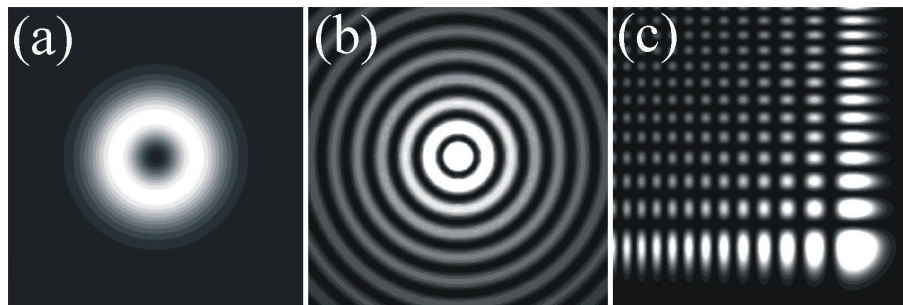


Figure 1.3. The simulated transverse intensity profiles of an optical vortex (a), a Bessel beam (b) and an Airy beam (c) are shown. Note that when the parameters of the beams are changed, the transverse intensity profile will also change.

1.4 Light sources for optical manipulation

Narrowband lasers are the most common light sources used for optical manipulation. This is because they can be easily accessible, relatively inexpensive and often have a high beam quality. When using lasers for the optical tweezing of biological items, the lasing wavelength must be carefully selected to minimise damage to the item. The so called ‘therapeutic window’ of tweezing wavelengths for biological items is approximately³³ 700nm - 1064nm. In this case, the ‘therapeutic window’ is the range of wavelengths that can be used to optically tweeze a biological item and maximise the chance of survival of the item. Other factors also affect the chance of survival for the biological item such as the intensity of the beam. However, for imaging applications that use light of very low intensity, damage to tissue is minimal even at short wavelengths. However, light has the deepest penetration into tissue within the wavelength range 800nm – 1200nm. Short wavelength light scatters from the tissue and does not penetrate deeply into the tissue. For spectroscopy applications, the use of a broadband laser can be advantageous. For many of the experiments in this thesis a laser with a broad bandwidth known as a supercontinuum (SC) source is used. The supercontinuum source has some qualities that make it distinct from any other laser source. The most notable quality is the extremely broad bandwidth. The source used during this research offers access to wavelengths ranging from 464nm to 1750nm. Additionally, the supercontinuum source has a very short temporal coherence length whilst maintaining a high degree of spatial coherence.

The short temporal coherence length of the supercontinuum beam allows it to be used for applications such as optical binding studies³⁴ where interference effects are problematic. The imaging technique of optical coherence tomography has also benefited from the short temporal coherence length of this source.³⁵⁻³⁷ Furthermore, the broad bandwidth of the supercontinuum source has been used to develop unique microscopy techniques^{38,39} and optical manipulation applications, such as the simultaneous trapping and spectroscopy of individual objects^{40,41} and aerosols⁴² using only a single tightly focused beam. Also, the broad bandwidth of the supercontinuum source can facilitate extended optical guiding distances of microparticles.⁴³ In the field of fluorescence microscopy, Li *et al.*⁴⁴ have

developed a technique capable of identifying precancerous cells using a supercontinuum source.

Gaussian beams have been used for optical manipulation and can often achieve the three dimensional confinement of a single object. This is extremely useful for many applications, but in some cases the manipulation of multiple objects or optical guiding over long distances is required. The transverse intensity profile of a focused Gaussian beam spreads rapidly away from the focus, and the optical gradient forces diminish as the beam spreads. This limits the range over which the beam can manipulate objects. The generation of novel beams with unique properties allows for more applications to be developed.

Novel beam shapes generated using a supercontinuum source have allowed investigations into the fundamentals of physics, particularly into the roles that wavelength and coherence play in affecting the properties of novel beams.⁴⁵ More details about the supercontinuum source, and other laser sources used for optical manipulation, are given in Chapter 2 along with a review of supercontinuum source applications.

1.5 Thesis outline

This thesis describes an investigation into the forces involved in optical manipulation and the characterisation of the properties of novel beams. Chapter 2 outlines some of the laser sources that have been used for optical manipulation so far, with particular attention given to the supercontinuum source. Chapter 3 details the physics behind optical manipulation, and Chapter 4 further explores the properties of the novel beams that were introduced above. Chapters 5 - 8 present the experiments carried out during this research.

I began by investigating the forces involved in a broadband optical trap and then used holographic techniques to generate multiple broadband optical trap sites. Chapter 5 describes the process used to generate broadband optical traps with a computer generated hologram. I also used a micromirror array integrated into a microfluidic device to generate multiple broadband optical trap sites. Holographic techniques were then

extended to generate a broadband optical vortex. The transfer of orbital angular momentum from the broadband optical vortex to an ensemble of microspheres was demonstrated. This experiment is presented in Chapter 6. Chapter 7 describes the use of a supercontinuum source to investigate the effect of wavelength and spatial coherence on the properties of an optical Airy beam. The parabolic propagation of the Airy beam encouraged an investigation into the possibility of generating a Bessel beam that deviates from a straight line propagation path. I used a narrowband laser to generate Bessel beams that propagate along snaking and spiralling paths. I characterised the properties of these beams and demonstrated that the snaking Bessel beam can propagate around obstructions placed on the optic axis. The experimental procedure and results are presented in Chapter 8. Chapter 9 concludes this thesis.

References

1. Maiman, T. H. Optical and microwave-optical experiments in Ruby. *Physical Review Letters* **4**, 564-566 (1960).
2. Neuman, K. C. & Block, S. M. Optical trapping. *Review of Scientific Instruments* **75**, 2787-2809 (2004).
3. Dholakia, K., Reece, P. & Gu, M. Optical micromanipulation. *Chemical Society Reviews* **37**, 42-55 (2008).
4. Grier, D. G. A revolution in optical manipulation. *Nature* **424**, 810-816 (2003).
5. Dienerowitz, M., Mazilu, M. & Dholakia, K. Optical manipulation of nanoparticles: a review. *Journal of Nanophotonics* **2**, 021875 (2008).
6. Berns, M. W., Tadir, Y., Liang, H. & Tromberg, B. Laser scissors and tweezers. *Methods in Cell Biology* **55**, 71-98 (1998).
7. Mehta, A. D., Rief, M., Spudich, J. A., Smith, D. A. & Simmons, R. M. Single-molecule biomechanics with optical methods. *Science* **283**, 1689-1695 (1999).
8. Bustamante, C., Bryant, Z. & Smith, S. B. Ten years of tension: single-molecule DNA mechanics. *Nature* **421**, 423-427 (2003).
9. Kuo, S. C. & Sheetz, M. P. Force of single kinesin molecules measured with optical tweezers. *Science* **260**, 232-234 (1993).
10. Lang, M. J., Fordyce, P. M., Engh, A. M., Neuman, K. C. & Block, S. M. Simultaneous, coincident optical trapping and single-molecule fluorescence. *Nature methods* **1**, 133-139 (2004).
11. Schlierf, M., Berkemeier, F. & Rief, M. Direct observation of active protein folding using lock-in force spectroscopy. *Biophysical Journal* **93**, 3989-3998 (2007).
12. Curtis, J. E., Koss, B. A. & Grier, D. G. Dynamic holographic optical tweezers. *Optics Communications* **207**, 169-175 (2002).

13. Dufresne, E. R. & Grier, D. G. Optical tweezer arrays and optical substrates created with diffractive optics. *Review of Scientific Instruments* **69**, 1974-1977 (1998).
14. Liesener, J., Reicherter, M., Haist, T. & Tiziani, H. J. Multi-functional optical tweezers using computer-generated holograms. *Optics Communications* **185**, 77-82 (2000).
15. Melville, H. et al. Optical trapping of three-dimensional structures using dynamic holograms. *Optics Express* **11**, 3562-3567 (2003).
16. Leach, J. et al. 3D manipulation of particles into crystal structures using holographic optical tweezers. *Optics Express* **12**, 220-226 (2004).
17. He, H., Friese, M. E. J., Heckenberg, N. R. & Rubinsztein-Dunlop, H. Direct observation of transfer of angular momentum to absorptive particles from a laser beam with a phase singularity. *Physical Review Letters* **75**, 826-829 (1995).
18. Garcés-Chavez, V., Volke-Sepulveda, K., Chavez-Cerda, S., Sibbett, W. & Dholakia, K. Transfer of orbital angular momentum to an optically trapped low-index particle. *Physical Review A* **66** (2002).
19. Ladavac, K. & Grier, D. Microoptomechanical pumps assembled and driven by holographic optical vortex arrays. *Opt. Express* **12**, 1144-1149 (2004).
20. Yao, A., Tassieri, M., Padgett, M. & Cooper, J. Microrheology with optical tweezers. *Lab Chip* **9**, 2568-75 (2009).
21. Bishop, A. I., Nieminen, T. A., Heckenberg, N. R. & Rubinsztein-Dunlop, H. Optical microrheology using rotating laser-trapped particles. *Physical Review Letters* **92**, 198104 (2004).
22. Paterson, L. et al. Light-induced cell separation in a tailored optical landscape. *Applied Physics Letters* **87** (2005).
23. Berry, M. V. & Balazs, N. L. Non-spreading wave packets. *American Journal of Physics* **47**, 264-267 (1979).
24. Siviloglou, G. A., Broky, J., Dogariu, A. & Christodoulides, D. N. Observation of accelerating airy beams. *Physical Review Letters* **99** (2007).
25. Baumgartl, J., Mazilu, M. & Dholakia, K. Optically mediated particle clearing using Airy wavepackets. *Nat. Photon* **2**, 675-678 (2008).
26. Ashkin, A. Acceleration and trapping of particles by radiation pressure. *Physical Review Letters* **24**, 156 -159 (1970).
27. Ashkin, A. & Dziedzic, J. M. Optical levitation by radiation pressure. *Applied Physics Letters* **19**, 283-285 (1971).
28. Ashkin, A., Dziedzic, J. M., Bjorkholm, J. E. & Chu, S. Observation of a single-beam gradient force optical trap for dielectric particles. *Optics Letters* **11**, 288-290 (1986).
29. Ashkin, A. & Dziedzic, J. M. Internal cell manipulation using infrared laser traps. *Proceedings of the National Academy of Sciences of the United States of America* **86**, 7914-7918 (1989).
30. Paterson, L. et al. Controlled rotation of optically trapped microscopic particles. *Science* **292**, 912-914 (2001).
31. Simpson, N. B., Dholakia, K., Allen, L. & Padgett, M. J. Mechanical equivalence of spin and orbital angular momentum of light: An optical spanner. *Optics Letters* **22**, 52-54 (1997).

32. Arlt, J., Garces-Chavez, V., Sibbett, W. & Dholakia, K. Optical micromanipulation using a Bessel light beam. *Optics Communications* **197**, 239-245 (2001).
33. Stevenson, D. J., Gunn-Moore, F. & Dholakia, K. Light forces the pace: optical manipulation for biophotonics. *J Biomed Opt* **15**, 041503.
34. Gherardi, D. M., Carruthers, A. E., Cizmar, T., Wright, E. M. & Dholakia, K. A dual beam photonic crystal fiber trap for microscopic particles. *Applied Physics Letters* **93** (2008).
35. Huang, D. et al. Optical coherence tomography. *Science* **254**, 1178-1181 (1991).
36. Aguirre, A. D. et al. Continuum generation in a novel photonic crystal fiber for ultrahigh resolution optical coherence tomography at 800 nm and 1300 nm. *Optics Express* **14**, 1145-1160 (2006).
37. Cimalla, P., Walther, J., Mehner, M., Cuevas, M. & Koch, E. Simultaneous dual-band optical coherence tomography in the spectral domain for high resolution in vivo imaging. *Optics Express* **17**, 19486-19500 (2009).
38. Shi, K. B., Li, P., Yin, S. Z. & Liu, Z. W. Chromatic confocal microscopy using supercontinuum light. *Opt. Express* **12**, 2096-2101 (2004).
39. Shi, K. B., Nam, S. H., Li, P., Yin, S. Z. & Liu, Z. W. Wavelength division multiplexed confocal microscopy using supercontinuum. *Optics Communications* **263**, 156-162 (2006).
40. Li, P., Shi, K. B. & Liu, Z. W. Manipulation and spectroscopy of a single particle by use of white-light optical tweezers. *Optics Letters* **30**, 156-158 (2005).
41. Li, P., Shi, K. B. & Liu, Z. W. Optical scattering spectroscopy by using tightly focused supercontinuum. *Optics Express* **13**, 9039-9044 (2005).
42. Guillon, M., Dholakia, K. & McGloin, D. Optical trapping and spectral analysis of aerosols with a supercontinuum laser source. *Optics Express* **16**, 7655-7664 (2008).
43. Fischer, P. et al. Enhanced optical guiding of colloidal particles using a supercontinuum light source. *Optics Express* **14**, 5792-5802 (2006).
44. Li, D., Zheng, W. & Qu, J. A. Y. Two-photon autofluorescence microscopy of multicolor excitation. *Optics Letters* **34**, 202-204 (2009).
45. Fischer, P. et al. White light propagation invariant beams. *Optics Express* **13**, 6657-6666 (2005).

Chapter 2

Light sources for optical manipulation applications

2.1 Synopsis

In this chapter, the properties of narrowband, pulsed and broad bandwidth light sources are compared for the case of optical manipulation. The use of these different sources for optical manipulation applications is discussed, and the relevance of the lasing wavelength for the optical manipulation of biological items is explained. More is then discussed about the supercontinuum source. This is a broad bandwidth source used for many of the experiments presented in this thesis. Finally, there is a review of some of the applications of the supercontinuum source.

2.2 Introduction

This section focuses on the properties of different types of light sources. Firstly, the bandwidth of different light sources can vary greatly. For a narrowband source such as a helium-neon laser, the spectral bandwidth¹ is typically 0.0019nm. For a pulsed laser the bandwidth is significantly larger. For example, a titanium-sapphire laser with a pulse duration of about 10fs (1×10^{-14} seconds) has a bandwidth² of 90nm full width half

maximum (FWHM). A supercontinuum source has a bandwidth that much exceeds even that of the shortest pulses that can be produced today. The bandwidth of the supercontinuum source used in this thesis is $\sim 1286\text{nm}$ (464-1750nm), which is more than ten times the bandwidth of the aforementioned pulsed titanium-sapphire laser.

The coherence properties of narrowband, pulsed and broad bandwidth light sources also vary. A helium-neon laser can have a temporal coherence length on the order of metres. Fischer *et al.*² carried out an investigation into the temporal coherence length, l_c , of a range of other sources. This investigation included a superluminescent diode, which is a diode laser operating without stimulated emission. Such a source has a broad bandwidth and a short temporal coherence length. They found that a superluminescent diode has a temporal coherence length of around $46\mu\text{m}$, a pulsed titanium-sapphire laser has $l_c \approx 6\mu\text{m}$ and a halogen bulb has $l_c \approx 2\mu\text{m}$. A supercontinuum source has the shortest temporal coherence length of all of these sources with $l_c < 1\mu\text{m}$.

2.3 Light sources for optical manipulation

Optical manipulation was initially carried out using a narrowband laser by Ashkin as described in Chapter 1. In fact, early optical manipulation experiments almost exclusively used continuous wave sources. There are several reasons why this is the case. One reason is simply that narrowband, continuous wave lasers are more readily available. Another reason is that the forces involved in optical manipulation result from the average power of the source. If a pulsed laser source is used, the magnitude of the optical forces acting on the object depends only on the average power and not on the peak power of the pulses. Therefore, the use of a pulsed source does not necessarily increase the power available for optical manipulation.

However, pulsed lasers have found a place in optical manipulation. The use of short pulses opens up the option of exploiting nonlinear effects. For example, it is possible to induce two-photon fluorescence in an object using the same laser that is simultaneously manipulating that object.³ This technique can be used to track the physiological changes of biological cell components using PH sensitive fluorescent tags.⁴ Although two-photon

fluorescence has been induced in an optical tweezers setup using a continuous wave source,⁴ the use of a pulsed source enhances the fluorescence signal because of the high peak power available. Similarly, second harmonic generation can be induced in an object using a continuous wave source,⁵ but again the use of pulses greatly enhances the signal obtained.⁶

Even so, there are cases when the use of a pulsed laser is detrimental and a continuous wave source is better employed. Biological items are often damaged by the high peak power of pulsed lasers. Therefore, it is often better to employ a continuous wave source in cases where it is important to minimize the damage to biological items.⁷ The wavelength of the source used to manipulate biological items also affects the impact of a procedure. For cells to survive the optical manipulation process, the laser wavelength must be within a certain range known as the ‘therapeutic window.’ For the optical manipulation of biological cells, the use of wavelengths below ~700nm increases the likelihood of cell damage.⁸ The therapeutic window has a range of about 700nm - 1064nm. This is the wavelength range where water and proteins have the lowest absorption coefficients, thus reducing heating and damage to the cells and cellular components. Figure 2.1 is a graph of the absorption coefficients for water, deoxyhemoglobin and oxyhemoglobin. It is clear that the absorption is lowest around the therapeutic window. An investigation was carried out into the efficiency of cloning cells after the cell had been optically manipulated.⁹ It was found that cells manipulated using a laser wavelength between 950nm - 990nm gave the best cloning efficiency.

Common lasers used in continuous wave mode for the optical manipulation of biological items are¹⁰ Nd:YAG with a wavelength of 1064nm or 1320nm; Nd:YLF with a wavelength of 1047nm or 1053nm; diode lasers, which have an available wavelength range of <400nm up to the infrared, and titanium-sapphire lasers, which are tunable between ~700nm - 1100nm. Of these, diode lasers are the cheapest by far, but the power is low and the quality of the beam must be improved using circularisation optics. For some optical manipulation applications, the use of a broad bandwidth source can be advantageous. In cases where the interference of waves is a problem, a source with a

This illustration of the absorption coefficients of water, Hb and HbO₂ is unavailable due to copyright restrictions.

Figure 2.1. The absorption coefficients of water, deoxyhemoglobin (Hb) and oxyhemoglobin (HbO₂) are shown. The therapeutic window lies at wavelengths of ~700nm - 1064nm, where the absorption is lowest. Image replicated from reference [10].¹⁰

broad bandwidth, and therefore low temporal coherence, can reduce these interference effects. For example, counter-propagating beams can be used to manipulate multiple objects. The refocusing of the counter-propagating beams through trapped objects results in the generation of new trap sites where other objects can be trapped. This effect is called optical binding.¹¹ Interference effects between the counter-propagating beams are detrimental to optical binding investigations and the use of a broad bandwidth source can help to reduce the interference effects.¹² The supercontinuum source is an ideal broad bandwidth source for use in optical manipulation studies. Unlike other broad bandwidth sources such as halogen bulbs or superluminescent diodes, the supercontinuum source can produce a high power, broad bandwidth beam with good directionality and a high degree of spatial coherence.

2.4 The supercontinuum source

2.4.1 Properties

The supercontinuum source is a broad bandwidth source with good spatial coherence but low temporal coherence. The source used during this research has a bandwidth of approximately 1300nm and a temporal coherence length less than 1 μ m. The high degree of spatial coherence gives rise to good beam directionality and the ability to tightly focus the beam. The output beam is pulsed with a repetition rate of about 40MHz. The duration

of the pulses is between 100ps – 200ps. Due to the way the supercontinuum is generated, the exact repetition rate and pulse duration varies. It should also be noted that the power spectrum of the supercontinuum beam is not uniform. However, the unusual properties of the supercontinuum source make it a useful tool for imaging, optical manipulation and spectroscopy applications, just to name a few. Some of the applications of the supercontinuum source are reviewed in the next section.

The extremely broad bandwidth of the supercontinuum source requires that all wavelength dependent effects are taken into account in the experimental environment. For example, chromatic aberration occurs when focusing a broad bandwidth beam. This effect is a result of the wavelength dependent focal length of a lens. Equation 2.1 relates the wavelength of light to the focal length of the lens,¹³

$$f_{lens}(\lambda) = \frac{R}{n(\lambda) - 1}, \quad (2.1)$$

where R is the radius of curvature of the lens surface and $n(\lambda)$ is the wavelength dependent refractive index described by Sellmeier's equation.¹⁴ Chromatic aberration can be a particular problem for optical tweezing applications since a tightly focused beam is required for 3D optical confinement. However, the elongated focal region can be an advantage for the optical guiding of objects as discussed in the next section.

As a result of the large bandwidth of the source, the transverse intensity profile of a focused supercontinuum beam is not Gaussian. The non-Gaussian focus arises because the individual wavelength components focus to spots with different beam waists. Throughout this research, the full width half maximum value of the supercontinuum spot was measured to determine the size of the beam because the transverse beam profile is not Gaussian. The intensity profile of a broad bandwidth beam can be determined using Equation 2.2, where $S_\lambda(\lambda)$ is the power spectrum and $w(z, \lambda)$ is the beam waist for each wavelength at position z along the propagation axis.¹³

$$I(r, z) = \sum_{\lambda} S_{\lambda}(\lambda) \cdot I_{\lambda}(r, z) = \sum_{\lambda} S_{\lambda}(\lambda) \cdot \frac{2}{\pi w^2(z, \lambda)} \cdot \exp\left(-2\left(\frac{r}{w(z, \lambda)}\right)^2\right) \quad (2.2)$$

There are several ways to generate a supercontinuum source output. The most versatile method is to couple the beam from a pulsed laser source into a photonic crystal fibre. A photonic crystal fibre has a central core surrounded by a structure of air holes that run the length of the fibre. Photonic crystal fibres used for supercontinuum generation have a solid core in which nonlinear broadening can occur. In many cases the solid core is made of silica,¹⁵ but other materials such as ZBLAN glass¹⁶ (which is composed of zirconium, barium, lanthanum, aluminium and sodium fluorides) have also been used. Altering the size, pattern and spacing of the microstructured air holes allows control of the fibre's properties. Nonlinear effects such as self phase modulation, four wave mixing, Raman scattering and soliton fission occur in the core of the fibre as the pulses propagate through. Such nonlinear effects broaden the pulses to produce a supercontinuum beam at the output of the fibre. More information about the nonlinear effects can be found in Boyd, 'Nonlinear Optics.'¹⁷

It is interesting to note that other types of broadband sources can also be used to produce a spatially coherent source of light. A small pinhole placed in front of a halogen bulb results in a spatially coherent beam. Additionally, any broadband source that is coupled into a fibre is spatially coherent at the output of the fibre. A source such as a light bulb or a star is made up of many tiny emitting elements within the source. Each element emits light independent of any other element in the source, so the light emitted by different points within the same source are incoherent. That is to say that there is no known phase relation between the light emitted by one point in the bulb and the light emitted by a different point in the bulb. The spatial coherence from such a non-point like source of incoherent emitters is related to the angle made between the source and two measurement points. If the source is small enough, the phase difference measured between two reasonably close measurement points will essentially be fixed. The degree of spatial coherence depends on how well the phase relation between the light at the two measurement points is defined. The degree of coherence varies between a value of 1 for coherent light and a value of 0 for incoherent light. Values between 0 and 1 represent the case of partial coherence.

For supercontinuum generation, nonlinear processes that occur inside the photonic crystal fibre result in the generation of new frequencies. Therefore, the temporal coherence length of light propagating through the fibre is reduced. This is why the supercontinuum beam has a very short temporal coherence length.

The supercontinuum source used during this research was bought from the Fianium company. It uses a passively mode-locked ytterbium fibre laser, which is then amplified through a ytterbium doped fibre amplifier. The output of the fibre amplifier is then coupled into a photonic crystal fibre to generate the supercontinuum beam. The amplifier is pumped by a high power, multi-emitter laser diode module. The ytterbium fibre laser has pulses of 4ps duration and operates at a repetition rate of 40MHz. The supercontinuum output is randomly polarized and has a spectral range of 464nm - 1750nm with a total output power of 6.3W.

2.4.2 Applications

A low temporal coherence source is useful for eliminating interference effects when studying optical binding effects.¹² Low temporal coherence is also particularly useful for imaging applications, such as white light scanning interferometry (WLSI)^{18,19} and optical coherence tomography (OCT). OCT uses the short temporal coherence length of the source to improve axial resolution. OCT uses a Michelson interferometer setup with the sample placed in one arm of the interferometer and a translating reference mirror placed in the other arm. If the path difference between the two arms of the interferometer is within the temporal coherence length of the source, an interference pattern can be detected. Then the sample is scanned longitudinally and laterally to build up an image. The axial depth of an image is limited to the distance over which the waves interfere. Therefore, a source with a short temporal coherence length allows imaging of a thin slice of the sample. In 1991, the first OCT experiment²⁰ used a superluminescent diode as the light source, and an axial resolution of 17 μ m in air was achieved. This resolution was then improved to <5 μ m in the late 1990s using a pulsed titanium-sapphire laser.^{21,22} It wasn't until several years later, in 2006, that a supercontinuum source was first used for OCT. The use of a supercontinuum source resulted in a similar resolution to that obtained

with the titanium-sapphire laser but provided access to a range of different wavelength bands. For imaging tissue, the use of a source with a wavelength band centred near 1300nm reduces scattering effects and gives deeper penetration into the tissue.²³ However, pulsed laser sources with a wavelength around 1300nm are uncommon. The broad bandwidth of the supercontinuum source provides a solution as demonstrated by Aguirre *et al.*²⁴ and Koch *et al.*²⁵ Both groups demonstrated the use of a supercontinuum source for OCT and achieved axial resolutions of $<7\mu\text{m}$. The wavelength bands used, which were suitable for imaging tissue, were around 1300nm (Aguirre *et al.*) and 1250nm (Koch *et al.*). In fact, the first practical application of the supercontinuum source was for OCT. Since then, there has been an upturn in research using supercontinuum sources. Imaging, spectroscopy, microscopy, optical manipulation and novel beam shaping are all areas of interest.

Due to its broad bandwidth, the supercontinuum source lends itself to spectroscopic applications. In the last few years, there has been great interest in finding out what this source can offer in the field of spectroscopy. Often, spectroscopy relies on the averaging of data taken from multiple objects in a sample. Using a supercontinuum source opens up the possibility for the simultaneous manipulation and spectroscopic analysis of individual objects.²⁶ The forward scattering spectrum of an object depends on the size, shape and refractive index of that object. Therefore, a detailed characterisation of individual objects can be carried out using the information obtained from the forward scattering spectrum of an optically trapped object. Using spectroscopic techniques, the supercontinuum source has been used to probe the properties of aerosols,²⁷ to determine the size of water droplets²⁸ and to investigate the electronic structure of carbon nanotubes.²⁹ Additionally, the supercontinuum source has made it possible to obtain the first plasmon spectra of gold nanoparticles smaller than 10nm.³⁰

In 2004, a new microscopy technique was developed that took advantage of the chromatic aberration effect of the supercontinuum beam to simultaneously image different depths in a sample. The technique was named ‘chromatic confocal microscopy’^{31,32} and it eliminates the need to mechanically scan a sample in the axial

direction. The experimental setup is illustrated in Figure 2.2. Each wavelength was simultaneously focused to a different depth in the sample due to chromatic aberration. Then, a grating was used to spatially separate out the light reflected from different sample depths. The image produced was detected using a CCD camera. As a result of the grating, the images from different sample depths were position dependent on the CCD camera. This technique has a depth resolution of $1\mu\text{m}$ and a scanning depth of $7\mu\text{m}$. Recently, a beam scanning chromatic confocal microscope has been used to generate three dimensional surface images using a broad bandwidth Xenon lamp.³³

The supercontinuum source has also been applied to fluorescence microscopy techniques. The use of a narrow bandwidth source for fluorescence microscopy allows the excitation of only selected fluorophores. The supercontinuum source has overcome this limitation

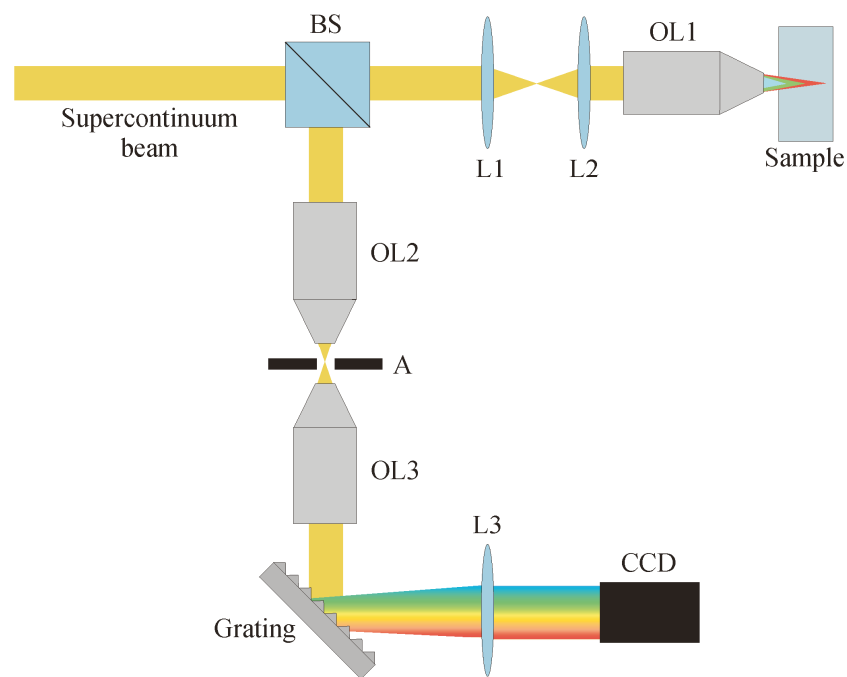


Figure 2.2. Illustration of the setup for chromatic confocal microscopy using a supercontinuum source. BS is beam splitter, OL is objective lens, L1, L2 and L3 are lenses and A is a $1\mu\text{m}$ diameter aperture. This image is based on that in reference [31].³¹

by providing access to multiple wavelengths from the same source.³⁴⁻³⁶ Therefore, a supercontinuum beam allows the simultaneous excitation of multiple different fluorophores in a single sample. Li *et al.*³⁷ measured the fluorescence of NADH (nicotinamide adenine dinucleotide) and tryptophan to investigate the metabolic activity

of cells and cell protein expression. They determined that the ratio of NADH fluorescence to tryptophan fluorescence can be used to identify cancer cells. Indeed, they believe that the identification of pre-cancer cells may be possible with this technique. Access to multiple wavelengths is essential for this technique so that both the NADH and tryptophan can be excited and the levels of fluorescence can be compared.

Confocal reflection microscopy was the next technique to benefit from the use of a supercontinuum source.³⁸ This method can produce reflection spectra as well as three dimensional images. Therefore, more information about a sample can be obtained using a supercontinuum confocal microscope than with a conventional confocal microscope. The supercontinuum beam is focused into the sample using a microscope objective. Then the reflected light, after passing through a pinhole, is incident on a grating to separate the spectral components. The spectral components are imaged onto a CCD camera via a scanning mirror and a lens. When the sample is scanned, by moving the sample stage, the mirror is simultaneously scanned. This enables the reflected spectrum from each sample position to be spatially separated out onto the CCD camera. Three dimensional images with spectral information can be produced in this way. This technique is a great advancement because images taken using a conventional confocal microscope do not obtain spectral information.

There is also great interest in the supercontinuum source amongst optical manipulation researchers. Optical guiding distances of particles can be extended by exploiting the chromatic aberration effect of a supercontinuum beam. Due to chromatic aberration an elongated focal region is produced, making it is possible to guide particles over much larger distances with a supercontinuum beam than is possible with a narrowband laser source.¹³ The particle can be guided in the direction of beam propagation by radiation pressure for distances of up to 3mm, which is twice the guiding distance previously achieved with a regular laser source. Interest in the use of a supercontinuum source for optical manipulation has since been piqued, and investigations into the forces involved in broadband optical manipulation are presented in this thesis. Additionally, results of the first broadband multiple trapping experiments are presented in Chapter 5.

Extending the use of a supercontinuum beam to microfluidic devices provides the opportunity to develop new ‘lab-on-a-chip’ technologies. For example, a supercontinuum source has been used to excite fluorophores in a microfluidic system for the analysis of cells.³⁹ Recently, an array of parabolic micromirrors has been built into a microfluidic system to facilitate the optical trapping of multiple objects.^{40,41} In this case, a narrowband laser was used. Optical trap sites are created when a laser is incident on the array of mirrors. Objects flow above the mirrors and can be caught in the optical traps for analysis. If a supercontinuum source were used instead of a narrowband laser, the micromirror setup could prove useful for the microfluidic spectroscopic analysis of cells. The work carried out into the use of a supercontinuum source with a micromirror array is presented in Chapter 5.

Finally, interest in the generation of novel beam shapes using broad bandwidth sources has grown in the last few years. The first ‘white light’ Bessel beam,² generated using a halogen bulb, provided insight into the role that coherence plays in the generation of novel beam shapes. A picture of this beam is shown in Figure 2.3.

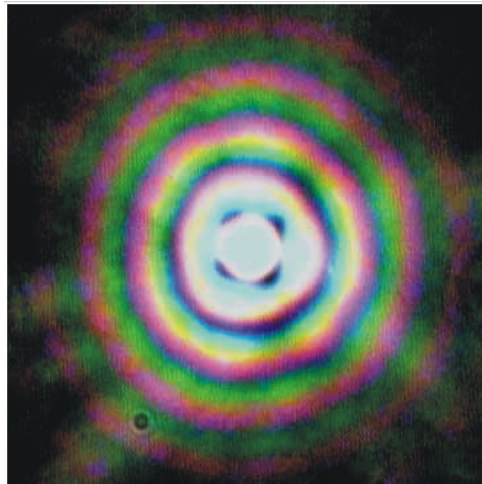


Figure 2.3. An image of a ‘white light’ Bessel beam generated using a halogen bulb is shown. It is clear to see that the different wavelength components of the beam produce light rings at different radial distances from the beam centre. Image taken from reference [2].²

There has also been an investigation carried out into the wavelength dependent behaviour of Bessel beams and their reconstruction properties. It was found that the reconstruction distance was dependent on wavelength.⁴² Another novel beam that has recently been generated using a broad bandwidth source is the optical bottle beam.^{43,44} This type of

beam has a dark centre enclosed by a region of high light intensity and could be useful for the optical confinement of atoms or microscopic objects. A broadband bottle beam has been generated,⁴⁵ and the wavelength dependent properties were investigated. Each wavelength component in the beam produced a bottle beam with a different diameter and range. ‘White light’ optical vortices^{46,47} have also been realised in recent years. This thesis further investigates the use of ‘white light’ for the generation of novel beam shapes and provides insight into the roles of both coherence and wavelength. The transfer of orbital angular momentum from a ‘white light’ optical vortex to microspheres is demonstrated. This work is presented in Chapter 6. Additionally, in Chapter 7, details are presented of the first ever ‘white light’ Airy beam along with an investigation into the propagation characteristics of an Airy beam.⁴⁸

2.5 Conclusion

A comparison between the properties of narrowband, pulsed and extended bandwidth sources has been presented. There are a range of narrowband laser sources that are readily available, relatively inexpensive and have a good beam profile. For these reasons narrowband lasers are often the first choice of source for optical manipulation applications. For biological applications, a laser source emitting at a wavelength that minimises the damage to cells or other biological items can be chosen for optical tweezing applications. The wavelength range where the damage to cells is minimised is called the ‘therapeutic window’ and has a range of approximately 700nm - 1064nm.

The use of a pulsed laser for optical manipulation allows nonlinear effects, such as two-photon fluorescence, to be exploited.³ However, pulsed lasers are seldom used for biological applications because the high peak power of the pulses often results in the death of the biological item.

The supercontinuum source has been introduced and some of the work carried out so far using this source has been reviewed. Unlike a conventional laser source, the supercontinuum source has a very broad bandwidth and a short temporal coherence length. However, the good spatial coherence of the source means that the beam has good

directionality and can be tightly focused. The use of a broadband laser for optical manipulation gives rise to the opportunity to develop spectroscopic applications.²⁶ As we demonstrate in Chapter 7, the supercontinuum source can also be used for studies into the wavelength dependent properties of beams. Different wavelength components can be selected from the supercontinuum beam using filters. Such studies can then be carried out without changing the laser source and the experimental setup. The supercontinuum source has low temporal coherence. For experiments that are hampered by interference effects, such as optical binding investigations, the supercontinuum source can be used to reduce problematic interference effects. This is achieved by splitting the supercontinuum source into two beams and increasing the path difference between the two counter propagating beams so that the path difference is larger than the temporal coherence length of the source.

References

1. Hecht, J. in *The Laser Guidebook* 101-120 (McGraw-Hill, 1999).
2. Fischer, P. et al. White light propagation invariant beams. *Optics Express* **13**, 6657-6666 (2005).
3. Agate, B., Brown, C. T. A., Sibbett, W. & Dholakia, K. Femtosecond optical tweezers for in-situ control of two-photon fluorescence. *Optics Express* **12**, 3011-3017 (2004).
4. Liu, Y., Sonek, G. J., Berns, M. W., Konig, K. & Tromberg, B. J. Two-photon fluorescence excitation in continuous-wave infrared optical tweezers. *Optics Letters* **20**, 2246-2248 (1995).
5. Sato, S. & Inaba, H. Second-harmonic and sum-frequency generation from optically trapped KTiOPO₄ microscopic particles by use of Nd-YAG and Ti:Al₂O₃ lasers. *Optics Letters* **19**, 927-929 (1994).
6. Malmqvist, L. & Hertz, H. M. Second-harmonic generation in optically trapped nonlinear particles with pulsed lasers. *Applied Optics* **34**, 3392-3397 (1995).
7. Mohanty, S. K., Rapp, A., Monajembashi, S., Gupta, P. K. & Greulich, K. O. Comet assay measurements of DNA damage in cells by laser microbeams and trapping beams with wavelengths spanning a range of 308 nm to 1064 nm. *Radiation Research* **157**, 378-385 (2002).
8. Konig, K., Liang, H., Berns, M. W. & Tromberg, B. J. Cell damage in near-infrared multimode optical traps as a result of multiphoton absorption. *Optics Letters* **21**, 1090-1092 (1996).
9. Liang, H. et al. Wavelength dependence of cell cloning efficiency after optical trapping. *Biophysical Journal* **70**, 1529-1533 (1996).
10. Svoboda, K. & Block, S. M. Biological applications of optical forces. *Annual Review of Biophysics and Biomolecular Structure* **23**, 247-285 (1994).

11. Metzger, N. K., Dholakia, K. & Wright, E. M. Observation of bistability and hysteresis in optical binding of two dielectric spheres. *Physical Review Letters* **96**, 068102 (2006).
12. Gherardi, D. M., Carruthers, A. E., Cizmar, T., Wright, E. M. & Dholakia, K. A dual beam photonic crystal fiber trap for microscopic particles. *Applied Physics Letters* **93** (2008).
13. Fischer, P. et al. Enhanced optical guiding of colloidal particles using a supercontinuum light source. *Optics Express* **14**, 5792-5802 (2006).
14. Siegman, A. E. in *Lasers* 357 (University Science Books, 1986).
15. Ranka J.K, W. R. S., Stentz A. J. Visible continuum generation in air-silica microstructure optical fibers with anomalous dispersion at 800nm. *Optics Letters* **25**, 25 (2000).
16. Qin, G. S. et al. Supercontinuum generation spanning over three octaves from UV to 3.85 microns in a fluoride fiber. *Optics Letters* **34**, 2015-2017 (2009).
17. Boyd, R. W. *Nonlinear Optics* (Academic Press, 2003).
18. Reolon, D., Jacquot, M., Verrier, I., Brun, G. & Veillas, C. Broadband supercontinuum interferometer for high-resolution profilometry. *Optics Express* **14**, 128-137 (2006).
19. Kassamakov, I. et al. Scanning white-light interferometry with a supercontinuum source. *Optics Letters* **34**, 1582-1584 (2009).
20. Huang, D. et al. Optical coherence tomography. *Science* **254**, 1178-1181 (1991).
21. Bouma, B. et al. high-resolution optical coherence tomographic imaging using a mode-locked Ti-Al₂O₃ laser source. *Optics Letters* **20**, 1486-1488 (1995).
22. Drexler, W. et al. In vivo ultrahigh-resolution optical coherence tomography. *Optics Letters* **24**, 1221-1223 (1999).
23. Schmitt, J. M., Knuttel, A., Yadlowsky, M. & Eckhaus, M. A. Optical-coherence tomography of a dense tissue - statistics of attenuation and backscattering. *Physics in Medicine and Biology* **39**, 1705-1720 (1994).
24. Aguirre, A. D. et al. Continuum generation in a novel photonic crystal fiber for ultrahigh resolution optical coherence tomography at 800 nm and 1300 nm. *Optics Express* **14**, 1145-1160 (2006).
25. Cimalla, P., Walther, J., Mehner, M., Cuevas, M. & Koch, E. Simultaneous dual-band optical coherence tomography in the spectral domain for high resolution in vivo imaging. *Optics Express* **17**, 19486-19500 (2009).
26. Li, P., Shi, K. B. & Liu, Z. W. Manipulation and spectroscopy of a single particle by use of white-light optical tweezers. *Optics Letters* **30**, 156-158 (2005).
27. Zemlyanov, A. A. & Geints, Y. E. Aerosol scattering of supercontinuum radiation formed upon femtosecond laser pulse filamentation in the atmosphere. *Optics Communications* **270**, 47-50 (2007).
28. Guillon, M., Dholakia, K. & McGloin, D. Optical trapping and spectral analysis of aerosols with a supercontinuum laser source. *Optics Express* **16**, 7655-7664 (2008).
29. Sfeir, M. Y. et al. Probing electronic transitions in individual carbon nanotubes by Rayleigh scattering. *Science* **306**, 1540-1543 (2004).

30. Lindfors, K., Kalkbrenner, T., Stoller, P. & Sandoghdar, V. Detection and spectroscopy of gold nanoparticles using supercontinuum white light confocal microscopy. *Physical Review Letters* **93** (2004).
31. Shi, K. B., Li, P., Yin, S. Z. & Liu, Z. W. Chromatic confocal microscopy using supercontinuum light. *Opt. Express* **12**, 2096-2101 (2004).
32. Shi, K. B., Nam, S. H., Li, P., Yin, S. Z. & Liu, Z. W. Wavelength division multiplexed confocal microscopy using supercontinuum. *Optics Communications* **263**, 156-162 (2006).
33. Chun, B. S., Kim, K. & Gweon, D. Three-dimensional surface profile measurement using a beam scanning chromatic confocal microscope. *Review of Scientific Instruments* **80** (2009).
34. Betz, T. et al. Excitation beyond the monochromatic laser limit: simultaneous 3-D confocal and multiphoton microscopy with a tapered fiber as white-light laser source. *Journal of Biomedical Optics* **10** (2005).
35. McConnell, G. Confocal laser scanning fluorescence microscopy with a visible continuum source. *Optics Express* **12**, 2844-2850 (2004).
36. Palero, J. A., Boer, V. O., Vijverberg, J. C., Gerritsen, H. C. & Sterenborg, H. Short-wavelength two-photon excitation fluorescence microscopy of tryptophan with a photonic crystal fiber based light source. *Optics Express* **13**, 5363-5368 (2005).
37. Li, D., Zheng, W. & Qu, J. A. Y. Two-photon autofluorescence microscopy of multicolor excitation. *Optics Letters* **34**, 202-204 (2009).
38. Booth, M. J., Juskaitis, R. & Wilson, T. Spectral confocal reflection microscopy using a white light source. *Journal of the European Optical Society-Rapid Publications* **3** (2008).
39. Telford, W. G., Subach, F. V. & Verkhusha, V. V. Supercontinuum white light lasers for flow cytometry. *Cytometry Part A* **75A**, 450-459 (2009).
40. Merenda, F., Rohner, J., Fournier, J. M. & Salathe, R. P. Miniaturized high-NA focusing-mirror multiple optical tweezers. *Optics Express* **15**, 6075-6086 (2007).
41. Merenda, F., Grossenbacher, M., Jeney, S., Forro, L. & Salathe, R. P. Three-dimensional force measurements in optical tweezers formed with high-NA micromirrors. *Optics Letters* **34**, 1063-1065 (2009).
42. Fischer, P. et al. Wavelength dependent propagation and reconstruction of white light Bessel beams. *Journal of Optics a-Pure and Applied Optics* **8**, 477-482 (2006).
43. Arlt, J. & Padgett, M. J. Generation of a beam with a dark focus surrounded by regions of higher intensity: the optical bottle beam. *Optics Letters* **25**, 191-193 (2000).
44. Wei, M.-D., Shiao, W.-L. & Lin, Y.-T. Adjustable generation of bottle and hollow beams using an axicon. *Optics Communications* **248**, 7-14 (2005).
45. Lin, J. H., Wei, M. D., Liang, H. H., Lin, K. H. & Hsieh, W. F. Generation of supercontinuum bottle beam using an axicon. *Optics Express* **15**, 2940-2946 (2007).
46. Leach, J. & Padgett, M. J. Observation of chromatic effects near a white-light vortex. *New Journal of Physics* **5** (2003).

47. Sztul, H. I., Kartazayev, V. & Alfano, R. R. Laguerre-Gaussian supercontinuum. *Optics Letters* **31**, 2725-2727 (2006).
48. Morris, J. E., Mazilu, M., Baumgartl, J., Cizmar, T. & Dholakia, K. Propagation characteristics of Airy beams: dependence upon spatial coherence and wavelength. *Optics Express* **17**, 13236-13245 (2009).

Chapter 3

Optical manipulation: an introduction

3.1 Synopsis

This chapter serves as an introduction to optical manipulation. The specific case of an optical tweezers arrangement will be used to explain how a microscopic object can be manipulated by light. This information can then be extended to the other optical manipulation techniques outlined in Chapter 1: optical trapping, optical levitation, optical guiding and dual beam trapping. An object in an optical trap behaves like a damped harmonic oscillator. The Brownian motion of the sphere acts as the driving force, the gradient force of a focused laser beam provides the restoring force and the viscosity of the medium surrounding the object results in damping. With this knowledge of how an object behaves in an optical trap, the efficiency of the optical trap and the forces involved can be determined. In this chapter, methods are described to measure the forces in optical manipulation using a parameter known as the ‘trap stiffness value.’ The ‘ Q value’ parameter, which is a measure of the efficiency of an optical trap, is also introduced.

The characterisation of forces using trap stiffness values in optical manipulation has allowed further insight into single molecule studies. One end of a molecule can be tethered to a coverslide whilst the other end is attached to a microsphere. If the microsphere is optically tweezed by a focused laser, the molecule can then be stretched

by moving the coverslide. The trap stiffness value of the microsphere can be measured, giving insight into the forces acting on the molecule. Information about the elasticity of molecules can be determined from the trap stiffness value.¹ Insight into many single molecule biophysical processes can be gained in this way.

3.2 Optical manipulation: an explanation

Light can exert a force on an object. This force is very small, on the order of picoNewtons, but it can be used to manipulate small objects such as microspheres. A laser beam has an intensity gradient in the transverse direction due to the Gaussian profile of the beam. This intensity gradient gives rise to a ‘gradient force.’ The gradient force attracts microspheres (with a higher refractive index than their surroundings) into the most intense region of the beam. When a laser is focused to a tight spot, there is also an intensity gradient in the axial direction. Acting counter to the gradient force, there is a scattering force, which is a result of photons scattering from the microsphere. The axial component of the scattering force uses radiation pressure to push the object in the direction of beam propagation. If the axial gradient force is large enough to balance the scattering force, the object will settle at an equilibrium position in the focal region of the laser beam.

There are three regimes for optical manipulation: the Mie regime where the object is more than 10 times larger than the wavelength of the laser light; the Rayleigh regime where the object size is smaller than $\lambda/20$ and the Lorentz-Mie regime where the size of the object is approximately the same as the wavelength. Figure 3.1 illustrates the different optical manipulation regimes.

In the case of objects that are more than ten times larger than the laser wavelength, Mie theory^{2,3} is used to explain the photon-sphere interaction. The incoming photons have a momentum of $\hbar k$ each, where \hbar is Planck’s constant divided by 2π and k is the wavenumber. When light is refracted through a microsphere, the direction of the photon momentum is changed, see Figure 3.2. Due to conservation of momentum, the

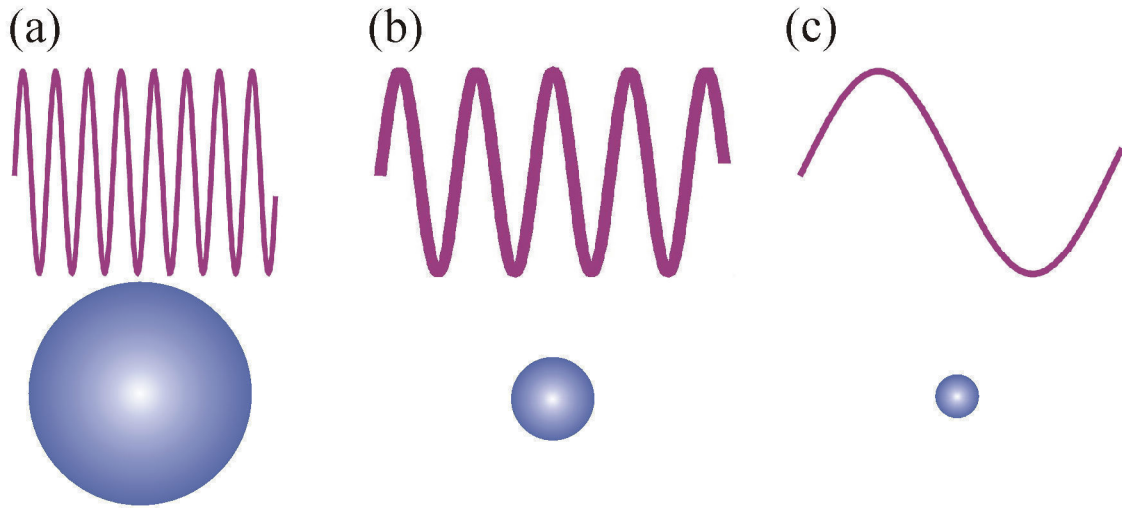


Figure 3.1. Image (a) represents the Mie regime where the object is much larger than the laser wavelength (object size $>10\lambda$). Image (b) represents the Lorentz-Mie regime where the object is approximately the same dimensions as the laser wavelength. Image (c) represents the Rayleigh regime where the object is much smaller than the laser wavelength (object size $<\lambda / 20$).

microsphere must experience an equal and opposite change in momentum. For spheres with a higher refractive index than the surrounding medium, this momentum change draws the object towards the focus of the beam. In the transverse direction, the incoming vertical rays are refracted through the sphere and there is a net gain of momentum in the negative x direction. The sphere must gain momentum of equal magnitude in the opposite direction, the positive x direction, so the net transverse force on the sphere is towards the centre of the beam.

Trapping in the axial direction can be similarly explained. When a beam is tightly focused, there is a gradient force in the axial direction. In Figure 3.2(d), the light rays are refracted through the sphere such that they gain momentum in the $-z$ direction. Consequently, the sphere must gain momentum in the $+z$ direction i.e. towards the focus of the beam.

In the case of objects that are much smaller than the laser wavelength, ray optics (Mie theory) is no longer used to explain the interaction taking place between the photons and the object. Instead, the Rayleigh regime applies in cases where the object is smaller than $\lambda / 20$. For the Rayleigh regime, optical manipulation can be explained by noting that a

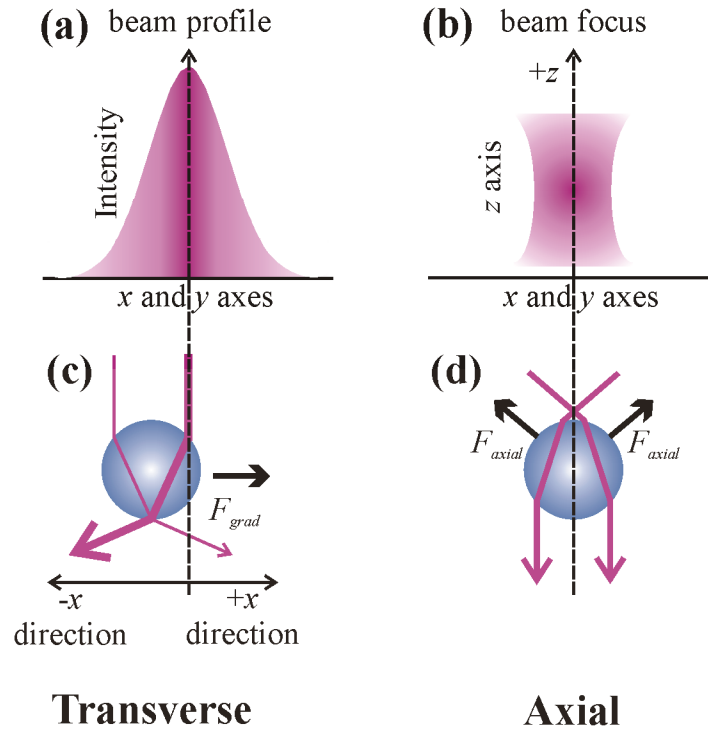


Figure 3.2. The transverse intensity profile of a Gaussian beam is shown in image (a). A focused beam, which is most intense at the centre with the intensity dropping off in the z direction away from the centre, is shown in image (b). A transverse trapping ray diagram is shown in image (c), where the thicker line represents a light ray with a higher intensity than the light ray represented by the thinner line. An axial trapping ray diagram is shown in image (d). F_{axial} is the resultant force acting on the sphere and F_{grad} is the gradient force.

polarizable particle present in an electric field has an induced dipole. The induced dipole oscillates in response to the electric field oscillations. The force acting on a point charge in an electric field is described by the Lorentz force. The magnitude of the force acting on each side of the induced dipole in a non-uniform electric field is unequal. The electric field gradient in an optical tweezers results in a net force that draws the object to the region of maximum intensity, where the forces acting on the positive and negative sides of the dipole are balanced. This is the gradient force (also known as the dipole force). The electric dipole has the lowest energy when it is positioned in the focal region of the beam. There is also a scattering force. Ashkin *et al.*⁴ determined the gradient force, F_{grad} , and the scattering force, F_{scat} , for trapped objects in the Rayleigh regime as per Equations 3.1 and 3.2.

$$F_{grad} = \frac{-n_m}{2} \alpha_p \nabla \mathbf{E}^2 = -\frac{n_m^3 a^3}{2} \left(\frac{m^2 - 1}{m^2 + 2} \right) \nabla \mathbf{E}^2 \quad (3.1)$$

$$F_{scat} = \frac{n_m P_{scat}}{c} = \frac{n_m I}{c} \frac{128 a^6 \pi^5}{3 \lambda^4} \left(\frac{m^2 - 1}{m^2 + 2} \right)^2, \quad (3.2)$$

and the scattering cross-section of the sphere, σ_{sc} , is⁵

$$\sigma_{sc} = \frac{128 \pi^5 a^6}{3 \lambda^4} \left(\frac{m^2 - 1}{m^2 + 2} \right)^2, \quad (3.3)$$

where ∇ is the gradient operator, \mathbf{E} is the electric field vector, $m = n_s / n_m$ is the ratio between the refractive index of the sphere, n_s , and that of the surrounding medium, n_m , λ is the wavelength, c is the speed of light, a is the radius of the sphere, I is the intensity, P_{scat} is the scattered power and α_p is the polarizability of the sphere. A sphere with a high polarizability will be trapped more strongly than a less polarizable sphere because the gradient force is proportional to polarizability.

A polarizable particle present in an electric field has an induced dipole with dipole moment \mathbf{p} . The Lorentz force, \mathbf{F}_L , describes the force acting on a single charge in an external electric field and is given by Equation 3.4.

$$\mathbf{F}_L = q \left(\mathbf{E} + \frac{d\mathbf{x}}{dt} \times \mathbf{B} \right), \quad (3.4)$$

where \mathbf{E} is the electric field at the position of the charge, q is the charge, \mathbf{B} is the magnetic field and \mathbf{x} is the position of the charge. For a dipole, the total force is

$$\mathbf{F}_{tot} = q \left(\mathbf{E}_1(x, y, z) - \mathbf{E}_2(x, y, z) + \frac{d(x_1 - x_2)}{dt} \times \mathbf{B} \right), \quad (3.5)$$

where \mathbf{E}_1 is the electric field at the position of the positive side of the dipole, \mathbf{E}_2 is the field at the position of the negative side of the dipole, x_1 is the position of the positive side of the dipole, x_2 is the position of the negative side of the dipole and \mathbf{B} is the magnetic field. For a small sphere, the distance between the dipoles is very small and we can rewrite the above equation as

$$\mathbf{F}_{tot} = q \left(\mathbf{E}_1(x, y, z) + ((x_1 - x_2) \cdot \nabla) \mathbf{E} - \mathbf{E}_1(x, y, z) + \frac{d(x_1 - x_2)}{dt} \times \mathbf{B} \right). \quad (3.6)$$

The dipole moment is $\mathbf{p} = q(\mathbf{x}_1 - \mathbf{x}_2) = \alpha_p \mathbf{E}$, where α_p is the polarizability of the sphere.

The total force equation can then be written as

$$\mathbf{F}_{tot} = \alpha_p \left((\mathbf{E}(x, y, z) \cdot \nabla) \mathbf{E}(x, y, z) + \frac{d\mathbf{E}(x, y, z)}{dt} \times \mathbf{B} \right). \quad (3.7)$$

Using the following substitutions:

$$(\mathbf{E} \cdot \nabla) \mathbf{E} = \nabla \left(\frac{1}{2} \mathbf{E}^2 \right) - \mathbf{E} \times (\nabla \times \mathbf{E}), \quad (3.8)$$

$$\nabla \times \mathbf{E} = -\frac{d\mathbf{B}}{dt}, \quad (3.9)$$

we can determine that the total force on the dipole is proportional to the gradient of the electric field as given in Equation 3.10,

$$\mathbf{F}_{tot} = \alpha_p \left(\frac{1}{2} \nabla \mathbf{E}^2 + \frac{d}{dt} (\mathbf{E} \times \mathbf{B}) \right). \quad (3.10)$$

The second term averages to zero and we get the optical dipole force, F_{grad} ,

$$F_{grad} = \frac{1}{2} \alpha_p \nabla \mathbf{E}^2. \quad (3.11)$$

The regime between Mie and Rayleigh is called Lorentz-Mie. The Lorentz-Mie regime applies to the case where the size of the object is similar to the wavelength of laser light. However, usually the less complex Mie or Rayleigh theories are sufficient.

A typical experimental setup used for optical manipulation is shown in Figure 3.3. For the case of optical tweezers, a strong axial gradient force is necessary. Therefore, the laser beam is expanded using a telescope to match the beam size to the back aperture of the objective lens. The objective lens used typically has a numerical aperture close to 1. The full numerical aperture of the objective lens can be taken advantage of by filling the back aperture of the objective lens with the laser beam. The highest axial gradient force possible with that objective lens can then be achieved.

In order to translate the beam in the trapping plane, a beam steering arrangement is often incorporated into the setup. Mirror M2, the steering mirror, is imaged onto the back focal plane of the objective lens using relay lenses L3 and L4. As a result, the steering mirror and the back focal plane of the objective are conjugate planes. The beam can then be translated in the sample by adjusting mirror M2 whilst not being translated in the conjugate plane. The beam steering arrangement ensures that the laser beam is always centred on the back aperture of the objective lens.

To view the optically manipulated object, a white light illumination source such as a halogen bulb is used. The light passes through the microscope objective and a dichroic mirror, M3, to reach the CCD camera. The dichroic mirror reflects the laser into the trapping plane whilst transmitting the illumination light through to the CCD camera. An interference filter is placed before the CCD camera to block out the residual laser light. In Chapter 5 (Section 5.2.1), the adaptation of this setup to accommodate the use of a supercontinuum source is explored.

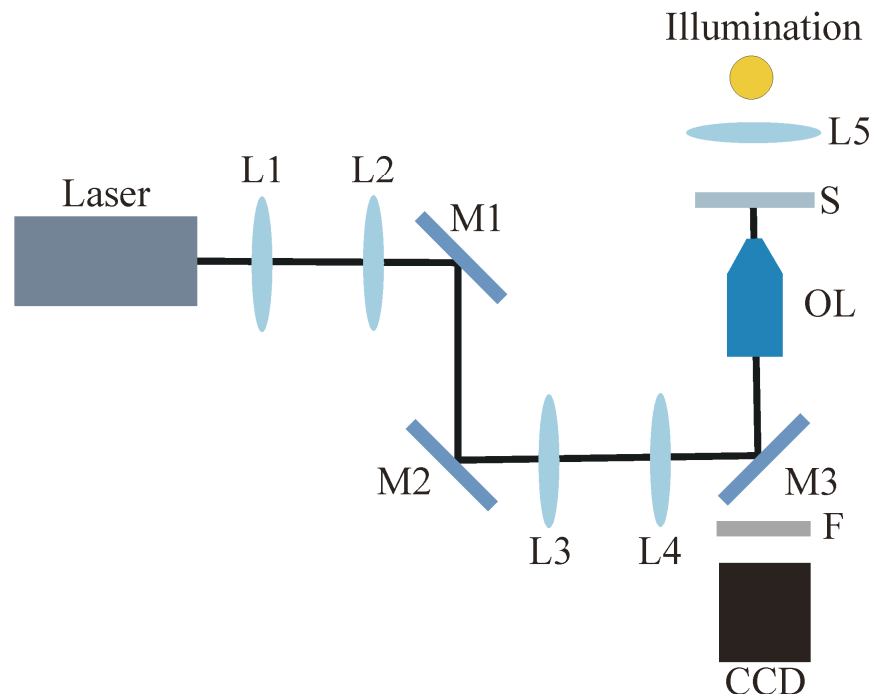


Figure 3.3. A typical optical manipulation setup is illustrated. Lenses L1 and L2 are used to expand the beam. M1 and M2 are mirrors. M3 is a dichroic mirror that reflects the laser light but transmits the illumination light. Lenses L3 and L4 are relay lenses that are used in conjunction with mirror M2 for steering the beam in the sample plane. The microscope objective lens OL focuses the laser into the sample S and also collects the illumination light. F is a filter that blocks the lasing wavelength from the CCD camera. Lens L5 is used to direct the illumination light into the sample.

3.3 Characterising an optical trap

3.3.1 Introduction to Q values

It is often useful to characterise the forces involved in optical manipulation. One way to establish the efficiency of an optical tweezers is to determine the Q value of the system. This is a dimensionless parameter that has a value between 0 and 2. The Q value is a measure of the efficiency of the transfer of momentum from the trapping laser to the trapped object. A Q value of 2 represents the case where the change of momentum of a photon interacting with an object is $2p_1$, where the initial momentum of the photon is p_1 . A Q value of zero represents no change in the incident photon's momentum. Momentum is a conserved quantity. Therefore, the combined momentum of the photon and object must be the same before and after the photon interacts with the object. Figure 3.4(a) illustrates the case where a photon with initial momentum $+p_1$ is reflected 180° by an object with no initial momentum. The total initial momentum of the system is $+p_1$. After the collision, the photon has momentum $-p_1$ and the momentum of the object is $+2p_1$. The total momentum of the system after the collision is the same as it was before the collision, i.e. $+p_1$. The total change in momentum of the photon during the process was $\Delta p = 2p_1$. This represents the situation for $Q = 2$. Figure 3.4(b) illustrates a more general case where the momentum of the photon before the interaction with an object is p_1 , where all of the momentum is in the horizontal axis. After the interaction, the direction of the momentum has changed such that there is a gain in momentum in the vertical direction and a reduction in momentum in the horizontal direction. The momentum in the horizontal direction after the interaction is $p_h = p_1 \cos \theta$, and in the vertical direction the magnitude of the momentum is $p_v = p_1 \sin \theta$. As a result, the object has an equal and opposite momentum change.

The Q value of an optical trap can be determined experimentally. Figure 3.5 illustrates the sample chamber during such a measurement. A laser is focused into a sample chamber containing microspheres immersed in a fluid, which is typically water. The microsphere is optically tweezed in the laser beam. The sample chamber, and therefore

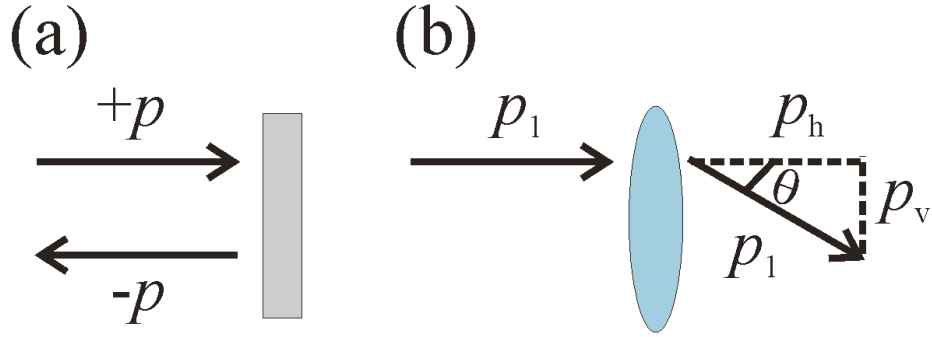


Figure 3.4. Image (a) shows a photon with momentum p reflected from a mirror. After reflection the photon has momentum $-p$. The total momentum change of the photon is $2p$. Image (b) shows a photon with momentum p_1 refracted through a lens by an angle θ .

the fluid, is then translated at a known velocity v_{fluid} . The microsphere experiences a drag force due to the motion of the fluid F_{drag} . This causes the microsphere to become displaced from its previous equilibrium position at the centre of the laser beam. The gradient force F_{grad} , acting on the sphere from the laser, balances the drag force at a new equilibrium position for the microsphere. At a certain velocity, the drag force overcomes the trapping force and the microsphere is pulled out of the optical tweezers. The maximum fluid velocity where the sphere stays in the optical tweezers can be used to determine the Q value.⁶

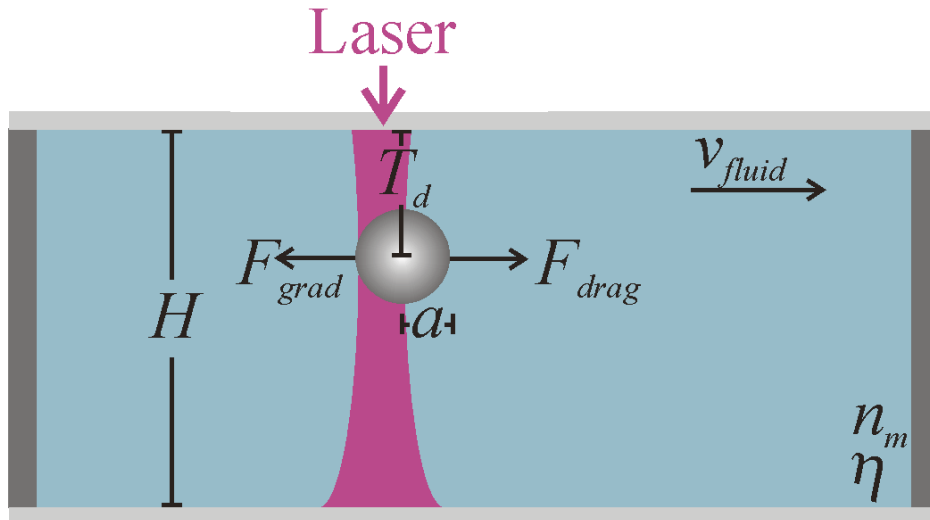


Figure 3.5. A laser beam is focused into the sample chamber from above. The sample chamber, and therefore the fluid, is translated at a known velocity v_{fluid} . The sphere has radius a and is a distance T_d from the edge of the sample chamber. The sample chamber has height H and the fluid has refractive index n_m and viscosity η . The forces acting on the sphere are indicated by F_{drag} and F_{grad} .

The equations for F_{grad} and F_{drag} are given below. The Q value can then be determined using Equation 3.14, where v_{max} is the maximum velocity of the fluid where the object remains confined by the optical tweezers.

$$F_{grad} = \frac{Qn_m P_{trap}}{c}, \quad (3.12)$$

$$F_{drag} = 6\pi\eta\beta v_{fluid} a, \quad (3.13)$$

$$Q = \frac{6\pi\eta\beta v_{max} ac}{n_m P_{trap}}. \quad (3.14)$$

P_{trap} is the power in the trapping plane, c is the speed of light and n_m is the refractive index of the medium surrounding the sphere to be trapped, v_{fluid} is the velocity of the fluid surrounding the sphere, η is the viscosity of the fluid surrounding the sphere, β takes into account surface effects and a is the radius of the trapped sphere. The transverse surface effects, which account for the sphere being close to the boundary of the sample chamber, can be calculated by the Faxen correction term,⁷

$$\beta = \frac{1}{1 - \frac{9}{32} \left(\frac{2a}{T_d} \right) + \frac{1}{64} \left(\frac{2a}{T_d} \right)^3 - \frac{45}{4096} \left(\frac{2a}{T_d} \right)^4 - \frac{1}{512} \left(\frac{2a}{T_d} \right)^5}, \quad (3.15)$$

where T_d is the distance from the centre of the sphere to the boundary of the sample chamber. When T_d is large, $\beta \rightarrow 1$. This is the case when the sphere is far away from the edge of the sample chamber and surface effects can be ignored.

3.3.2 Trap stiffness

The Q value is a useful parameter to measure the efficiency of the momentum transfer in an optical tweezers. It is also a simple way to compare the efficiency of optical tweezers produced using different laser sources. However, the Q value is not a measure of the forces involved in an optical tweezers. For the study of biological systems, a direct measurement of the optical forces is required. This can be achieved by measuring a parameter known as trap stiffness. Two methods for measuring trap stiffness values will

now be described. These methods are the power spectrum method and the optical potential analysis method.

3.3.2.1 Power spectrum method

The interaction between fluid molecules and a microsphere causes the microsphere to move. The motion of the sphere due to the interaction with the surrounding fluid molecules is called Brownian motion and can be described by the Einstein diffusion equation,⁸

$$D_E = k_B T / \gamma_0, \quad (3.16)$$

where γ_0 is the friction coefficient, $k_B T$ is the Boltzmann energy and D_E is the diffusion constant.

An object that is optically tweezed moves around within the optical potential as a result of Brownian motion. The position of the object as a function of time in the x , y and z axes can be measured experimentally. If the position of the object as a function of time in the x axis is denoted by $x(t)$, then the magnitude of the squared displacement of the object is denoted by $|x(t)|^2$. The path of the object can be broken down into frequency components of varying amplitude, and it is this frequency analysis of the sphere's position that is the power spectrum. The power spectrum in the x axis is denoted by $S_{\lambda,x}(f)$. The position information $|x(t)|^2$ can be converted into the frequency domain by taking the Fourier transform to give $S_{\lambda,x}(f) = |\tilde{x}(t)|^2$, where the tilda denotes the Fourier transform. This is the power spectrum of the optically trapped object in the x axis. $S_{\lambda,x}(f)$ can be used to determine the trap stiffness value relating to the x axis. Similarly the power spectrum in the y axis is given by $S_{\lambda,y}(f) = |\tilde{y}(t)|^2$.

An optically tweezed sphere behaves like an over-damped harmonic oscillator, which can be described by the Langevin equation $m\ddot{x}(t) + \gamma_0\dot{x}(t) + \kappa x(t) = F(t)$, where $\ddot{x}(t)$ is the second time derivative, $\dot{x}(t)$ is the time derivative, κ is the trap stiffness, γ_0 is the

hydrodynamic drag coefficient such as Stokes drag and $F(t)$ is the force acting on the sphere due to Brownian motion. Optical manipulation is typically in the low Reynolds number regime. This means that the inertial term ($m\ddot{x}(t)$) in the Langevin equation is negligible in comparison to the viscous damping and can be ignored. The Langevin equation for an over-damped harmonic oscillator (without the inertial term), the power spectrum equation for a sphere in an optical tweezers and the corner frequency equation respectively are given by⁵

$$F(t) = \gamma_0 \frac{dx}{dt} + \kappa x, \quad (3.17)$$

$$S_{\lambda,x}(f) = |\tilde{x}(t)|^2 = \frac{|F(f)|^2}{4\pi^2\gamma_0^2(f_0^2 + f^2)} = \frac{k_B T}{\pi^2\gamma_0(f_0^2 + f^2)}, \quad (3.18)$$

$$f_0 = \frac{\kappa}{2\pi\gamma_0}, \quad (3.19)$$

where k_B is Boltzmann's constant, T is the temperature in Kelvin, f is the frequency, f_0 is the corner frequency and the other parameters are defined above. The corner frequency is related to the trap stiffness, κ , as shown in Equation 3.19, and $|F(f)|^2 = 4\gamma_0 k_B T$. The mean square displacement of the object in the x axis can be determined by⁹

$$\langle x(t)^2 \rangle = 2\pi \int_0^\infty S_{\lambda,x}(f) df. \quad (3.20)$$

A high trap stiffness value indicates that a sphere is well confined in the optical potential. Higher frequencies contribute more to the power spectrum when the trap stiffness value is high. Therefore, a stronger optical tweezers has a higher corner frequency than a weak optical tweezers.

The power spectrum plot takes the shape of a Lorentzian profile (Equation 3.18) and the corner frequency, f_0 , can be used to determine the trap stiffness value (Equation 3.19). The corner frequency is the frequency at which $|\tilde{x}(t)|^2$ is half of its asymptotic value. Example power spectrum data is shown in Figure 3.6.

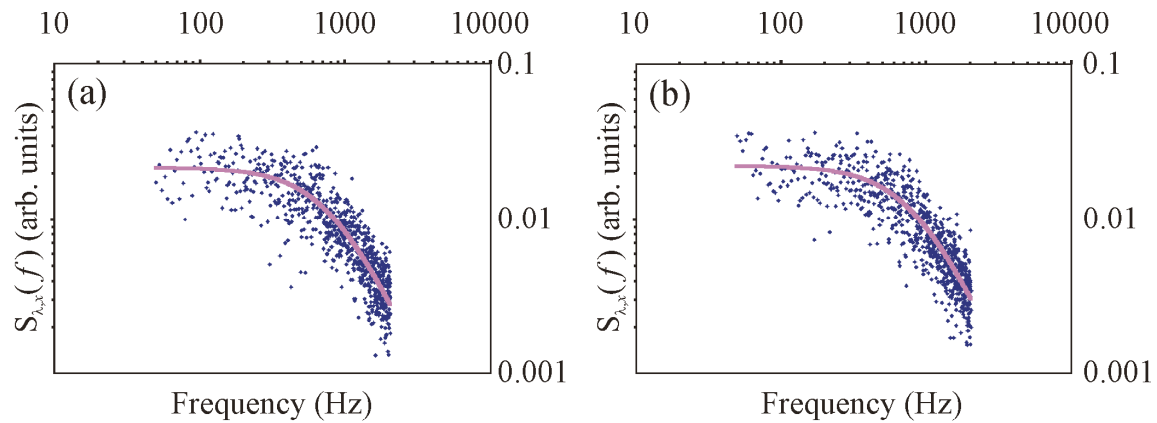


Figure 3.6. Example power spectra are shown for the x (a) and y (b) axes of an optical trap. The solid line shows the theoretical fit.

Although there are other methods to determine the power spectrum of a trapped sphere, the method used in this research is the back focal plane detection method.¹⁰ A typical experimental setup for this method is shown in Figure 3.7(a). Some of the laser light is scattered from the optically trapped sphere. The light is collected by an objective lens, and an interference pattern between the scattered and un-scattered light is formed at the back focal plane of the objective lens. This interference pattern causes variations in the light intensity that can be used to determine the position of the trapped object.⁵ The back focal plane of the objective lens is imaged onto a detector called a quadrant photodiode (QPD). A QPD is a circularly symmetric device with four photodiodes arranged as in Figure 3.7(b). The QPD uses the information from the light intensity incident on each quadrant to determine the motion of a trapped sphere. The interference of the un-scattered light with either the forward scattered light or the backscattered light from the sphere can be used. Since the use of the backscattered light gives a signal of lower intensity, the forward scattered light is used in this research.

The photodiode signals are first amplified. Then summation circuits add and subtract the data from the individual photodiodes to separate the horizontal, vertical and axial information. Each photodiode quadrant gives out a voltage dependent on the intensity of laser light that is incident on it. The sphere's position can be determined from these voltages using the following equations:⁸

$$\begin{aligned}
V_z &\equiv V_A + V_B + V_C + V_D \\
R_x &\equiv (V_A - V_B - V_C + V_D)/V_z \\
R_y &\equiv (V_A + V_B - V_C - V_D)/V_z
\end{aligned}
\tag{3.21}$$

V_z is proportional to the z position of the trapped sphere, R_x is proportional to the position of the sphere in the x axis and R_y is proportional to the y position of the sphere. V_A , V_B , V_C and V_D represent the voltages at each of the four photodiodes of the QPD.

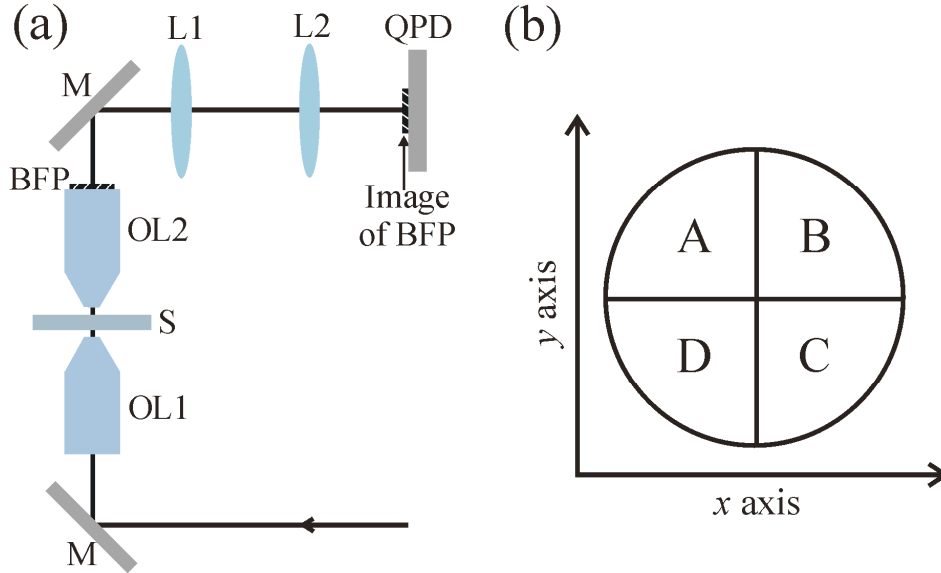


Figure 3.7. Diagram (a) is a typical experimental setup used for the back focal plane detection method. This setup is for detecting the interference between the forward scattered light from the microsphere and the unscattered light. Mirrors (M) are used to direct the laser beam, and objective lens 1 (OL1) focuses the beam into the sample (S). An interference pattern is formed at the back focal plane (BFP) of objective lens 2 (OL2). Lenses, L1 and L2, image the interference pattern onto the QPD. Diagram (b) illustrates the circular face of the QPD, where each segment of the circle is a separate photodiode. Each photodiode is labelled A, B, C or D for reference to Equation 3.21.

The quadrants are labelled accordingly in Figure 3.7(b). The information about the position of the sphere can be used to determine the power spectrum similar to those in Figure 3.6. A Lorentzian profile (Equation 3.18) is fitted to the data and the trap stiffness value can be determined from the corner frequency of the fit (Equation 3.19).

The QPD can be used to determine axial trap stiffness values. Light undergoes a π phase shift as it travels through the focal plane, which is known as the Gouy phase shift. In the axial direction, the Gouy phase shift is used to determine the position of the sphere. Light

that is scattered from the trapped sphere maintains the phase it had at the time of scattering. Therefore, if the light was scattered before passing through the focus, it does not obtain the π phase shift that it would have if the light was scattered after passing through the focus. However, the un-scattered light always passes through the focus and obtains the Gouy phase shift. Thus, the interference between the scattered and un-scattered light in the axial direction can be used to determine the axial position of the trapped sphere.

3.3.2.2 Optical potential analysis method

Another, less common, method to measure trap stiffness values involves the use of a high frame rate camera.⁸ Using such a camera, a video is taken of the optically trapped object. Using particle tracking software, the position of the sphere as a function of time can be determined. Producing a histogram of this data gives the position probability function for the trapped sphere. The position probability function is shown in Equation 3.22, and the optical trapping potential, $U(x)$, is related to the trap stiffness value by Equation 3.23.⁵

$$\rho(x) \propto \exp\left(\frac{-U(x)}{k_B T}\right) = \exp\left(\frac{-\kappa x^2}{2k_B T}\right) \quad (3.22)$$

$$U(x) = \left(\frac{\kappa}{2}\right)x^2 \quad (3.23)$$

where $U(x)$ is the trapping potential, k_B is Boltzmann's constant, T is the temperature and κ is the trap stiffness value. An optical trap produced by a focused Gaussian beam has an approximately parabolic optical dipole potential, V_{dipole} , with the minimum of the parabola at the centre of the optical trap. The optical dipole potential is only parabolic close to the centre of the trap. The gradient force is related to the gradient of the optical dipole potential by $F_{grad} \propto -\nabla V_{dipole}$. Therefore, a trapped sphere that deviates from the beam centre experiences a force pulling it back towards the centre of the trap. From Equation 3.11, we see that the optical dipole potential depends on the polarizability and the electric field strength as $V_{dipole} = -(1/2)\alpha_p E^2$. The restoring force, $F_{restore}$, acting on the optically trapped object is linear with position such that $F_{restore} = \kappa r$, where κ is the trap stiffness and r is the radial displacement of the object from the centre of the trap.

The position probability function has a Gaussian distribution with the highest position probability at the centre of the trap. Figure 3.8(a) shows how a sphere in an optical tweezers can be regarded as a simple harmonic oscillator. Figures 3.8(b) and (c) show examples of a position histogram and an optical trapping potential for an optically tweezed sphere respectively.

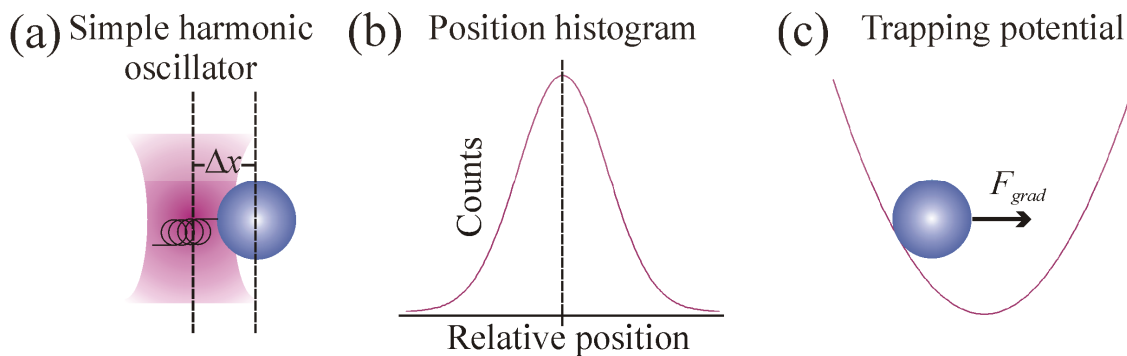


Figure 3.8. Illustration (a) is of a trapped sphere acting like a damped harmonic oscillator (mass on a spring) with $F_{grad} = -\kappa\Delta x$. Illustration (b) shows a position probability histogram that can be used to determine the trapping potential. Illustration (c) is a representation of the gradient force acting on a trapped particle in a trapping potential.

The trap stiffness value can be determined from the x^2 coefficient of Equation 3.23. This method is usually only applicable when measuring transverse trap stiffness values. To measure the axial trap stiffness value, the power spectrum method can be used.

3.4 Review of experiments

The ability to accurately measure forces using optical tweezers has allowed the direct characterisation of single molecules. An optically trapped sphere can be attached to a single molecule allowing indirect optical manipulation of the molecule. The molecule is then brought close to another molecule, and the forces acting on the trapped sphere can be measured to gain information about the interaction of the molecules.

The first single molecule investigations using optical tweezers were carried out into molecular motors such as myosin and kinesin. Myosin is a molecule that drives muscle contraction. It binds to a filament of actin and travels along the filament using energy from adenosine triphosphate (ATP). *Finer et al.*¹¹ investigated the forces involved in this process. They attached an actin molecule to two optically trapped microspheres and

stretched the molecule. A sphere, which was stuck to a coverslide, was coated with a small number of myosin molecules. The actin was then brought close to the myosin coated bead, and the forces acting on one of the trapped spheres attached to the actin were recorded. They found that myosin moves along the actin in steps of about 11nm with a force of 3pN - 4pN. Figure 3.9(a) illustrates the arrangement used for this experiment. Kinesin molecules have also been shown to move in nanometer sized steps.¹² Kinesin molecules transport vesicles by moving along microtubule tracks. A kinesin molecule has two globular head domains and until 2004 it was difficult to distinguish the interactions from each with the microtubule. Then, Jeney *et al.*¹³ used mutant kinesin molecules that had only one globular head domain. This allowed them to investigate the interaction between only one of the globular head domains with a microtubule. The arrangement that was used is illustrated in Figure 3.9(b). A kinesin molecule was attached to an optically tweezed sphere and brought close to a microtubule to observe their interaction. The back focal plane of the collection objective was imaged onto a quadrant photodiode. They used the information from the QPD to determine the forces acting on the kinesin molecule and its displacement along the microtubule.

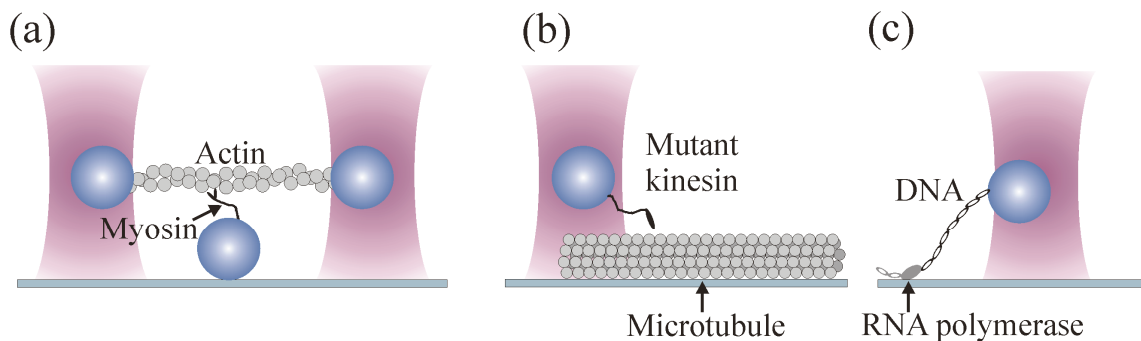


Figure 3.9. Illustration (a) is of the arrangement used to study the actin-myosin interaction. Illustration (b) shows a kinesin molecule tethered to an optically tweezed microsphere interacting with a microtubule. Illustration (c) shows a strand of DNA tethered to an optically tweezed microsphere at one side and a microscope slide (via RNA polymerase) on the other side.

The use of optical tweezers to study single molecules has also been extended to strands of DNA. Wang *et al.*¹ attached a DNA strand to an optically tweezed microsphere at one side and to a microscope slide (via RNA polymerase) on the other side. The sphere could then be moved to stretch the DNA. A QPD was used to measure the forces acting on the DNA strand. Figure 3.9(c) illustrates the arrangement used to stretch the DNA strand.

These are just a few ways that optical tweezers can be used to measure forces acting on single molecules and to gain insight into biological processes. More information can be found in a review paper by Mehta *et al.*¹⁴ Other applications for the measurement of forces in optical tweezers include investigations into the interactions between colloids.¹⁵ Two microspheres trapped in separate optical traps can be brought close together, and the hydrodynamic cross correlations can be studied using a QPD to monitor the forces acting on both spheres.

3.5 Conclusion

This chapter has described how light can be used to optically manipulate microscopic objects. The gradient force arising from the intensity gradient in a tightly focused Gaussian beam can be used to draw microscopic objects towards the high intensity beam focus. For the formation of a stable trap, the gradient force of the beam must be sufficient to balance other forces acting on the sphere, such as the scattering force and the gravitational force. The efficiency of the momentum transfer from a laser to an object in an optical trap can be determined using a parameter known as the Q value. The Q value of an optical trap can have a value between 0 and 2. A Q value of 2 indicates that there has been a maximum transfer of momentum from a photon to an object, and a Q value of 0 indicates that there has been no transfer of momentum. The Q value is a useful quantity for comparing the efficiency of optical traps generated using different laser sources. However, the Q value does not directly determine the optical forces acting on a trapped object.

On the other hand, trap stiffness values are a direct measurement of the forces acting on an optically confined object. Two methods that can be used to determine the trap stiffness values of an optical trap have been presented. The ‘power spectrum method’ uses a quadrant photodiode to detect the movement of a sphere in an optical trap. The power spectrum of the trapped sphere can then be determined and the corner frequency can be used to determine the trap stiffness value. Alternatively, a high frame rate camera can be used to obtain a video of a trapped sphere. The motion of the sphere can be tracked using computer software and a position probability histogram can be plotted from the data. The

trapping potential can then be determined, and the trap stiffness value can be obtained from the x^2 coefficient of the fitted parabola. In this thesis we call this method the ‘optical potential analysis method.’ The ability to determine the forces acting on a sphere in an optical trap has allowed detailed investigations to be carried out into single molecules and their interactions.^{1,11-13} Optical tweezers can also be used to bring colloidal particles close together and study the interactions between them.¹⁵

References

1. Wang, M. D., Yin, H., Landick, R., Gelles, J. & Block, S. M. Stretching DNA with optical tweezers. *Biophysical Journal* **72**, 1335-1346 (1997).
2. Van de Hulst, H. C. *Light scattering by small particles* (Wiley, New York, 1957).
3. Ashkin, A. Forces of a single-beam gradient laser trap on a dielectric sphere in the ray optics regime. *Biophysical Journal* **61**, 569-582 (1992).
4. Ashkin, A., Dziedzic, J. M., Bjorkholm, J. E. & Chu, S. Observation of a single-beam gradient force optical trap for dielectric particles. *Optics Letters* **11**, 288-290 (1986).
5. Neuman, K. C. & Block, S. M. Optical trapping. *Review of Scientific Instruments* **75**, 2787-2809 (2004).
6. Malagnino, N., Pesce, G., Sasso, A. & Arimondo, E. Measurements of trapping efficiency and stiffness in optical tweezers. *Optics Communications* **214**, 15-24 (2002).
7. Felgner, H., Muller, O. & Schliwa, M. Calibration of light forces in optical tweezers. *Applied Optics* **34**, 977-982 (1995).
8. Berg-Sorensen, K. & Flyvbjerg, H. Power spectrum analysis for optical tweezers. *Review of Scientific Instruments* **75**, 594-612 (2004).
9. Svoboda, K. & Block, S. M. Biological applications of optical forces. *Annual Review of Biophysics and Biomolecular Structure* **23**, 247-285 (1994).
10. Gittes, F. & Schmidt, C. F. Interference model for back-focal-plane displacement detection in optical tweezers. *Opt. Lett.* **23**, 7-9 (1998).
11. Finer, J. T., Simmons, R. M. & Spudich, J. A. Single myosin molecule mechanics - piconewton forces and nanometer steps. *Nature* **368**, 113-119 (1994).
12. Svoboda, K., Schmidt, C. F., Schnapp, B. J. & Block, S. M. Direct observation of kinesin stepping by optical trapping interferometry. *Nature* **365**, 721-727 (1993).
13. Jeney, S., Stelzer, E. H. K., Grubmuller, H. & Florin, E. L. Mechanical properties of single motor molecules studied by three-dimensional thermal force probing in optical tweezers. *Chemphyschem* **5**, 1150-1158 (2004).
14. Mehta, A. D., Rief, M., Spudich, J. A., Smith, D. A. & Simmons, R. M. Single-molecule biomechanics with optical methods. *Science* **283**, 1689-1695 (1999).
15. Meiners, J.-C. & Quake, S. R. Direct measurement of hydrodynamic cross correlations between two particles in an external potential. *Physical Review Letters* **82**, 2211 LP - 2214 (1999).

Chapter 4

Novel beam shaping

4.1 Synopsis

The use of Gaussian beams for optical manipulation applications has been very successful. The ability to tightly focus a Gaussian beam gives rise to transverse and axial gradient forces allowing optical tweezing of micrometer sized objects. However, a tightly focused Gaussian beam rapidly diverges away from the focus. The axial range over which the Gaussian beam can be utilised for optical manipulation is therefore limited. For some applications, such as optical guiding, novel beams have useful properties. Over a finite range, the transverse intensity profile of a Bessel beam does not spread. The central core can therefore maintain a small beam waist over a much larger propagation range than a Gaussian beam, allowing for the extended optical guiding of objects.¹ Unlike the Gaussian beam, the transverse intensity profile of the Bessel beam is able to reform around an object, allowing the beam to manipulate multiple objects. The Bessel beam can also be used to optically sort objects that have different physical characteristics.²

Other novel beams can also be applied to optical manipulation. The optical vortex can be used to optically trap and rotate objects such as dielectric spheres, hollow spheres,³ reflective and absorptive particles^{4,5} and metal nanoparticles.⁶ The optical rotation of microscopic objects has been useful for channeling fluid through microfluidic devices⁷

and for microrheology to determine the viscous properties of fluids.^{8,9} Like the Bessel beam, the transverse intensity profile of an Airy beam does not spread as it propagates. The Airy beam can be used to guide objects along a parabolic path for optical clearing applications.¹⁰

This chapter describes the properties of the optical vortex, the Bessel beam and the Airy beam. Methods to generate these beams are described, including the use of computer generated holograms. Computer generated holograms can be designed to impose any phase profile on an incident beam. Holograms can sculpt the phase profile of an incident beam such that novel beam shapes can be produced. These novel beams have proved useful for many applications including optical cell sorting,¹¹ optical clearing¹⁰ and optical microrheology.⁸ The spatial light modulator (SLM) is introduced, which is a device that can display computer generated holograms. Displaying computer generated holograms on an SLM has allowed arrays of three dimensional optical traps to be generated as well as arbitrary transverse arrangements of optical traps.¹²⁻¹⁴ Due to their flexibility, computer generated holograms are now the primary method for generating novel beams.

4.2 Optical vortices

4.2.1 What are optical vortices?

Optical vortices (also called Laguerre Gaussian or LG beams) are the optical analogues of fluid vortices such as tornadoes. Both types of vortices have a central singularity and momentum around that singularity. An optical vortex has a spiral phase front and an integer 2π phase shift around the circumference of the beam. The phase at the centre of the beam is undefined and results in a dark central core or singularity. Thus, the transverse intensity profile of an optical vortex is a ring of light. The number of 2π phase shifts around the beam circumference is described by the azimuthal index. An optical vortex with an azimuthal index l has a phase shift of $2\pi l$ around the beam circumference. A vortex with a negative value of l has a spiral phase front with the opposite helicity to that of a vortex with a l value of the same magnitude but positive polarity. The radial mode index, p , is related to the number of concentric bright rings,

N_r , present in the vortex such that $N_r = (p+1)$. In this thesis, we are only concerned with optical vortices that have one bright ring ($p = 0$).

The momentum around the vortex singularity is termed orbital angular momentum. This is a result of the beam's spiral phase front. The Poynting vector represents energy flow and is always perpendicular to the wavefront. Since optical vortices have an inclined wavefront with respect to the optic axis, the Poynting vector has an azimuthal component, which gives rise to orbital angular momentum. Figure 4.1 illustrates how the transverse intensity profile and azimuthal phase of an optical vortex change with l value. Each photon in the beam has $l\hbar$ orbital angular momentum.

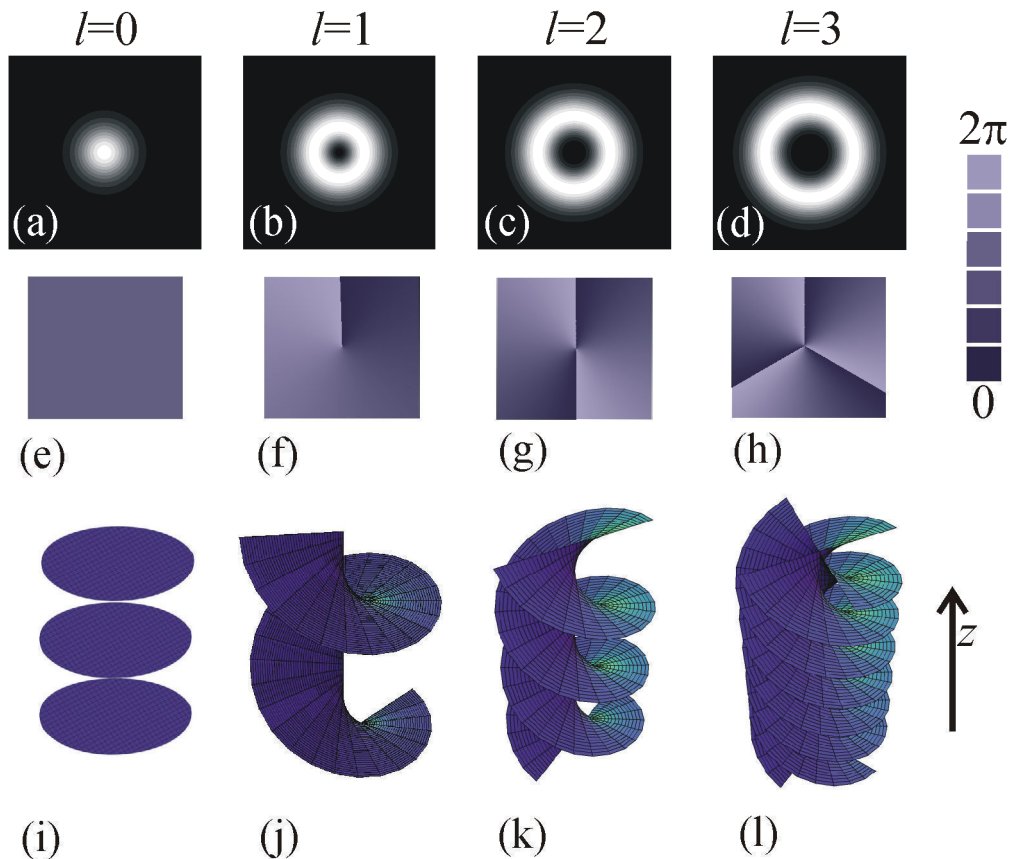


Figure 4.1. Simulated intensity profiles of Laguerre Gaussian beams with $p = 0$ and (a) $l = 0$ (b) $l = 1$, (c) $l = 2$ and (d) $l = 3$ are shown. The corresponding azimuthal phase is shown below the intensity profiles in (d), (e), (f) and (g), where the colour chart shows the corresponding phase. Three dimensional representations of the phase fronts are shown in (i), (j), (k) and (l) with vertical propagation axis z .

The equation describing the scalar field of a narrowband optical vortex is a solution to the paraxial wave equation and is given by¹⁵

$$\begin{aligned}
u_p^l(r, \phi, z) \propto & \exp\left(-\frac{ikr^2}{2R(z)}\right) \exp\left(-\frac{r^2}{w^2(z)}\right) \exp(-i(2p+l+1)\Phi) \\
& \times \exp(-il\phi) (-1)^p \left(2\frac{r^2}{w^2(z)}\right)^{\frac{l}{2}} L_p^l\left(\frac{2r^2}{w^2(z)}\right)
\end{aligned} \tag{4.1}$$

where k is the wavenumber, r , ϕ and z are the cylindrical co-ordinates, l is the azimuthal index, p is the radial mode index, $L_p^l(2r^2/w^2(z))$ is the Laguerre polynomial, $\exp(-il\phi)$ is the azimuthal phase term and $w(z)$ is the beam waist measured at a propagation distance z . The Gouy phase shift is contained in the term $\exp(-i(2p+l+1)\Phi)$, with $\Phi = \tan^{-1}(z/z_r)$ where $z_r = \pi w_0^2/\lambda$ is the Rayleigh range and w_0 is the beam waist in the focal plane. The beam waist as a function of z , $w(z)$, and the radius of curvature of the wavefront, $R(z)$, are:

$$R(z) = z \left(1 + \left(\frac{z_r}{z} \right)^2 \right), \tag{4.2}$$

$$w(z) = w_0 \sqrt{1 + \left(\frac{\lambda z}{\pi w_0} \right)^2}. \tag{4.3}$$

The transverse intensity profile for a Laguerre Gaussian beam is¹⁶

$$I(r, z) = \frac{2p!}{\pi(p+|l|)!} \frac{P_0}{w^2(z)} \exp\left(-2\frac{r^2}{w^2(z)}\right) \left(\frac{2r^2}{w^2(z)}\right)^{|l|} \left\{ L_p^{|l|}\left(\frac{2r^2}{w^2(z)}\right) \right\}^2, \tag{4.4}$$

where P_0 is power. The radius of the maximum intensity, $r_{\max l}(z)$, varies as a function of l according to¹⁷

$$r_{\max l}(z) = \frac{\sqrt{2w(z)}}{2} \sqrt{l}. \tag{4.5}$$

4.2.2 Angular momentum

4.2.2.1 Spin angular momentum

There are two types of angular momentum: orbital and spin. Both can be transferred to microscopic objects. In this thesis, we are only concerned with orbital angular momentum, but for completeness, spin angular momentum is briefly explained here. Spin

angular momentum (SAM) arises in a beam that is circularly or elliptically polarized. In such beams the electric field vector rotates around the z axis as illustrated in Figure 4.2.



Figure 4.2. The electric field vector of a circularly polarized wave is indicated by the blue arrows. The angle of the electric field vector varies along the propagation axis z .

The conservation of angular momentum is a fundamental law of physics. It is the statement that the total angular momentum in a closed system must remain the same. Conservation of momentum explains why spin angular momentum can rotate birefringent objects. Each photon has $\pm \hbar$ spin angular momentum, where $\hbar = h/(2\pi)$ and h is Planck's constant. If such photons interact with a birefringent object, the spin angular momentum can be transferred to that object either by absorption or scattering.¹⁸ An object that absorbs a photon with SAM also absorbs the angular momentum of the photon and experiences a torque as a result. If a photon with SAM scatters from an object, the polarization state of the photon may be changed as a result. In order to conserve angular momentum in the system, the SAM lost by the photon must be transferred to the object. Momentum must be transferred to an object that is involved in a scattering process with a photon that has SAM, and this transferred momentum must be equal to the difference between the momentum of the photon before the collision and the momentum of the photon after the collision.

It was first shown that circularly polarized light could be used to rotate a quartz half waveplate in 1936 by Beth.¹⁹ Left circularly polarized light propagating upwards through the half waveplate was converted into right circularly polarized light. The right circularly polarized light was then reflected back downwards through the half waveplate (the polarization is then again left circular due to the reflection). The light passing through the half waveplate, in both the upwards and downwards directions, was always left circularly polarized causing the plate to rotate due to the conservation of angular momentum. This was the initial important result that inspired many more investigations into the transfer of

angular momentum to objects. More recently, Friese *et al.*²⁰ demonstrated the transfer of spin angular momentum to birefringent calcite particles in an optical tweezers setup. The calcite particles can behave as microscopic waveplates. Light incident on such a particle experiences a different phase shift in the ordinary and extraordinary axes of the particle, if a change in the angular momentum of the light occurs as a result, there will be a torque on the material causing it to rotate.

4.2.2.2 Orbital angular momentum

Orbital angular momentum (OAM) arises in beams that have an azimuthal component to their phase profile. Therefore it is distinct from spin angular momentum, which arises due to polarization effects. Optical vortices have a spiral phase front and therefore have orbital angular momentum. The Poynting vector \mathbf{S} , which represents energy flux, in any beam is always perpendicular to the phase front. So for a beam with a spiral phase front, the Poynting vector rotates at an inclined angle with respect to the propagation direction. The angular momentum density, \mathbf{j} , is related to the Poynting vector by²¹

$$\mathbf{j} = \mathbf{r} \times \mathbf{S}, \quad (4.6)$$

where

$$\mathbf{S} = \varepsilon_0 \mathbf{E} \times \mathbf{B}. \quad (4.7)$$

The total angular momentum of the field, \mathbf{J}_t , is

$$\mathbf{J}_t = \int \mathbf{r} \times \mathbf{S} d\mathbf{r}, \quad (4.8)$$

where \mathbf{r} is the radius vector and ε_0 is the vacuum permittivity of free space. The total angular momentum of the field is equal to the sum of the orbital and spin contributions. If the light is linearly polarized, then there is no spin angular momentum and the contribution to the total angular momentum \mathbf{J}_t is in the form of orbital angular momentum only, we now call this \mathbf{J} . The Poynting vector in a beam with a spiral phase front has an azimuthal component. Therefore, there is an azimuthal component to the momentum resulting in non-zero orbital angular momentum. Orbital angular momentum can be transferred to objects through scattering and absorption processes causing the objects to rotate. This idea can be pictured intuitively by visualising an object rolling around the spiral phase front of a vortex beam. Figure 4.3(a) depicts the transfer of orbital

angular momentum to a microsphere and Figure 4.3(b) shows the Poynting, radius and momentum density vectors present in a beam with a spiral phase front.

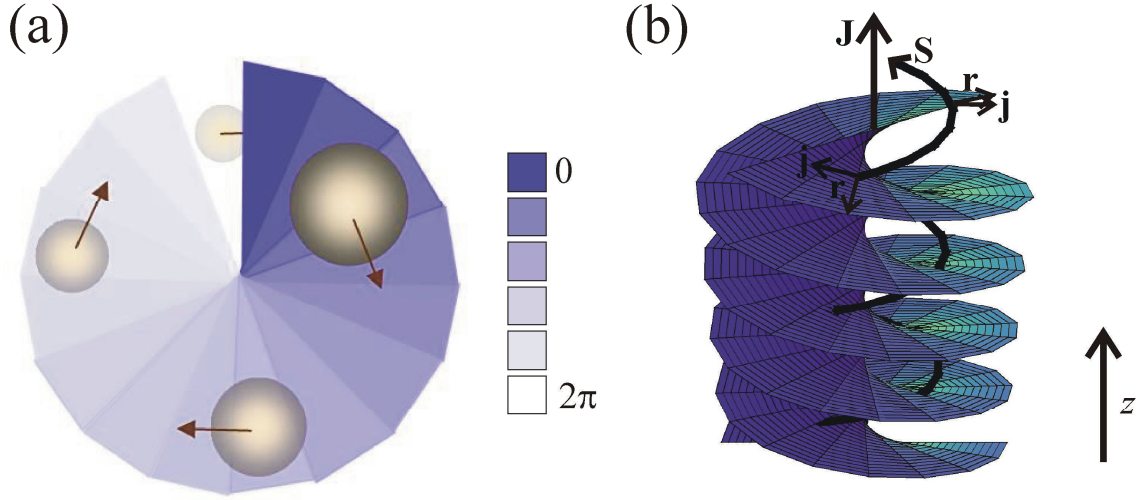


Figure 4.3. A trapped sphere is illustrated travelling around a spiral phase front in image (a) and the colour chart shows the value of the phase in this image. The darkest colour represents a phase of zero, white represents a phase of 2π and the other shades represent intermediate phase values. Image (b) shows that the Poynting vector has an azimuthal component when there is a spiral phase front. Also shown are some of the radius and momentum density vectors. When the total orbital angular momentum is averaged over the beam, only the axial component of the OAM averages to a non-zero value. The direction of the total orbital angular momentum \mathbf{J} is shown. If the helicity of the phase front is reversed, by changing the l value of the vortex from positive to negative, the total momentum is then directed in the negative z direction.

The transfer of orbital angular momentum to objects can be demonstrated by focusing an optical vortex into a sample of microspheres immersed in water. A microsphere orbiting in an optical vortex will experience a drag force as a result of the surrounding fluid. The torque due to the drag force, τ_{drag} , is given in Equation 4.9. The sphere will also experience a torque, τ_{OAM} , due to the orbital angular momentum of the vortex.²² The equations for τ_{OAM} and τ_{drag} are shown below along with the total torque denoted by τ .

$$\tau_{drag} = -6\pi\eta\omega_r r_{max}^2 a, \quad (4.9)$$

$$\tau_{OAM} = \frac{P_{beam}}{2\pi f} l = \frac{\rho_{laser} a^2}{2f} l, \quad (4.10)$$

$$\tau = |\tau_{OAM}| - |\tau_{drag}| = \frac{\rho_{laser} a^2}{2f} l - 6\pi\eta\omega_r r_{max}^2 a, \quad (4.11)$$

where η is the viscosity of the medium surrounding the microsphere, ρ_{laser} is the laser power optical density, ω_r is the angular velocity of the rotating object, r_{max} is the radius

of the maximum intensity of the beam, a is the radius of the microsphere, P_{beam} is the power of the beam, f is the frequency of light and l is the azimuthal index of the vortex.

Another way to view the transfer of orbital angular momentum to an object is to think of individual photons. Each photon has $\pm l\hbar$ orbital angular momentum that can be transferred to an object. When a photon scatters from an object, the orbital angular momentum of the photon is changed, and the difference between the OAM of the photon before scattering and after scattering is transferred to the object. Similarly, if a photon with OAM is absorbed by an object, then the OAM of the photon is transferred to the object. The same is true for photons with linear momentum or spin angular momentum.

4.2.3 Generating optical vortices

There are several ways to generate optical vortices each with advantages and disadvantages. Some of these methods will be discussed briefly but the emphasis will be on the method used during this research, namely computer generated holograms displayed on a spatial light modulator. Since a vortex has a $2\pi l$ phase shift around its circumference, it is intuitive to think of using a spiral piece of glass with varying thickness to introduce an azimuthally dependent phase delay on a Gaussian beam. This does in fact work and the object introducing the phase delay is called a spiral phase plate (or optical vortex lens). Beijersbergen *et al.*²³ were the first to demonstrate the use of a spiral phase plate for the generation of an optical vortex. Since then, achromatic spiral phase plates have been developed for use with broadband sources.²⁴ A broad bandwidth optical vortex generated using an achromatic spiral phase plate has all the wavelength components overlapped. Another advantage of spiral phase plates is that they can be used with high power laser sources.

Another way to generate an optical vortex is by using a mode convertor. Petrov *et al.*²⁵ used a cylindrical mode convertor to convert two fundamental HG_{00} modes that are out of phase with each other and oriented at 45° to each other into a L_0^1 mode. As with a spiral phase plate, mode convertors can be used with high power beams.

However, for the generation of high power optical vortices, there is a simpler method than mode conversion. Volyar *et al.*^{26,27} showed that an optical vortex can be generated by focusing a Gaussian beam into a uniaxial crystal placed between crossed polarizers. However, in order to generate vortices with higher l values, the beam must be sent through the same arrangement of polarizers and crystals repeatedly. Thus, large changes must be made each time the vortex parameters are to be altered.

Computer generated holograms can be used to impose a phase profile on an incident beam and produce novel beam shapes. The beam that is generated after being incident on the hologram has a complex amplitude, $u(r)$, described by²⁸

$$u(r) = u_0(r) \exp(i\psi(r)), \quad (4.12)$$

where $u_0(r)$ is the complex amplitude of the beam incident on the SLM and $\psi(r)$ is the phase imposed on the beam by the hologram.

Equations 4.13 and 4.14 show $\psi(r)$ required to generate a hologram to make an LG beam. Equation 4.13 shows $\psi(r)$ for applying a spiral phase when no grating is added to the hologram. Equation 4.14 shows $\psi(r)$ for applying a spiral phase front with a grating added to the hologram.¹⁵ The reason for adding a grating to the hologram is explained in Section 4.6.

$$\psi(r) = \text{mod}(l\phi, 2\pi), \quad (4.13)$$

$$\psi(r) = \text{mod}\left(l\phi - \frac{2\pi}{\Lambda} r \cos \phi, 2\pi\right), \quad (4.14)$$

where $\text{mod}(a,b)$ gives the remainder of a/b and Λ is the grating spacing. The spiral phase hologram, phase grating hologram and the resulting hologram used to generate an optical vortex are shown in Figure 4.4. The resulting holograms have a fork dislocation in the centre. The number of lines in the grating is different at the top and bottom of the hologram. This difference depends on the value of l . For example, Figure 4.4 shows that for $l=1$ there is one more line at the top of the grating than at the bottom. Similarly, for $l=2$ there are two more lines at the top of the grating than at the bottom.

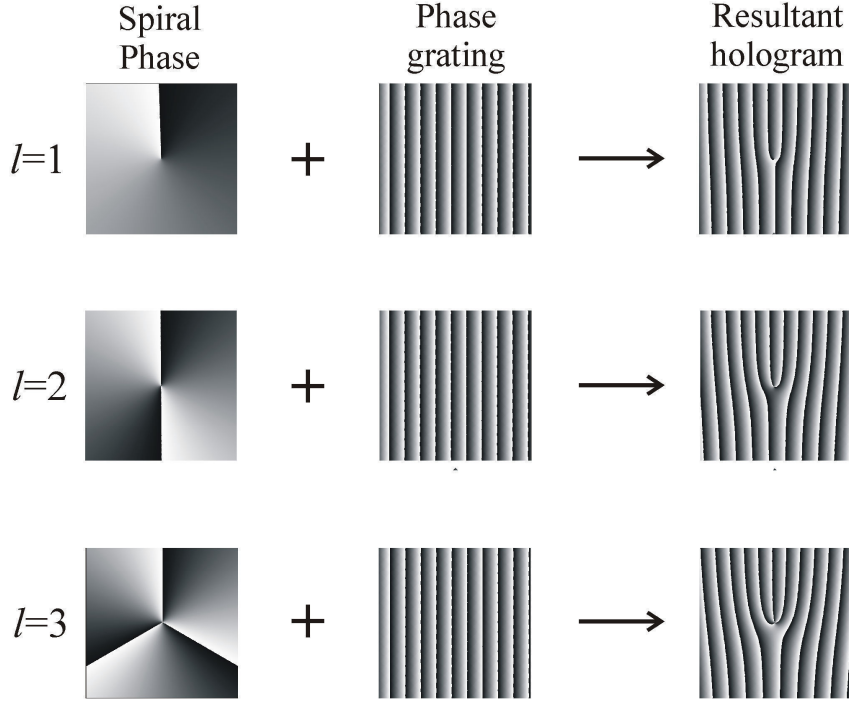


Figure 4.4. Typical ‘forked’ holograms used to generate optical vortices with $p = 0$ and $l = 1$, $l = 2$ and $l = 3$ are shown. Also shown are the phase and grating holograms that are combined to give the forked holograms. Black represents a phase of zero and white represents a phase of 2π .

4.3 Bessel beams

4.3.1 Introduction to Bessel beams

The idea of the Bessel beam first arose in 1987 when Durnin²⁹ spotted the Bessel solution to the Helmholtz equation. The first experimental realisation of the equivalent optical beam soon followed.³⁰ The electric field, $E(r, \phi, z)$, of a theoretical Bessel beam is given by³¹

$$E(r, \phi, z) = E_0 \exp(ik_z z) J_m(k_r r) \exp(\pm in\phi), \quad (4.15)$$

where E_0 is the field amplitude, k_z and k_r are wavevectors ($k = \sqrt{k_z^2 + k_r^2}$), J_m is the Bessel function of m^{th} order and r , ϕ and z are cylindrical co-ordinates. A zero order Bessel beam has a transverse intensity profile with a bright central spot surrounded by concentric rings. Higher order Bessel beams also have a transverse intensity profile of concentric rings but without the central bright spot. The transverse intensity profiles of Bessel beams with different m values are shown in Figure 4.5. In this thesis, we are only

concerned with zero order Bessel beams ($m = 0$). The energy of the Bessel beam is distributed equally between the rings.

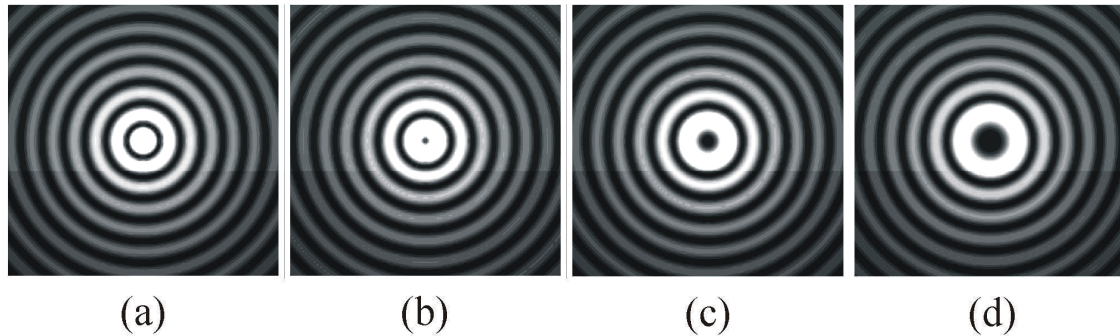


Figure 4.5. The simulated transverse intensity profiles for a Bessel beam with (a) $m = 0$, (b) $m = 1$, (c) $m = 2$ and (d) $m = 3$ are shown.

The initial draw of the Bessel beam lay in its ability to propagate ‘diffraction-free.’ The idea of a beam that was immune to diffraction was intriguing to many and generated great interest. In theory, the intensity profile of a zero order Bessel beam can propagate for an infinite distance without spreading. In practice, the beam can propagate ‘diffraction-free’ for only a finite distance. This is because an infinite ‘diffraction-free’ propagation distance would require the Bessel beam to have an infinite number of intensity rings and therefore infinite energy. However, an approximation to the ideal Bessel beam, which has a finite ‘diffraction-free’ propagation distance and finite energy, can be generated in the lab.

After further investigation, another surprising property was discovered: the Bessel beam can reconstruct beyond obstructions placed in its path.^{32,33} The reason for this will be explained in the next section when Bessel beam generation is explained.

4.3.2 Generating Bessel beams

There are several methods that can be used to generate a Bessel beam. The three that will be outlined in this section are illustrated in Figure 4.6. The simplest method to generate a Bessel beam involves the use of an annulus and a lens. The inverse Fourier transform of a Bessel beam is a ring of light. Therefore, a lens can be used to Fourier transform a ring of light to produce a Bessel beam. Experimentally, this means illuminating an annulus

placed at the back focal plane of a lens with a Gaussian beam. A conical wavefront is generated after the lens and these waves interfere to produce a Bessel beam. The maximum ‘diffraction-free’ propagation distance of this beam, z_{\max} , depends on the radius, R_{lens} , and focal length, f_{lens} , of the lens and the diameter of the annulus, d_a , such that³¹

$$z_{\max} = \frac{R_{\text{lens}}}{\tan \gamma}, \quad (4.16)$$

$$\tan \gamma = \frac{d_a}{2f_{\text{lens}}}. \quad (4.17)$$

However, this way of generating a Bessel beam is inefficient because the majority of light from the Gaussian beam is blocked at the annulus. Figure 4.6(a) illustrates this Bessel beam generation method.

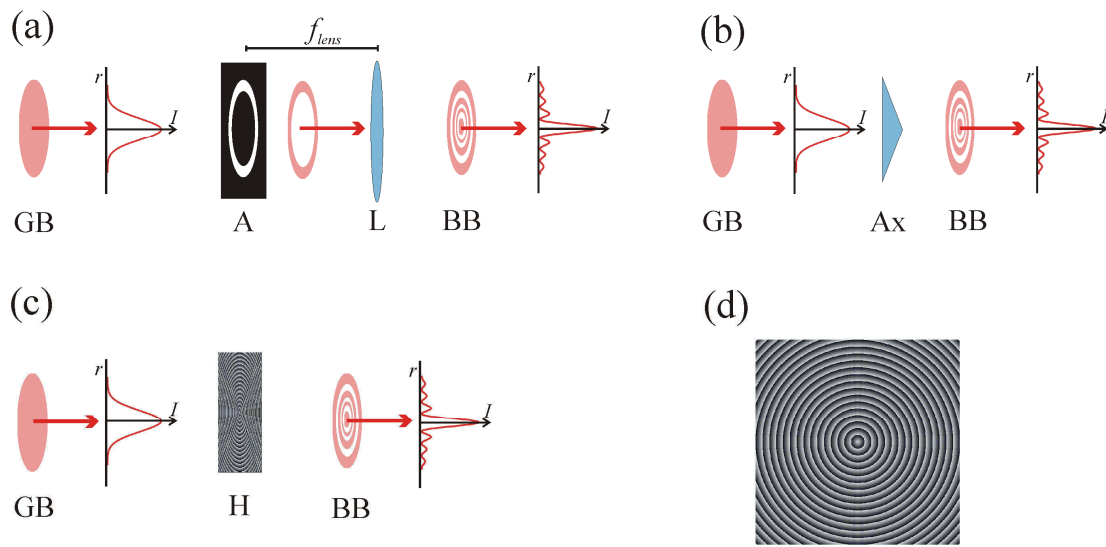


Figure 4.6. Image (a) shows a Bessel beam, BB, generated by illuminating an annulus, A, placed at the back focal plane of a lens, L, with a Gaussian beam, GB. Image (b) shows how a conical lens, known as an axicon, Ax, can be used to generate a Bessel beam. Image (c) shows that a Gaussian beam that is incident on an appropriate hologram, H, can generate a Bessel beam. A typical hologram used to generate a Bessel beam is shown in image (d).

A more efficient way to generate a Bessel beam is to use a conical lens known as an axicon. When a Gaussian beam is incident on an axicon, a conical wavefront is generated that interferes to produce a zero order Bessel beam. Higher order Bessel beams can be produced by illuminating an axicon with a Laguerre Gaussian beam.³⁴ The maximum ‘diffraction-free’ propagation distance of a beam generated this way depends on the

refractive index of the axicon material, n_x , the base angle of the axicon, α , and the waist of the incident beam, w_{inc} , such that³¹

$$z_{\max} = \frac{k}{k_r} w_{inc} \approx \frac{w_{inc}}{(n_x - 1)\alpha}, \quad (4.18)$$

where k and k_r are wavevectors as defined earlier. It is clear from Equation 4.18 that a larger beam waist results in a larger maximum ‘diffraction-free’ propagation distance. Also, a smaller value of α results in a larger value of z_{\max} .

The most versatile method for generating a Bessel beam is the use of a computer generated hologram. This allows immediate control over the parameters of the beam produced and is the method employed in the experiments presented in Chapter 8. The hologram can replicate the phase of a Gaussian beam that has propagated through an axicon. The function $\psi(r)$ that can be substituted into Equation 4.12 to generate a Bessel beam is³⁵

$$\psi(r) = \text{mod}\left(m\phi + \frac{2\pi}{\lambda} r \tan \alpha, 2\pi\right), \quad (4.19)$$

where α is the base angle of the axicon, r and ϕ are the cylindrical co-ordinates and m is the order of the Bessel function.

Now that Bessel beam generation has been explained, the beam’s self-healing property can be understood. The Bessel beam is an interference pattern generated by waves propagating on a conical wavefront. If an obstruction is placed in the path of the beam, the beam will reform at some distance after the obstruction. The obstruction blocks some of the incoming waves, but the waves that pass the obstruction are able to interfere and reform the Bessel beam. Figure 4.7(a) shows how a Bessel beam is generated using an axicon and Figure 4.7(b) shows how the beam is able to reconstruct around an obstruction.

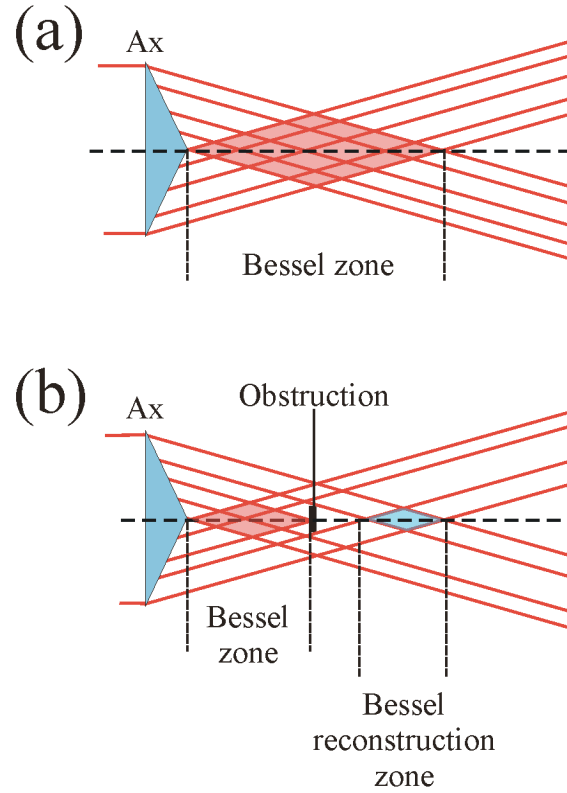


Figure 4.7. The axicon is indicated by Ax. The ‘Bessel zone’ is the region where the waves interfere to produce a Bessel beam. Illustration (a) shows how conical waves form a Bessel beam. Illustration (b) shows how a Bessel beam can form around an obstruction placed in the beam path. The ‘Bessel reconstruction zone’ is the area where the Bessel beam reforms after the obstruction.

From Figure 4.7, it can be seen that the rays entering the axicon close to the optic axis are responsible for constructing the Bessel beam nearest to the axicon. The rays entering the axicon far away from the optic axis construct the beam further away from the axicon. As long as some of the outer rays pass the obstruction, the Bessel beam will reconstruct. The minimum distance that it takes the Bessel beam to reconstruct around an obstruction, z_{\min} , is related to the wavevectors k and k_r by

$$z_{\min} \approx \frac{r_{obs} k}{k_r}, \quad (4.20)$$

where r_{obs} is the radius of the obstruction measured from the centre of the beam.

The Bessel beam has proved useful for many applications including optical sorting,^{2,36} optical guiding¹ and optical transfection.³⁷ The Bessel beam also lends itself to trapping elongated objects such as micrometer sized rods and e-coli, or trapping multiple spheres stacked on top of each other.¹ The advantage of the Bessel beam over a Gaussian beam for these applications is that the Gaussian beam focuses to a small spot and immediately expands, whereas the Bessel beam retains a small central core size over the ‘diffraction-free’ propagation distance. For the optical transfection of cells, a Gaussian beam has to be positioned accurately in the z axis to ensure the focal point of the beam is incident on the cell. The use of a Bessel beam for optical transfection removes the requirement to align the beam so accurately along the z axis.

4.4 Airy beams

4.4.1 Introduction to Airy beams

The idea for the Airy beam arose after Berry and Balazs³⁸ discovered the Airy wavepacket solution to the Schrödinger equation in 1979. The analogy between the Schrödinger equation and the paraxial wave equation made it possible to find a solution that could be used to describe an optical Airy beam. The first optical Airy beam was experimentally realized³⁹ 28 years after the initial discovery of Berry and Balazs.

The Airy beam is another example of a ‘non-diffracting’ beam. Just like the Bessel beam, the Airy beam can theoretically propagate for an infinite distance without spreading. Again, in order to propagate ‘diffraction-free’ for an infinite distance, infinite energy would be required, which is of course not possible. However, an approximation to the ideal Airy beam can be realised optically. The resistance to diffraction for a real Airy beam is only possible over a finite distance because of the finite energy of the system. The experimentally realisable Airy beam is referred to as the ‘finite Airy beam.’

Like the Bessel beam, the Airy beam can reconstruct after encountering an obstruction.^{33,40} This remarkable ability is due to the fact that both beams are generated as a result of an interference pattern. In the case of the Bessel beam, it is the interference

of conical waves. For the Airy beam, it is the interference of waves with a cubic phase front. When an obstruction is placed in the beam path, as long as some waves are able to pass the obstruction, the waves can interfere beyond it and reconstruct the beam.

Aside from their ‘non-diffracting’ and reconstruction properties, Airy beams have an even more unusual feature: they propagate along a parabolic trajectory. The Airy beam experiences an acceleration transverse to its propagation direction resulting in the beam’s parabolic trajectory. An analogy can be drawn between the behaviour of a projectile in a gravitational field and the propagation characteristics of an Airy beam.⁴¹ To look at the propagation another way, the waves that generate the Airy beam interfere constructively along a parabolic path.

The transverse intensity profile of the two dimensional Airy beam has side lobes of decreasing intensity forming a triangular arrangement around the main, and brightest, lobe. Figure 4.8 shows an example of the transverse intensity profile for a 1D and 2D Airy beam. In this thesis, we are only concerned with two dimensional Airy beams.

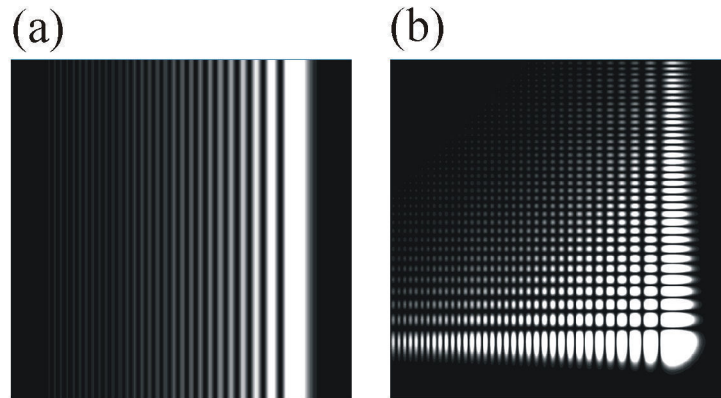


Figure 4.8. The transverse intensity profiles for a 1D (a) and 2D (b) Airy beam are shown. The 1D Airy beam has side lobes only in one transverse direction whilst the 2D Airy beam has lobes in both the x and y directions.

4.4.2 Generating an Airy beam

To allow the experimental realisation of the Airy beam, a finite equivalent to the Airy wavepacket solution³⁸ to the Schrödinger equation had to be found. This was made possible because of the introduction of an aperture function, $\exp(a_0 s)$, by Siviloglou *et*

al.³⁹ The 2D finite Airy beam solution to the paraxial wave equation is given in Equation 4.21.⁴²

$$u(\xi, s) = Ai\left(s_x - \left(\frac{\xi}{2}\right)^2 + ia_0\xi\right) Ai\left(s_y - \left(\frac{\xi}{2}\right)^2 + ia_0\xi\right) \times \exp\left(a_0s_x + a_0s_y - \left(\frac{a_0\xi^2}{2}\right) - i\left(\frac{\xi^3}{6}\right) - i\left(\frac{a_0^2\xi}{2}\right) + i\xi\left(\frac{s_x + s_y}{2}\right)\right), \quad (4.21)$$

The solution at $\xi = 0$ is shown in Equation 4.22.

$$u(x, y, \xi = 0) = Ai\left(\frac{x}{x_0}\right) \exp\left(\frac{a_0x}{x_0}\right) Ai\left(\frac{y}{y_0}\right) \exp\left(\frac{a_0y}{y_0}\right), \quad (4.22)$$

where $s_x = x/x_0$, $s_y = y/y_0$, $\xi = z/kx_0^2$, Ai denotes the Airy function, x_0 and y_0 are the characteristic lengths in the x and y directions respectively and a_0 is the aperture coefficient. The characteristic lengths are related to the spacing of the lobes in the transverse axes. The aperture coefficient is responsible for limiting the propagation distance of the beam. At this point another coefficient is introduced that characterises the parabolic propagation of the beam. It is the deflection coefficient and is denoted by b_0 , where $b_0 = 1/(4k^2x_0^3)$. The deflection coefficient is obtained from the argument of the Airy function in Equation 4.21. More detail about these properties is given in the next section.

To generate an Airy beam, a computer generated hologram can be used to impose a cubic phase shift on the incident beam. A lens placed at the focal distance from the hologram takes the Fourier transform to generate the Airy beam in the Fourier plane of the lens. The image of a typical hologram used to generate a 2D Airy beam is shown in Figure 4.9.

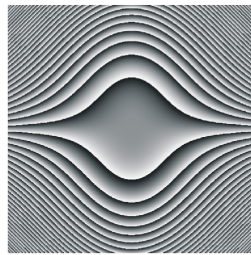


Figure 4.9. Above is an example of a typical hologram used to generate a 2D Airy beam. The hologram imposes a cubic phase on an incident beam. If the resultant beam is then focused through a lens, a finite Airy beam is produced.

The Airy beam is not circularly symmetric so Cartesian co-ordinates are used to describe the beam. If Equation 4.12 is presented in Cartesian co-ordinates, the function $\psi(x, y)$ that can be substituted into Equation 4.12 to generate a finite Airy beam is

$$\psi(x, y) = \text{mod}\left(\frac{1}{3}(x^3 + y^3) + ax + by, 2\pi\right), \quad (4.23)$$

where a and b are constants and ax and by give rise to a phase grating in the x and y axes respectively.

4.4.3 Properties of Airy beams

This section aims to describe how the deflection coefficient, aperture coefficient and characteristic length parameters affect the Airy beam's propagation and transverse intensity profile. The deflection coefficient, b_0 , describes the steepness of the parabolic propagation when the parabola is described by $x_m = b_0 z^2$. An Airy beam with a larger value deflection coefficient has a steeper propagation parabola, see Figure 4.10(a).

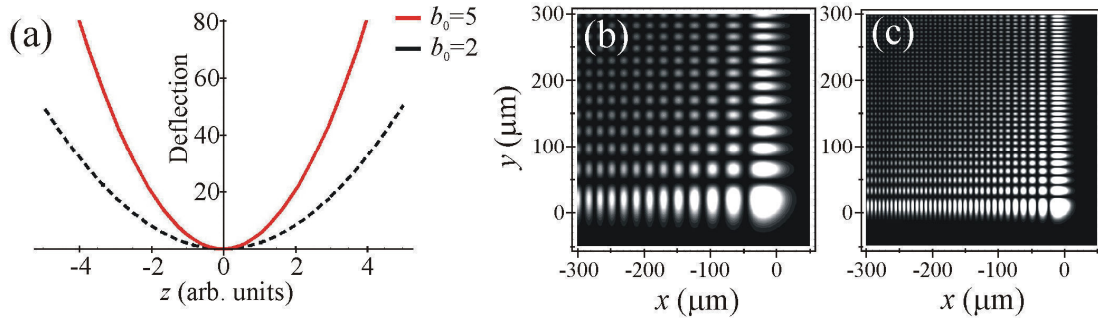


Figure 4.10. The simulated parabolas shown in (a) have the equation $x_m = b_0 z^2$. The parabola with a higher b_0 value is steeper; the deflection is stated in arbitrary units. Images (b) and (c) show simulated transverse intensity profiles of a 2D Airy beam. Both images have $a_0 = 0.004$. Image (b) has $x_0 = y_0 = 20\mu\text{m}$ and (c) has $x_0 = y_0 = 10\mu\text{m}$.

Next, the significance of the characteristic length of the Airy beam is explained. Figures 4.10(b) and (c) show contour plots of the transverse cross-sections of Airy beams with different characteristic length values. Larger x_0 and y_0 values give rise to an Airy beam with larger spacing between the beam's lobes.

The aperture coefficient is responsible for limiting the number of lobes present in the Airy beam and for limiting the 'diffraction-free' propagation distance of the beam. The

transverse intensity profiles of a finite 2D Airy beam with $a_0 = 0.05$, and an ideal Airy beam with $a_0 = 0$ are shown in Figure 4.11. The finite Airy beam ($a_0 > 0$) has lobes that decay as the distances from the main lobe increases, whilst the perfect Airy beam has lobes that disappear at an infinite distance from the main lobe. A high value of a_0 results in an Airy beam with lobes which decrease in amplitude rapidly as the distance from the main lobe increases. Also shown are modelled images of the Airy beam's propagation. The beam with a higher a_0 value has fewer lobes and propagates for a shorter distance than the beam with a lower a_0 value.

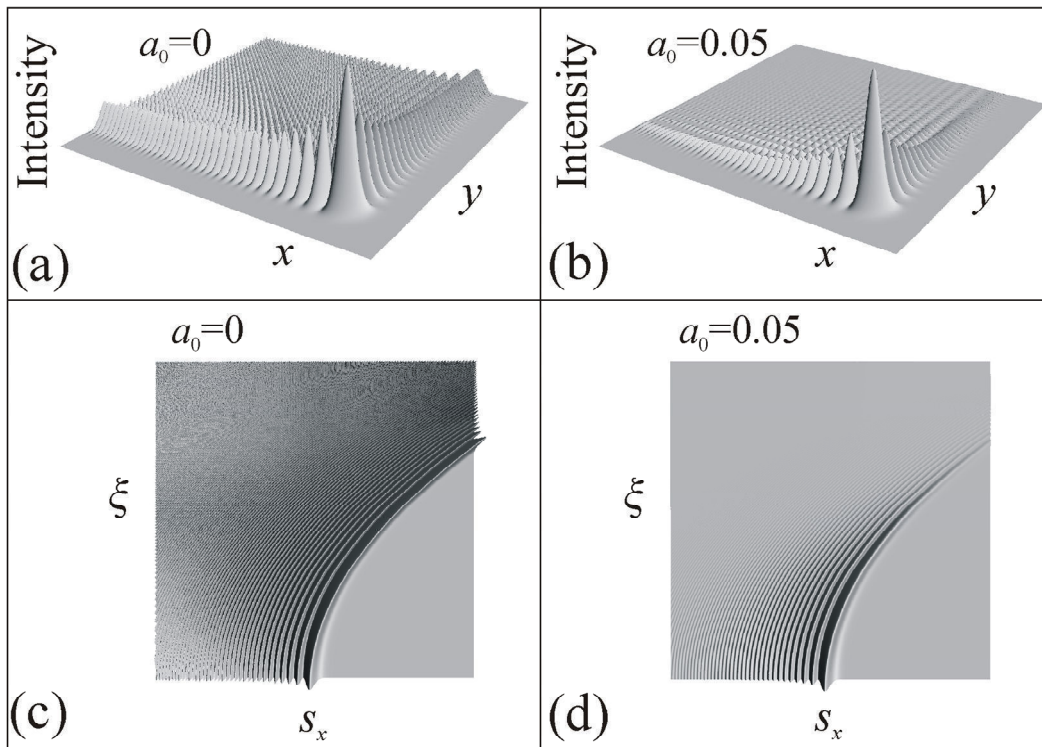


Figure 4.11. Image (a) is of an Airy beam with $a_0 = 0$, image (b) is of a finite Airy beam with $a_0 = 0.05$. Image (c) is the propagation of an Airy beam with $a_0 = 0$ and image (d) is the propagation of an Airy beam with $a_0 = 0.05$.

The Airy beam's parabolic trajectory has already proved interesting for optical clearing applications. Baumgartl *et al.*¹⁰ placed microspheres in four separated microwell compartments. They found that particles in one compartment can be drawn into the Airy beam and propagated along the beam's parabolic path before dropping out into a different compartment. This process was termed 'optical clearing' because the spheres can be

cleared from a chosen compartment in this way. Recently, the Airy beam has been used to generate a plasma channel along a parabolic path.⁴³ Femtosecond pulses were used to ionize the air and generate the plasma. As the filament (or plasma) is formed, broadband light is emitted in the forward direction. With a beam that propagates in a straight line, all of the forward emissions are overlapped in the transverse viewing plane and cannot be resolved. When the beam propagates along a parabola, the emissions are spread out along the transverse observation plane allowing information about the pulse dynamics to be determined from the far-field spectra produced.

Although there have been investigations into some of the Airy beam's properties, namely the behaviour of the Poynting vector and angular momentum,⁴² there has not yet been a full characterisation of the beam's propagation parameters. Chapter 7 details the characterisation of the Airy beam's parabolic trajectory, its lobe spacing and aperture coefficient in relation to the wavelength and spatial coherence of the source. In the same way that the beam waist, Rayleigh range and wavelength characterise the Gaussian beam, the deflection coefficient, characteristic length and aperture coefficient characterise the Airy beam.

4.5 The spatial light modulator

The generation of novel beam shapes has been made easier and more flexible with the invention of the spatial light modulator (SLM). A spatial light modulator has a liquid crystal display that is able to modulate the amplitude and phase of incident light to create a wide variety of beam shapes. A pixilated display is used and the pixels are given information either electrically or optically. When choosing an SLM, there is the option of a nematic or ferroelectric device. Ferroelectric SLMs are capable of a higher repetition rate than nematic devices. However, the pixels on ferroelectric SLMs are only able to modulate the phase in a binary manner e.g. either 0 or π , whereas nematic SLMs can modulate the phase by a range of values (in phase steps of $2\pi/256$) between 0 and 2π . During this research only electrically addressed nematic spatial light modulators are used. This is because the high repetition rate of a ferroelectric device was not required, and nematic devices provide more precise control over the applied phase.

The display of an electrically addressed nematic SLM consists of birefringent liquid crystals. There are silicon pixilated electrodes on one side of the crystals and a transparent electrode on the other side. The orientation of the liquid crystals at a location depends on the magnitude of the voltage applied to the nearest pixel. The crystals line up in a preferred orientation when there is no electric field present, but as an increasing electric field is applied the orientation of the crystals begins to align with the electric field. The refractive index of each pixel can therefore be controlled by modulating the voltage applied to each silicon pixel in the display as shown in Figure 4.12. As such, a spatial light modulator allows control over the phase modulation applied to an incident beam. Holograms can be designed using a computer and then displayed on the SLM. This allows almost complete control over the phase profile imposed on an incident beam. The computer generated hologram can be an 8-bit per pixel bitmap image where black (greyscale level 0) represents a phase of 0 and white (greyscale level 255) represents a phase of 2π .

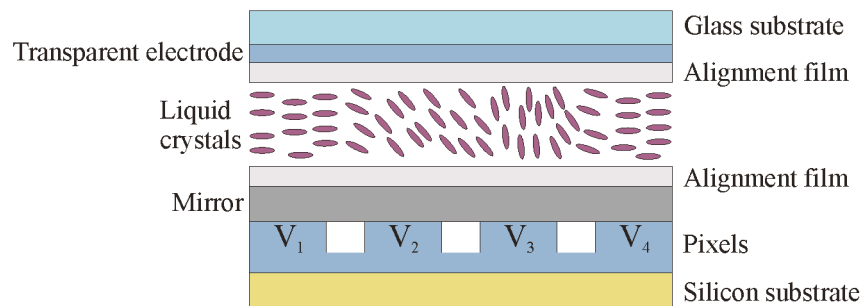


Figure 4.12. The pixels are electrodes and each has a different voltage applied. The liquid crystals then orient themselves according to the applied voltage. The phase of incoming light through the glass substrate has a phase modulation applied by the liquid crystal layer. The newly modulated light is then reflected by the mirror and exits the device through the glass substrate. Image adapted from reference [44].⁴⁴

Table 4.1 details the specifications of the two spatial light modulators that were used during this research. SLM 1 is the Holoeye 2500 and SLM 2 is the Hamamatsu x10468-03. Both SLMs use a liquid crystal on silicon display (LCOS).

When generating novel beams, the necessary use of optical elements such as lenses can introduce aberrations to the wavefront. Even the face of the SLM can introduce unwanted aberrations if it is not perfectly flat. The use of computer generated holograms with spatial light modulators allows for correction of wavefront aberrations. A method to achieve wavefront correction is presented in Appendix A.

Table 4.1.

	SLM 1	SLM 2
Number of pixels:	1024x768	792x600
Pixel pitch:	19 μ m	20 μ m
Display area:	19.6x14.6mm	16x12mm
Repetition rate:	72Hz	60Hz
Wavelength:	400-700nm	1000-1100nm
Fill factor:	93%	95%

4.6 Generating novel beams using a spatial light modulator

One of the main advantages of using computer generated holograms is that the parameters of the beam can be easily changed. The first use of a computer generated hologram in optical tweezing, including its first use to generate an optical vortex,⁴⁵ was in 1999. The versatility of computer generated holograms for beam shaping has made this the most popular method for advancing the possibilities of optical manipulation. Particularly for generating optical vortices, computer generated holograms have the advantage that the vortex parameters, such as the azimuthal index and the radial mode index, can be changed at the click of a button. However, the reflected light from the surface of the SLM display and the diffracted light from the gaps between the pixels do not undergo phase modulation. This un-modulated light overlaps with the phase modulated light. The addition of a blazed grating to the hologram spatially separates the modulated and un-modulated light. If the SLM device was perfect then higher orders of diffraction would not be produced. However, the pixelation of the SLM device means that a completely smooth phase transition from 0 to 2π in each line of the grating is not possible. This gives rise to higher diffraction orders. Figure 4.13(a) illustrates the overlap of the modulated and un-modulated beams that are produced using a hologram designed to generate a $l=1$ vortex with no grating displayed on the hologram. Figure 4.13(b) shows how the modulated and un-modulated beams can be separated when a grating is

added to the hologram. Finally, Figure 4.13(c) shows how a lens and an aperture can be used to isolate a chosen beam for use.

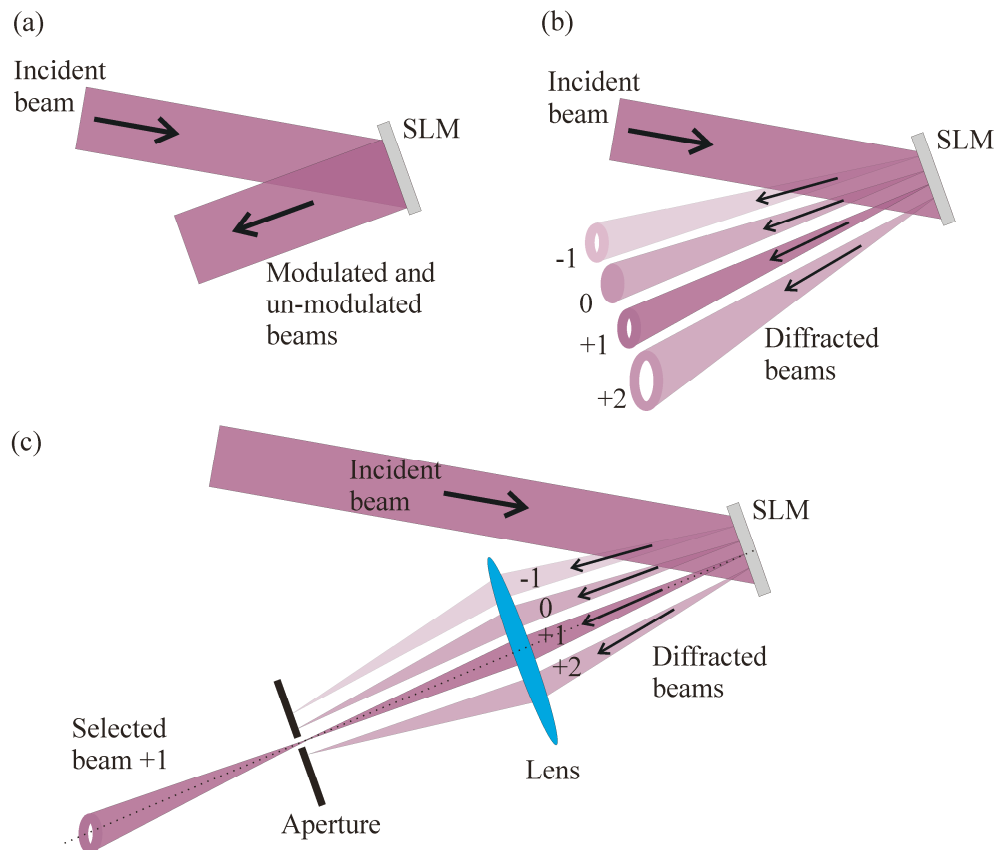


Figure 4.13. When the SLM displays a hologram with a spiral phase profile, an optical vortex is produced. Due to reflection from the surface of the SLM and diffraction caused by the gaps between the pixels, un-modulated light is always present. If no grating is applied to the hologram, the modulated light and un-modulated light overlap as in illustration (a). When the SLM displays such a hologram with a superimposed grating, the modulated and un-modulated light is spatially separated as shown in illustration (b). Illustration (c) shows that a lens and aperture can be used to select the modulated beam and block the un-modulated beam. Imperfections in the SLM device result in the production of higher diffraction orders from the grating. Some power is lost due to the unwanted beams. Orders higher than +2 and lower than -1 are also produced but are not shown in this illustration. The combination of the phase hologram and the grating hologram causes the diffracted beams to take the form of optical vortices. For a hologram designed to produce a vortex with $l = 1$, the +1 order beam has $l = +1$, the +2 order beam has $l = +2$ and the -1 order beam has $l = -1$.

High powers incident on an SLM will damage the liquid crystal display. This limits the maximum possible power in a beam generated using a computer generated hologram displayed on an SLM. However, the versatility of the computer generated hologram is usually such a great advantage that it outweighs this issue.

4.7 Broadband novel beams

Generating novel beam shapes using a broad bandwidth source opens up new avenues of investigation into the coherence properties of light. Investigations into the first ‘white light’ Bessel beam lead to interesting insights into the role that coherence plays in the generation of this beam.⁴⁶ A narrowband optical vortex has orbital angular momentum. The generation of an optical vortex using a broad bandwidth source provides insight into the effect of low temporal coherence on the orbital angular momentum of light. Broad bandwidth lasers are also extremely useful for investigating the wavelength dependent properties of novel beams. Wavelengths can be selected from the laser beam using filters and the properties of novel beams can be observed without changing the experimental setup.

To generate a ‘white light’ novel beam using a computer generated hologram, adjustments must be made to the setup shown in Figure 4.13. Dispersion must be taken into account because of the wavelength dependence of diffracted light. A technique for dispersion compensation using a prism was first demonstrated by Leach *et al.*⁴⁷ Figure 4.14 illustrates how the dispersion of a broad bandwidth beam can be compensated using a prism. The example in Figure 4.14 is for the generation of an optical vortex, but a similar arrangement can be applied for other novel beams generated in this way. The hologram is imaged onto a prism with opposite dispersion to that of the hologram grating. A similar setup is used to compensate dispersion in the experiments presented in Chapters 5 - 7. The position of the centre of the beam is different for each wavelength component due to dispersion. The prism can compensate the dispersion and overlap the beam centres to produce a ‘white light’ beam. The prism does not compensate any other wavelength dependent effects.

The phase range of a spatial light modulator is dependent on the wavelength of the incident light, even if there is no dispersion occurring due to the liquid crystals. This is because the distance travelled through the device is the same for each wavelength, but light with a shorter wavelength goes through a larger number of phase cycles than light with a longer wavelength in that distance.

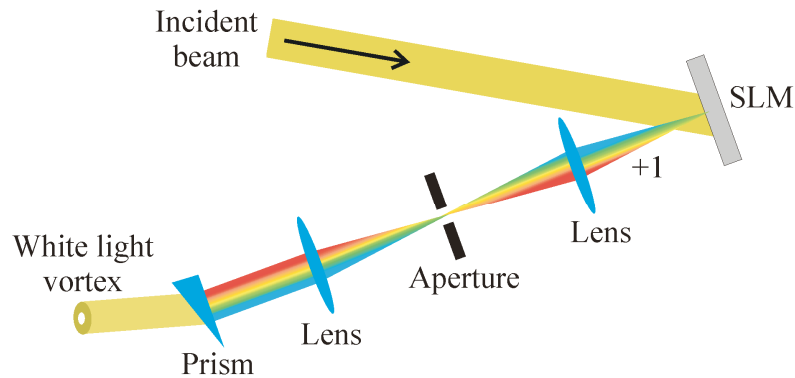


Figure 4.14. The dispersion from a diffraction grating can be compensated by imaging the hologram onto a prism of opposite dispersion. Only the +1 diffraction order is shown, other diffraction orders exist but were omitted from the illustration for clarity. SLM denotes the spatial light modulator. The example of dispersion compensation for a 'white light' optical vortex is shown. The same principle applies to the generation of other 'white light' novel beams.

4.8 Conclusion

Three types of novel beams have been introduced: the optical vortex (or Laguerre Gaussian beam), the Bessel beam and the Airy beam. The optical vortex has a spiral phase front giving rise to orbital angular momentum, which can be transferred to microscopic objects to make them rotate. Beams that are circularly or elliptically polarized have spin angular momentum, which can be used to rotate birefringent objects. The use of orbital angular momentum, as opposed to spin angular momentum, to rotate objects has the advantage that the objects do not have to be birefringent. Orbital angular momentum can be transferred to a range of objects including dielectric spheres, hollow spheres³ and nanometer scale objects.⁶

The Bessel beam can propagate 'diffraction-free' for a finite distance. Unlike a focused Gaussian beam, which diverges rapidly after the focus, the Bessel beam can maintain a small central core along its 'diffraction-free' propagation distance. This property makes the Bessel beam particularly useful for the extended optical guiding of particles.¹ The Bessel beam can also reconstruct around obstructions placed in the beam path. The Bessel beam is therefore more robust than the Gaussian beam and can reconstruct around one object allowing manipulation of another object positioned further along the beam path.

The Airy beam is also a ‘diffraction-free’ beam that can reconstruct around obstructions but has the unusual property of propagating along a parabolic path. The Airy beam can draw objects into the main lobe of the beam and guide them along a parabolic trajectory. This could be useful for optical clearing applications.¹⁰

All of the beams mentioned above can be generated using holograms. The spatial light modulator is a device that can be used to display computer generated holograms. The holograms impose a new phase profile on an incident beam. The resulting beam can have novel properties as described above. The use of a broadband beam with diffractive optics results in dispersion due to the wavelength dependent diffraction angle. This dispersion can be compensated by imaging the hologram onto a prism of opposite dispersion.

References

1. Arlt, J., Garces-Chavez, V., Sibbett, W. & Dholakia, K. Optical micromanipulation using a Bessel light beam. *Optics Communications* **197**, 239-245 (2001).
2. Paterson, L. et al. Light-induced cell separation in a tailored optical landscape. *Applied Physics Letters* **87** (2005).
3. Gahagan, K. T. & Swartzlander, J., G. A. Optical vortex trapping of particles. *Opt. Lett.* **21**, 827-829 (1996).
4. He, H., Heckenberg, N. R. & Rubinsztein-Dunlop, H. Optical-particle trapping with higher-order doughnut beams produced using high-efficiency computer-Generated Holograms. *Journal of Modern Optics* **42**, 217-223 (1995).
5. He, H., Friese, M. E. J., Heckenberg, N. R. & Rubinsztein-Dunlop, H. Direct observation of transfer of angular momentum to absorptive particles from a laser beam with a phase singularity. *Physical Review Letters* **75**, 826 LP - 829 (1995).
6. Dienerowitz, M., Mazilu, M., Reece, P. J., Krauss, T. F. & Dholakia, K. Optical vortex trap for resonant confinement of metal nanoparticles. *Optics Express* **16**, 4991-4999 (2008).
7. Ladavac, K. & Grier, D. Microoptomechanical pumps assembled and driven by holographic optical vortex arrays. *Opt. Express* **12**, 1144-1149 (2004).
8. Yao, A., Tassieri, M., Padgett, M. & Cooper, J. Microrheology with optical tweezers. *Lab Chip* **9**, 2568-75 (2009).
9. Bishop, A. I., Nieminen, T. A., Heckenberg, N. R. & Rubinsztein-Dunlop, H. Optical microrheology using rotating laser-trapped particles. *Physical Review Letters* **92**, 198104 (2004).
10. Baumgartl, J., Mazilu, M. & Dholakia, K. Optically mediated particle clearing using Airy wavepackets. *Nat Photon* **2**, 675-678 (2008).

11. Paterson, L. et al. Passive optical separation within a 'nondiffracting' light beam. *Journal of Biomedical Optics* **12** (2007).
12. Curtis, J. E., Koss, B. A. & Grier, D. G. Dynamic holographic optical tweezers. *Optics Communications* **207**, 169-175 (2002).
13. Melville, H. et al. Optical trapping of three-dimensional structures using dynamic holograms. *Optics Express* **11**, 3562-3567 (2003).
14. Bingelyte, V., Leach, J., Courtial, J. & Padgett, M. J. Optically controlled three-dimensional rotation of microscopic objects. *Applied Physics Letters* **82**, 829-831 (2003).
15. Arlt, J., Dholakia, K., Allen, L. & Padgett, M. J. The production of multiringed Laguerre-Gaussian modes by computer-generated holograms. *Journal of Modern Optics* **45**, 1231-1237 (1998).
16. Gherardi, D. M. *Studies of particle and atom manipulation using free space light beams and photonic crystal fibres* (University of St Andrews, Thesis, 2008).
17. Allen, L., Padgett, M. J. & Babiker, M. in *Progress in optics XXXIX* 294-372 (Elsevier Science, Amsterdam, 1999).
18. Parkin, S., Knoner, G., Nieminen, T. A., Heckenberg, N. R. & Rubinsztein-Dunlop, H. Measurement of the total optical angular momentum transfer in optical tweezers. *Optics Express* **14**, 6963-6970 (2006).
19. Beth, R. A. Mechanical detection and measurement of the angular momentum of light. *Physical Review* **50**, 115-125 (1936).
20. Friese, M. E. J., Nieminen, T. A., Heckenberg, N. R. & Rubinsztein-Dunlop, H. Optical alignment and spinning of laser-trapped microscopic particles. *Nature* **394**, 348-350 (1998).
21. Allen, L., Beijersbergen, M. W., Spreeuw, R. J. C. & Woerdman, J. P. Orbital angular-momentum of light and the transformation of Laguerre-Gaussian laser modes. *Physical Review A* **45**, 8185-8189 (1992).
22. Tao, S. H., Yuan, X. C., Lin, J. & Sun, Y. Y. Influence of geometric shape of optically trapped particles on the optical rotation induced by vortex beams. *Journal of Applied Physics* **100** (2006).
23. Beijersbergen, M. W., Coerwinkel, R. P. C., Kristensen, M. & Woerdman, J. P. Helical-wave-front laser-beams produced with a spiral phaseplate. *Optics Communications* **112**, 321-327 (1994).
24. Swartzlander, G. A. Achromatic optical vortex lens. *Optics Letters* **31**, 2042-2044 (2006).
25. Petrov, D. V., Canal, F. & Torner, L. A simple method to generate optical beams with a screw phase dislocation. *Optics Communications* **143**, 265-267 (1997).
26. Volyar, A. et al. Generation of single-charge optical vortices with an uniaxial crystal. *Optics Express* **14**, 3724-3729 (2006).
27. Volyar, A. V. & Fadeeva, T. A. Generation of singular beams in uniaxial crystals. *Optics and Spectroscopy* **94**, 235-244 (2003).
28. McGloin, D., Spalding, G., Melville, H., Sibbett, W. & Dholakia, K. Applications of spatial light modulators in atom optics. *Opt. Express* **11**, 158-166 (2003).
29. Durnin, J. Exact-solutions for nondiffracting beams .1. The scalar theory. *Journal of the Optical Society of America a-Optics Image Science and Vision* **4**, 651-654 (1987).

30. Durnin, J., Miceli, J. J. & Eberly, J. H. Diffraction-free beams. *Physical Review Letters* **58**, 1499-1501 (1987).
31. McGloin, D. & Dholakia, K. Bessel beams: diffraction in a new light. *Contemporary Physics* **46**, 15-28 (2005).
32. MacDonald, R. P., Boothroyd, S. A., Okamoto, T., Chrostowski, J. & Syrett, B. A. Interboard optical data distribution by Bessel beam shadowing. *Optics Communications* **122**, 169-177 (1996).
33. Bouchal, Z., Wagner, J. & Chlup, M. Self-reconstruction of a distorted nondiffracting beam. *Optics Communications* **151**, 207-211 (1998).
34. Arlt, J. & Dholakia, K. Generation of high-order Bessel beams by use of an axicon. *Optics Communications* **177**, 297-301 (2000).
35. Milne, G. in *Optical sorting and manipulation of microscopic particles* pg98 (Thesis: University of St Andrews, 2007).
36. Milne, G., Paterson, L., McGloin, D., Riches, A. & Dholakia, K. Light induced separation and flow of microscopic and biological particles. *Nanomanipulation with Light* **5736**, 46-53 (2005).
37. Tsampoula, X. et al. Femtosecond cellular transfection using a nondiffracting light beam. *Applied Physics Letters* **91** (2007).
38. Berry, M. V. & Balazs, N. L. Non-spreading wave packets. *American Journal of Physics* **47**, 264-267 (1979).
39. Siviloglou, G. A., Broky, J., Dogariu, A. & Christodoulides, D. N. Observation of accelerating airy beams. *Physical Review Letters* **99**, 213901 (2007).
40. Broky, J., Siviloglou, G. A., Dogariu, A. & Christodoulides, D. N. Self-healing properties of optical Airy beams. *Optics Express* **16**, 12880-12891 (2008).
41. Siviloglou, G. A., Broky, J., Dogariu, A. & Christodoulides, D. N. Ballistic dynamics of Airy beams. *Optics Letters* **33**, 207-209 (2008).
42. Sztul, H. I. & Alfano, R. R. The Poynting vector and angular momentum of Airy beams. *Optics Express* **16**, 9411-9416 (2008).
43. Polynkin, P., Kolesik, M., Moloney, J. V., Siviloglou, G. A. & Christodoulides, D. N. Curved plasma channel generation using ultraintense Airy beams. *Science* **324**, 229-232 (2009).
44. Hamamatsu. LCOS SLM x10468 hardware instruction manual. *Hamamatsu Photonics* (version 2.7).
45. Reicherter, M., Haist, T., Wagemann, E. U. & Tiziani, H. J. Optical particle trapping with computer-generated holograms written on a liquid-crystal display. *Optics Letters* **24**, 608-610 (1999).
46. Fischer, P. et al. White light propagation invariant beams. *Optics Express* **13**, 6657-6666 (2005).
47. Leach, J. & Padgett, M. J. Observation of chromatic effects near a white-light vortex. *New Journal of Physics* **5** (2003).

Chapter 5

Optical manipulation using a supercontinuum source

5.1 Synopsis and motivation

Optical manipulation is a very powerful technique that is most commonly carried out using a narrowband laser. However, the use of a broad bandwidth light source, such as a supercontinuum source, for optical manipulation can be beneficial for some applications. The supercontinuum source has good spatial coherence, which allows the beam to be tightly focused and used for optical manipulation. However, chromatic aberration occurs when focusing a broadband beam resulting in an elongated focal region. Although this is not ideal for optical tweezing, the elongated focal region can be useful for the optical guiding of objects.¹ A focused supercontinuum beam allows guiding over a larger range than is possible with a Gaussian narrowband beam. Additionally, the broad bandwidth of the supercontinuum source makes it ideal for spectroscopy applications. Spectroscopy typically involves the averaging of data obtained from multiple objects. Information about individual objects is then lost. Using a supercontinuum source, it has been demonstrated that simultaneous trapping and spectroscopy can be performed on an individual object.² This allows us to isolate a specific item and obtain spectroscopic information about that item. Information about the size, shape and refractive index of the object can be obtained. Using typical broad bandwidth sources that have low power and

low spatial coherence, it is difficult to obtain a scattering spectrum from very small objects. This is because the scattering signal from an object varies according to the size of the object as $(2a)^6$, where a is the radius of the object. The supercontinuum source produces a beam with a high intensity, which allows a scattering signal with a sufficient signal/noise ratio to be obtained from nano-scale objects. The supercontinuum source has made it possible to obtain plasmon spectra for individual gold spheres with a diameter of just 10nm.³ Aerosol water droplets have also been studied using a supercontinuum source. A water droplet was optically trapped using a supercontinuum source whilst information from the backscattering spectrum was obtained.⁴ Each water droplet behaves like a Fabry-Perot interferometer. Information from the backscattering spectra was then used to determine the dimensions of the water droplet and study the evaporation process.

The use of a supercontinuum source for optical manipulation is also useful when interference effects need to be reduced. For the above application, the interference occurs because the path difference is less than the temporal coherence length of the source. However, by separating the supercontinuum source into two beams and ensuring that the path difference between the two beams is greater than the temporal coherence length of the source, the supercontinuum source can be used for longitudinal optical binding studies that do not suffer from interference effects. Two counter-propagating beams can be used to optically trap objects. The trapped object focuses the laser to produce a new trap site for another object. This process is known as optical binding. Interference between the counter-propagating beams can hamper investigations into the effect of optical binding. The supercontinuum source has low temporal coherence and can be used to minimise interference effects for optical binding studies.⁵

This chapter describes the use of a supercontinuum source for optical manipulation. Some of the challenges involved in viewing optically manipulated objects when using a broad bandwidth source are discussed and a solution is provided. Determining the strength of an optical trap is important for many of the applications of optical manipulation, particularly in the field of biophysics where single molecule studies⁶, microrheology^{7,8} and microfluidic^{9,10} techniques are often employed. I characterised the

forces in a broadband optical trap and then carried out the first ever use of an SLM for multiple beam optical trapping with a supercontinuum source. This multiple trapping technique using a low coherence source could be useful for the study of hydrodynamic cross correlations by reducing the optical cross talk between traps.¹¹ A review of applications of a supercontinuum source is presented in Chapter 2. Additionally, I explored the use of a parabolic micromirror array as an alternative method to generate multiple broadband optical trap sites. The focal length of a parabolic mirror is wavelength independent. Parabolic mirrors therefore lend themselves well to the focusing of a broadband laser beam. A supercontinuum beam was incident on the parabolic micromirror array producing multiple optical trap sites. The 3D confinement of polymer microspheres was achieved. At the end of the chapter, an experimental setup is suggested that could be used to measure the trap stiffness values of the micromirror array traps.

5.2 Single beam optical manipulation using a supercontinuum source

The ability to illuminate the sample plane and view trapped objects whilst they are being manipulated is essential if scientific measurements are to be carried out. Section 3.2 details how this can be achieved when using a narrowband laser source for optical manipulation; a filter is placed before the CCD camera to block out only the lasing wavelength and allow the sample illumination light to be transmitted through to the CCD camera. When using a broadband source for optical manipulation, this method is not applicable. Any filter that blocks the broad bandwidth light from the camera would also block the illuminating light. A solution was found to overcome this illumination issue. The next section details the solution to the illumination issue and presents the experimental setup used for broadband optical manipulation.

5.2.1 Illuminating the sample

The principles for constructing an optical manipulation setup for use with a supercontinuum source are the same as for a narrowband laser, but there are a few additional aspects that must be taken into consideration. First of all, the issue of

chromatic aberration (see Section 2.4.1) had to be addressed. Although the elongated focal region of a supercontinuum beam has proved useful for optical guiding,¹ it can be a hindrance when it comes to optical manipulation techniques that require tight laser focusing. There are lenses that compensate for chromatic aberration such as achromatic or apochromatic lenses. Achromatic lenses are designed to focus two particular wavelengths to the same point, thus helping to avoid the elongated focal region. Apochromatic lenses are designed to focus three different wavelengths to the same point, so the aberration correction is better than in the case of achromatic lenses. However, there are also lenses available that are able to compensate for four wavelengths. These are violet corrected apochromatic lenses (VC apochromatic). For the experiments presented in Section 5.2.3 up until Section 5.4, I decided to use an objective lens that was VC apochromatic to focus our beam into the sample. This increased the chance of optically confining objects in the axial direction. The objective lens also had a high numerical aperture (Nikon $\times 100$, N.A. 1.4), which was used to maximize the axial intensity gradient of the beam. For the initial experiment, which is presented in Section 5.2.2, an objective lens with a slightly lower numerical aperture was used ($\times 100$, N.A. 1.25). This objective lens was switched for the objective lens with a higher N.A. because the three dimensional optical confinement of microspheres was not achieved. The lenses used for the supercontinuum beam in the experiments were achromatic doublet lenses (this does not refer to objective lenses).

The next issue, as encountered by Li *et al.*,² is the challenge of viewing the trapped objects. The supercontinuum beam showed up on the CCD camera to be overwhelmingly brighter than the illumination light. In the case of a narrowband laser, a filter that blocks the lasing wavelength can be placed immediately before the CCD camera. For a supercontinuum source, this is not possible because of the broad bandwidth of the beam. A solution was found that allowed clear viewing of the trapped objects as will now be discussed.

One avenue that was explored was the idea of using polarization to block out the supercontinuum beam from the CCD camera. If the supercontinuum beam was polarized

and the illumination light (from a halogen bulb) was not, placing a polarizer crossed to the direction of the trapping beam's polarization before the camera might block out the supercontinuum beam but transmit the illumination light to the camera. However, in practice, the supercontinuum light was still too bright on the camera to view the trapped sphere. This was because the objective lens, used to focus the supercontinuum beam, was not able to maintain the polarization of the beam and because the polarizers are not 100% efficient.

Next, I illuminated the sample with an LED emitting at 450nm. I placed an interference filter that transmits light with a wavelength of 450nm in front of the CCD camera. Since the spectrum of the supercontinuum source begins at around 460nm, I expected that the supercontinuum beam would be blocked from the camera using a combination of polarizers and the interference filter. In fact, the bandwidth of the interference filter was 40nm, so enough of the supercontinuum light was transmitted through the filter to overwhelm the camera. The use of a filter with a narrower bandwidth was considered but the illumination light would not be bright enough on the CCD camera for clear viewing of the trapped objects. The polarizer before the CCD camera also reduced the intensity of the illumination light incident on the CCD camera.

The next idea was to reduce the spectrum of the supercontinuum beam. I used an infrared mirror to separate the beam into two parts: one with a spectrum below 700nm and one with a spectrum above 700nm. Since there was more power in the beam that had a spectrum above 700nm (the IR region), this beam was used for the experiment. The sample plane was now illuminated with a 450nm LED, and the supercontinuum beam was blocked from the CCD camera using an interference filter (450nm, bandwidth of 40nm). Some neutral density filters were also required before the CCD camera to help block the supercontinuum beam. A Köhler illumination¹² scheme was used to control the contrast of the image and to provide uniform illumination in the sample plane. An illustration of the Köhler illumination arrangement is shown in Figure 5.1(c) along with the full experimental setup in Figure 5.1(a). The condenser aperture is used to adjust the contrast of the image observed on the camera. The field aperture is imaged onto the

sample plane and controls the size of the illuminated area. To change the brightness, the voltage applied to the LED is adjusted. This setup was used for the experiments presented in Section 5.2.2.

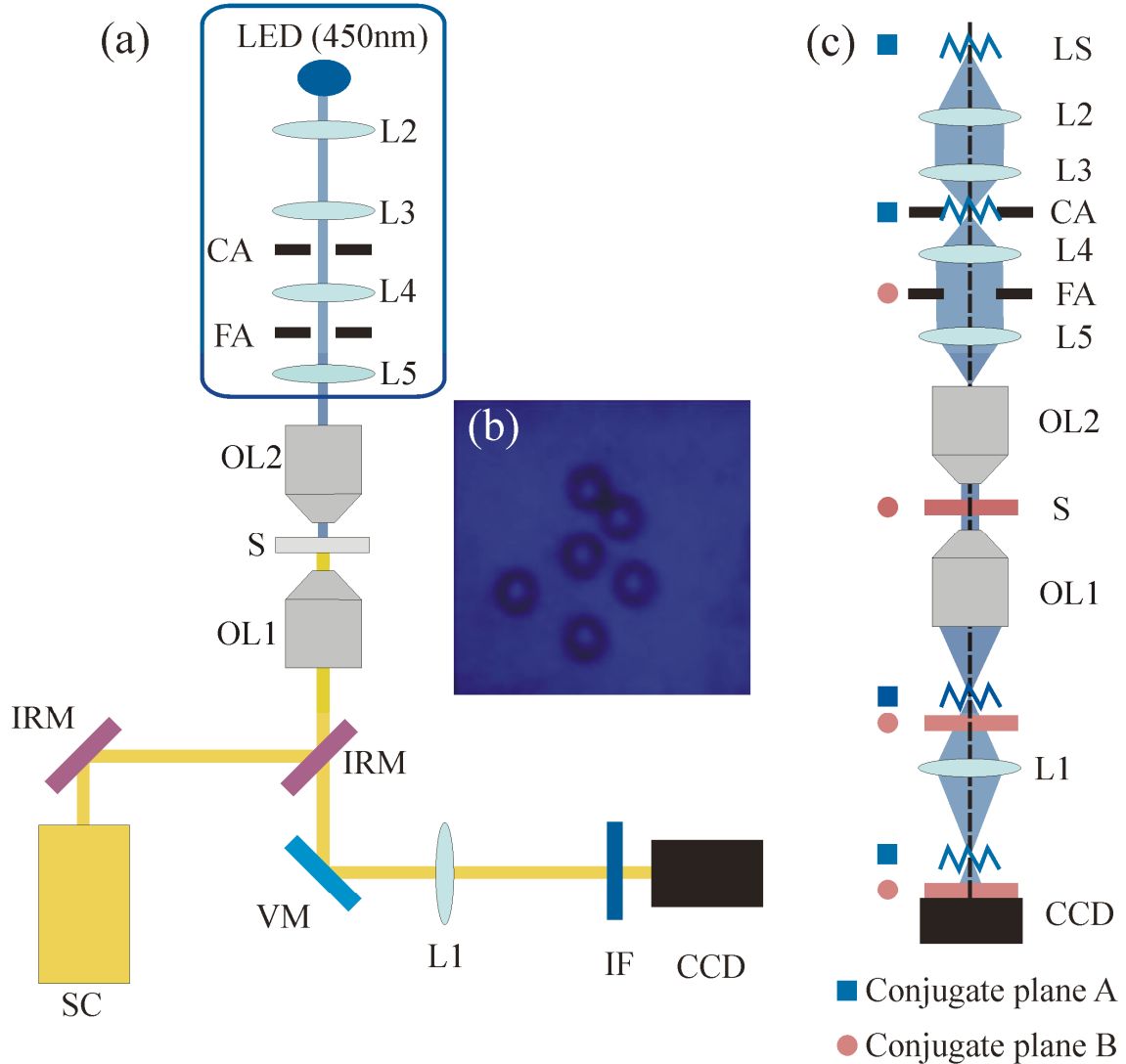


Figure 5.1. The setup using a 450nm LED for illumination and the infrared part of the supercontinuum spectrum for trapping is shown in image (a). SC is supercontinuum source, IRM represents mirrors that reflect infrared wavelengths, VM is a mirror that reflects visible wavelengths, L1 is a tube lens, IF is an interference filter that transmits light around 450nm, OL1 and OL2 are objective lenses, S is the sample and CCD is a camera. The Köhler illumination is outlined by a blue box. FA and CA are the field and condenser apertures respectively, L2 is the collimating lens and L3, L4 and L5 are lenses. Image (b) is a picture of 5µm spheres viewed using the improved illumination setup. The Köhler illumination arrangement, with conjugate planes identified, is shown in image (c), where LS is the light source.

To reduce heating effects in the trapping plane, the beam with the visible spectrum was used for the experiments ($\lambda < 700\text{nm}$). This arrangement was used for all of the experiments presented in this chapter from Section 5.2.3 onwards. In this case,

illumination of the sample plane was achieved using an LED emitting at 950nm. An interference filter that transmits only 950nm (bandwidth is 10nm) was placed before the CCD camera. Therefore, a setup has been successfully developed to view the sample when using either a broadband visible or a broadband infrared source for optical manipulation.

5.2.2 Determining the Q value of an optical trap

I investigated the Q values of a broadband optical trap for polymer spheres of diameter 1 μ m, 2 μ m, 3 μ m, 5 μ m and 10 μ m. A typical optical trapping setup was used and the infrared spectral region was selected from the supercontinuum beam using infrared reflecting mirrors (Comar 25MX05). A microscope objective ($\times 100$, N.A. 1.25) was used to focus the beam into the sample. Illumination of the sample was achieved through the same objective from below using a 450nm LED in a Köhler arrangement. The illumination light was collected and imaged onto a CCD camera using another microscope objective lens ($\times 100$, N.A. 0.7), which was placed above the trapping plane. An interference filter (bandwidth 40nm) transmitting only light with a wavelength of 450nm was placed before the CCD camera to block the supercontinuum beam. Figure 5.2 shows the spectrum of the supercontinuum source without any filtering and the spectrum of the illuminating LED.

The use of the infrared supercontinuum beam caused heating in the sample. To reduce the heating, the sample polymer spheres ($n_s = 1.59$) were immersed in D₂O instead of water because D₂O absorbs less infrared laser light than water. An extra thin PDMS (polydimethylsiloxane) sample chamber of only $18 \pm 1\mu$ m deep was also used in order to reduce the occurrence of convection currents. Coverslides were used on the top and bottom of the sample chamber. Finally, Vaseline sealed the edges of the sample to reduce capillary forces. An illustration of the sample chamber is shown in Figure 5.3.

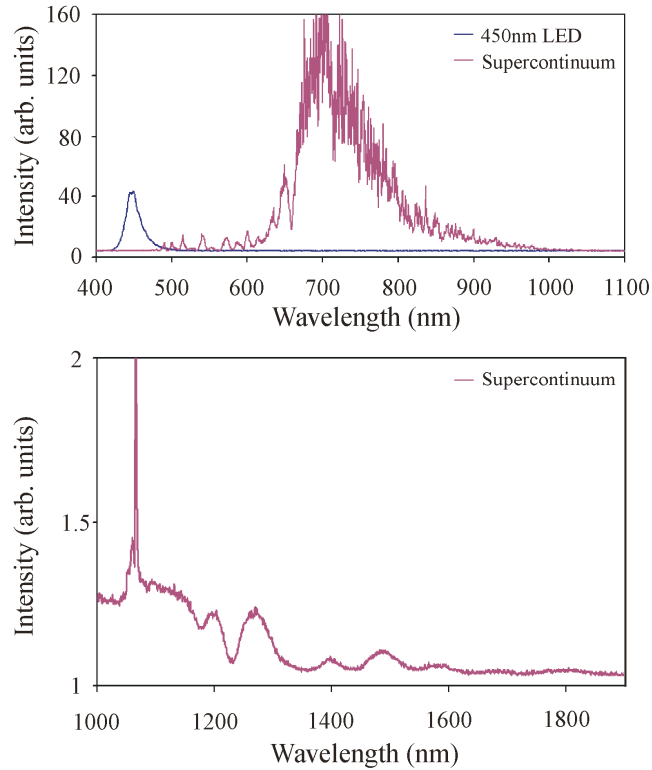


Figure 5.2. The graphs show the spectrum of the supercontinuum source and the spectrum of the 450nm LED. The Avaspec 3648 spectrometer was used to take the spectrum in the range from 300nm to 1000nm. The infrared part of the spectrum was taken using a photonics solutions APE wavescan spectrometer, which covers the wavelength range of 1000nm - 2600nm.

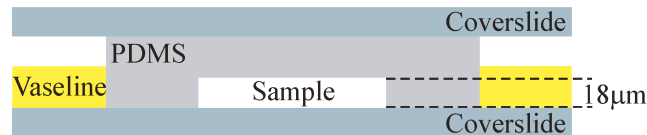


Figure 5.3. An illustration of the sample chamber is shown. Vaseline was used to seal the PDMS/coverslide boundary to reduce the presence of capillary forces acting on the sample.

Optical trapping was achieved in the transverse plane, but axial confinement was not achieved. As a result, the trapped spheres were pushed up against the top of the sample chamber. Q values were determined as described in Section 3.3.1 using Equation 3.14. The sample was translated at known velocities using a computer controlled actuator (Newport ESP 300), and the maximum velocity before the sphere escaped the optical trap was determined. Q values were also obtained using a ytterbium fibre laser emitting at 1064nm to compare with the values obtained when using the supercontinuum source. Table 5.1 shows the determined Q values for spheres of diameter 1 μ m, 2 μ m, 3 μ m, 5 μ m and 10 μ m. Each Q value was measured five times and the average value was determined.

The full width half maximum value of the supercontinuum trapping beam was $1.54\mu\text{m}$ and for the 1064nm laser trapping beam was $1.4\mu\text{m}$.

Table 5.1

Sphere diameter (μm)	Q values 1064nm laser	Q values supercontinuum
1	0.063 ± 0.001	0.029 ± 0.003
2	0.172 ± 0.023	0.080 ± 0.008
3	0.187 ± 0.026	0.089 ± 0.009
5	0.169 ± 0.024	0.110 ± 0.011
10	0.142 ± 0.015	0.059 ± 0.009

The random uncertainty was derived using the five values determined for each sphere size. I can conclude from Table 5.1 that the Q values for the broadband optical trap were always lower than those for the 1064nm laser trap. The Q values measured for the broadband optical trap were less than those measured for the narrowband laser because the supercontinuum beam spot is not Gaussian. It is a superposition of the focal spots from the different wavelength components in the beam (refer back to Section 2.4.1). Also, the spot size of the broadband beam was slightly larger than for the narrowband beam.

5.2.3 Optical tweezing of silica spheres

The aim in this section was to measure the trap stiffness values of different sized microspheres in a broadband optical tweezers. I was able to optically tweeze silica spheres ($n_s \sim 1.43-1.46$, immersed in water) of 780nm, 970nm and $1.28\mu\text{m}$ diameter. The supercontinuum beam was focused to a spot size of 640nm (FWHM) in the trapping plane. Samples of spheres were made using $80\mu\text{m}$ deep cylindrical chambers (vinyl spacers) sealed on top with a 1mm thick microscope slide and on the bottom with a thin glass coverslip. Due to the short working distance (0.13mm) of the microscope objective lens (Nikon $\times 100$, N.A. 1.4), zero thickness coverslips were used to seal the bottom of the chamber. Illumination of the sample plane was achieved using a LED emitting at 950nm as described at the end of Section 5.2.1. The visible spectrum of the

supercontinuum beam was used in this experiment. The spectrum is shown in Figure 5.4 along with the experimental setup.

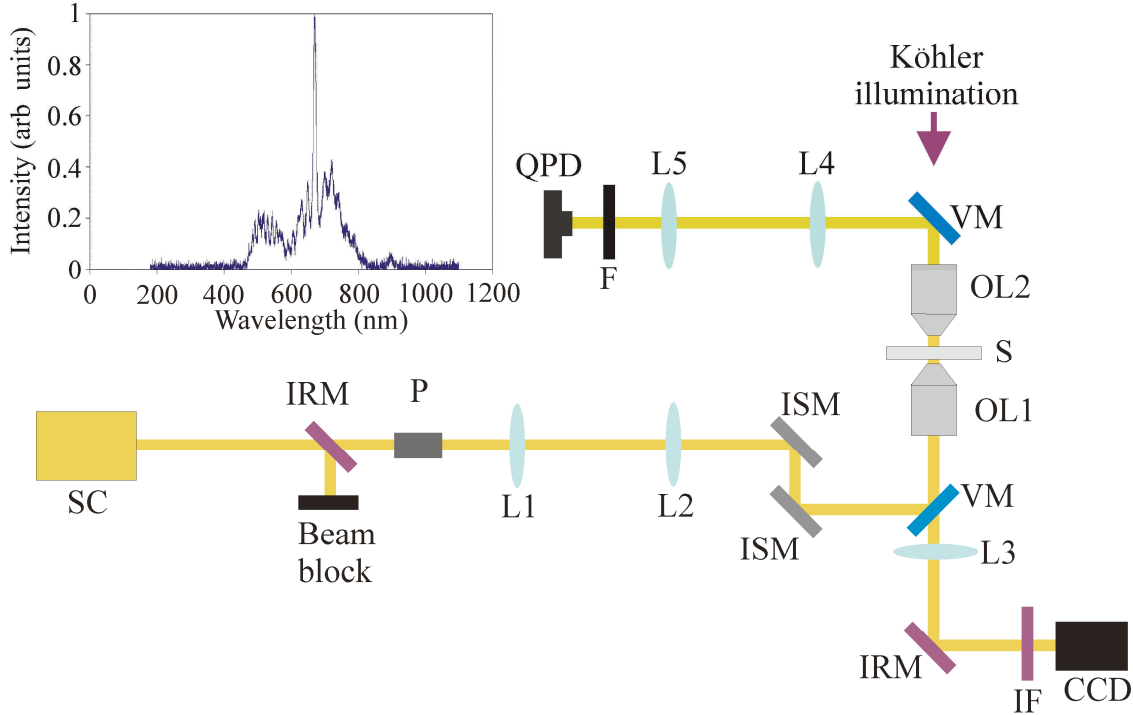


Figure 5.4. The setup is shown above. SC is the supercontinuum source, IRM is an infrared mirror, P is a polarizer, ISM is an ion-beam deposited silver mirror, VM is a visible mirror, IF is a 950nm interference filter (Comar 950IL25), F is neutral density filter, QPD is quadrant photodiode, OL1 is a $\times 100$ Nikon (N.A. 1.4) objective lens, OL2 is a $\times 100$ (N.A. 0.7) Mitutoyo long working distance objective lens. L1, L2 and L3 are achromatic lenses with respective focal lengths of 100mm, 250mm and 150mm. L4 and L5 are lenses with focal lengths 50mm and 100mm respectively. S is the sample. Köhler illumination was achieved using an LED emitting at 950nm. The spectrum was measured after OL1 and is shown as an insert.

To determine the trap stiffness values, a quadrant photodiode was used to detect the position of the trapped sphere using the method described in Section 3.3.2.1. The back focal plane of the long working distance objective (Mitutoyo $\times 100$, N.A. 0.7) was imaged onto the QPD. The data from the QPD was used to determine the power spectrum. The trap stiffness values were determined from the corner frequency of the Lorentzian fit to the power spectrum using Equation 3.19. Trap stiffness values were determined for different trapping beam powers. The measurement for the trap stiffness value at each power was repeated at least 15 times and the values were averaged. Figure 5.5 shows some typical power spectrum curves for spheres of diameter 780nm. The power in the trap was 25 ± 1 mW.

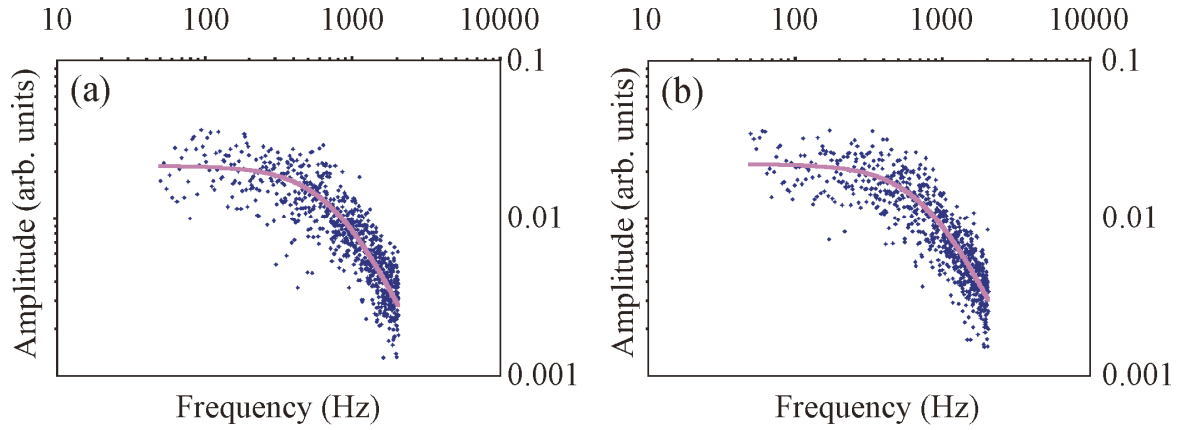


Figure 5.5. Graphs (a) and (b) show the x axis and y axis power spectrum data taken with a 780nm diameter sphere trapped with a laser power of $25 \pm 1\text{mW}$. The dots are the data and the solid line shows the Lorentzian fit to the data (Equation 3.18).

Trap stiffness values were determined in the transverse plane for the 780nm and 970nm diameter spheres at varying laser powers. Axial trap stiffness values were also determined for the 780nm and 970nm spheres as a function of power using the QPD. In addition, transverse trap stiffness values were obtained for the 1.28 μm diameter spheres at a trapping power of 35.6mW. Axial values were not obtained for the 1.28 μm diameter spheres because the power spectrum had a very low corner frequency and, due to the high level of noise at lower frequencies, an accurate trap stiffness value could not be determined. The results are shown in Figure 5.6 and Table 5.2. Table 5.2 compares the transverse trap stiffness values for all three sphere diameters when trapped with the same laser power. The transverse trap stiffness value was highest for the 970nm spheres and lowest for the 1.28 μm spheres. The axial trap stiffness values are shown in Figure 5.7. The 970nm spheres had higher axial values than the 780nm spheres.

The values obtained for κ_x/P_{trap} and κ_y/P_{trap} are similar to values found for a typical optical tweezers setup.^{13,14} However, the axial trap stiffness values obtained are less for a broad bandwidth beam than for a narrowband beam. This is because a broadband beam has chromatic aberration when focused. The use of an apochromatic objective lens minimises chromatic aberration but cannot eliminate the effect.

The expected transverse trap stiffness value can be calculated using Equation 5.1.¹⁵

$$\kappa_r = \frac{8n_m P}{c w_0} \left(\frac{a}{w_0} \right)^3 \left(\frac{m^2 - 1}{m^2 + 2} \right) \left(1 + \left(\frac{z_s}{z_r} \right)^2 \right)^{-2}, \quad (5.1)$$

where a is the radius of the sphere, P is the laser power, n_m is the refractive index of the medium surrounding the spheres, w_0 is the beam waist at the focus, m is the ratio of the refractive index of the sphere to the refractive index of the surrounding medium, z_s is the axial position of the sphere in relation to the beam focus and z_r is the Rayleigh range.

The trap stiffness value is therefore proportional to a^3 .

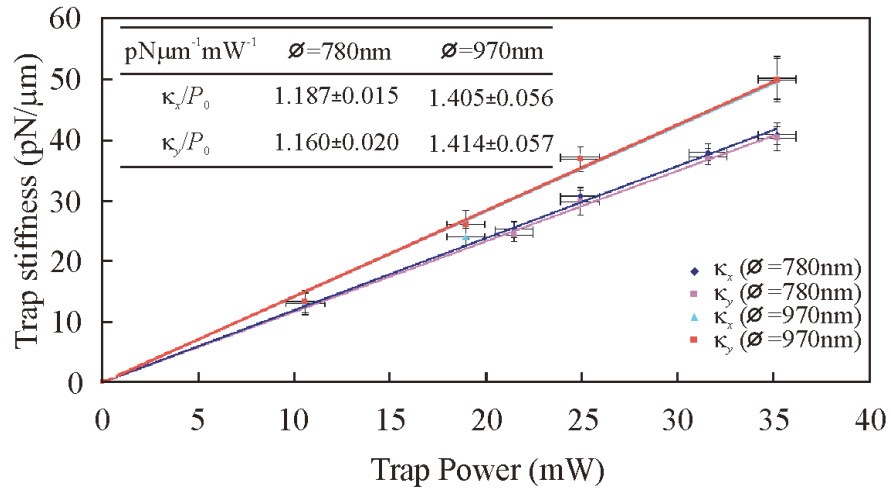


Figure 5.6. The transverse trap stiffness values are displayed as a function of trapping power for 780nm and 970nm diameter silica spheres. The trap stiffness values per unit power are displayed in the insert. The uncertainty in the power was $\pm 1\text{mW}$. The uncertainty in the trap stiffness value was the standard deviation of the 15 values averaged to produce each point on the graph.

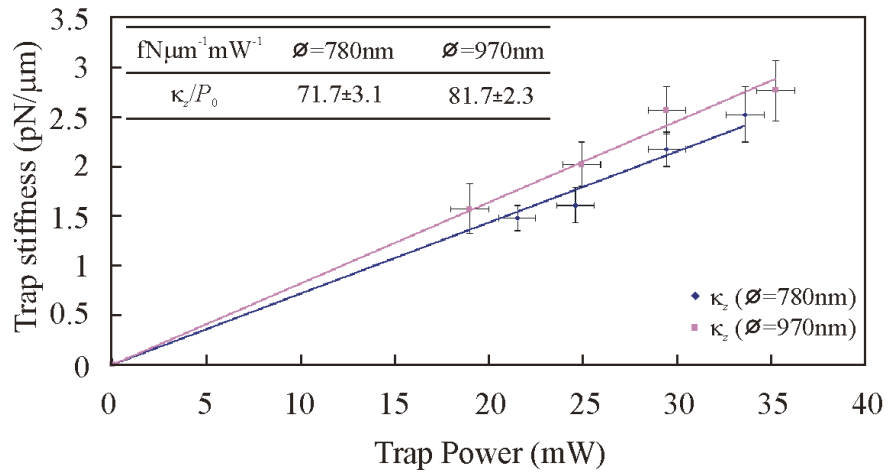


Figure 5.7. This graph compares the axial trap stiffness values as a function of trapping power for 780nm and 970nm diameter silica spheres. A table insert presents the trap stiffness values per mW of power. The uncertainty in the power was $\pm 1\text{mW}$. The uncertainty in the trap stiffness value was the standard deviation of the 15 values averaged to produce each point on the graph.

Table 5.2

Trapping power (mW)	Sphere size (μm)	Stiffness κ_x (pN/ μm)	Stiffness κ_y (pN/ μm)
35.6	1.28	5.27 \pm 0.74	6.03 \pm 0.75
35.3	0.97	50.15 \pm 3.53	49.76 \pm 3.63
35.3	0.78	40.93 \pm 1.80	40.22 \pm 2.00

However, Table 5.2 shows that the transverse trap stiffness values were lower for the 1.28 μm sphere than for the smaller spheres. This is because the scattering force increases as a^6 , so the larger sphere was pushed along the propagation axis by radiation pressure. I suggest that a possible scenario is that the 1.28 μm spheres were tweezed at a z position further away from the focus than where the smaller spheres were tweezed. This may then have resulted in reduced lateral trap stiffness values for the 1.28 μm spheres compared to the smaller spheres. The smaller spheres experienced a smaller scattering force and may have been trapped closer to the beam focus. This effect did not occur in the data presented in Table 5.1 because the spheres were pushed up against the top coverslide and only optical trapping (not tweezing) was achieved, so the z position of the trapped spheres with respect to the beam focus did not vary greatly.

The Q value can be related to the transverse trap stiffness value, κ_r , by

$$\kappa_r = \frac{Qn_s P}{r_{\max} c}, \quad (5.2)$$

where n_s is the refractive index of the sphere, P is the laser power, r_{\max} is the maximum deviation of the sphere from the trap centre and c is the speed of light.

5.2.4 Optical trapping of polymer spheres

Next, I investigated the trap stiffness values of optically trapped polymer spheres ($n_s = 1.59$). I was able to optically trap 1 μm diameter polymer spheres. The top coverslip of the sample chamber confined the spheres in the axial direction. A spatial light modulator was incorporated into the setup for a later experiment where broadband multiple traps were generated. This experiment is described later in this chapter. The experimental setup is shown in Figure 5.8.

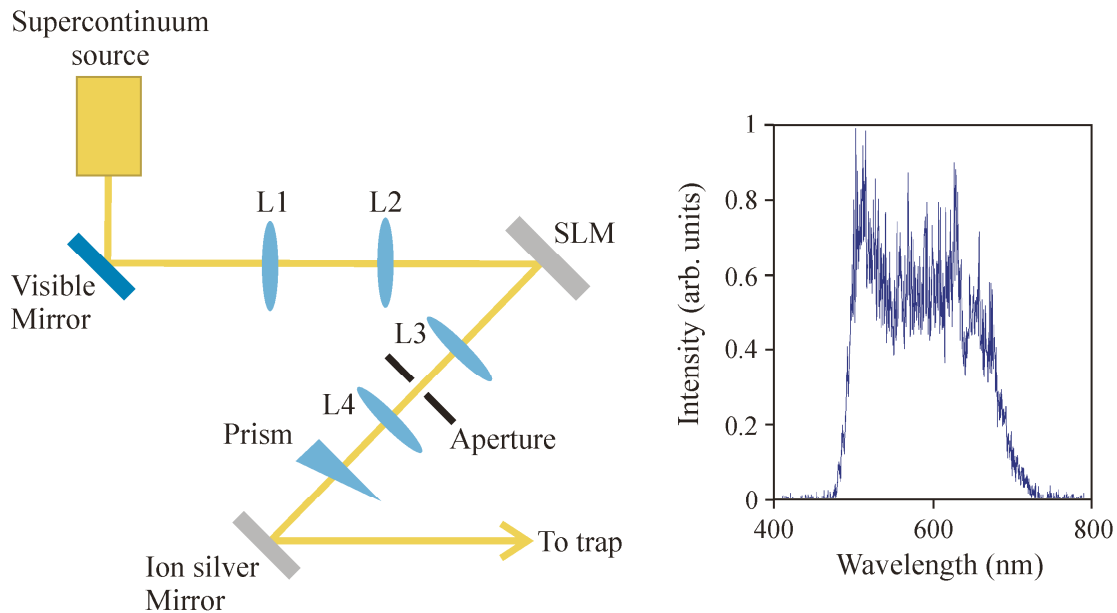


Figure 5.8. The experimental setup used to measure the trap stiffness values of polymer microspheres is shown. A spatial light modulator (SLM) was incorporated into the setup for the multiple trapping experiment, which is presented in Section 5.3. Lenses L1, L2, L3 and L4 are achromatic doublet lenses with focal lengths 50mm, 250mm, 200mm and 160mm respectively. An aperture was used to select the first diffraction order from the hologram. The hologram was imaged onto a 10° deviation angle prism (Comar 10JW25) to compensate dispersion. Refer to Section 4.7 and Figure 4.14 for information about the use of a spatial light modulator to generate broad bandwidth optical beams. A $\times 100$ Nikon (N.A 1.4) objective lens was used to focus the supercontinuum beam into the sample. The objective lens that was used to deliver the illumination light to the sample was a $\times 100$ (N.A 0.7) Mitutoyo long working distance objective lens. The spectrum obtained in the trapping plane is shown on the right. The specifications for the SLM (Holoeye 2500) are given in Table 4.1.

Filling the back aperture of the focusing objective lens ($\times 100$, N.A 1.4) with the supercontinuum beam produced a tightly focused broadband spot with a spot size of 640nm (FWHM). However, there was some difficulty trapping the polymer microspheres with this tightly focused beam. Therefore, I tried objective lenses with lower N.A. values to produce a larger focused spot. The power in the trapping plane and the size of spheres in the sample were also varied. Optical trapping of $1\mu\text{m}$ spheres was achieved using an objective lens ($\times 100$, N.A. 1.4) with an under-filled back aperture to produce a larger focused spot in the sample. The power in the sample plane was kept low at 11mW. At higher powers trapping could not be achieved. The scattering force is larger for polymer spheres than for silica spheres and this is why it was more difficult to trap polymer spheres. Since the trapping was in two dimensions and the top coverslip was used to confine the sphere in the third dimension, the exact trapping position of the sphere with

respect to the beam focus was not known. However, the beam focus was measured to have a spot size of $1.2\mu\text{m}$ (FWHM).

The optical potential analysis method, described in Section 3.3.2.2, was used to find the transverse trap stiffness values for a $1\mu\text{m}$ diameter polymer sphere. A high frame rate camera (Basler pl640-210gm) was used to record videos of the trapped sphere. The position probability distribution was then plotted and the trap stiffness values were determined. The derived trap stiffness values are shown in Figure 5.9 along with the position probability graphs for the x and y axes. The optical trap had good symmetry with $\kappa_x = 1.1\text{pN}/\mu\text{m}$ and $\kappa_y = 1.3\text{pN}/\mu\text{m}$ for a trapping power of 11mW .

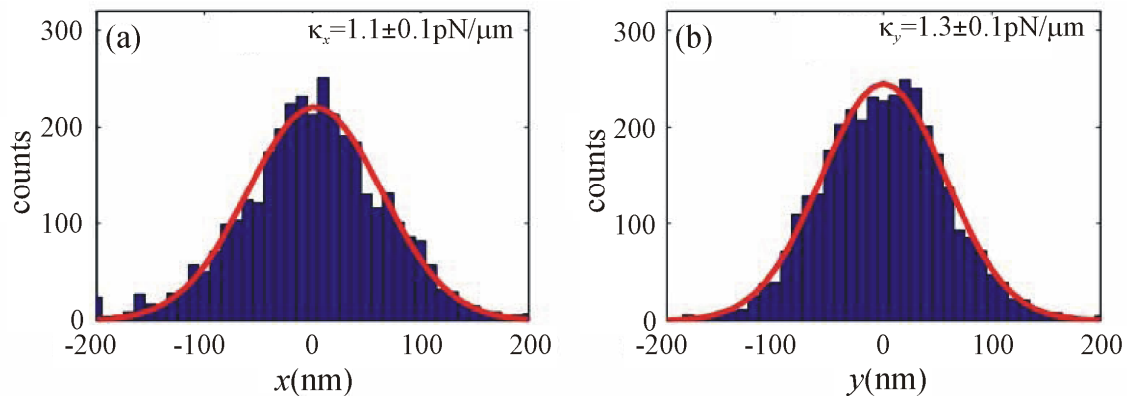


Figure 5.9. Position probability histograms for the trapped $1\mu\text{m}$ polymer sphere are shown for the x and y axes. The power in the trapping plane was 11mW .

5.3 Multiple beam optical manipulation

5.3.1 Using a spatial light modulator for optical manipulation with a supercontinuum source

Multiple beam optical manipulation is now easily achievable using a narrowband laser and has many applications. I investigated if multiple optical manipulation was possible using a broad bandwidth source. Diffractive optical elements have made it possible to generate a wide variety of beam shapes such as Bessel beams, optical vortices and arrays of optical trap sites.¹⁶ A hologram displayed on a spatial light modulator imposes a phase on an incident beam to produce the multiple trap sites. This method is convenient when using a narrowband light source but it is more challenging when using a broad bandwidth

source. In Section 4.6, we found out that it is often necessary to add a grating to a hologram for the purpose of separating the different order beams that are generated. The SLM hologram is not able to convert 100% of the incident light into the desired mode. Some of the light is converted into higher order modes. Also, light that is directly reflected from the surface of the SLM display does not have a phase modulation applied to it. All of these beams are overlapped after encountering the hologram unless a diffraction grating is added. Adding a grating to the hologram mask spatially separates the preferred modulated beam from the un-modulated zero order beam and the higher order beams. The preferred beam can be selected and the other beams can be blocked using a lens and an aperture as illustrated in Figure 4.13(c). However, the wavelength components of a supercontinuum beam diffract at different angles. This causes spatial dispersion of the beam. This issue can be overcome by placing a prism in the image plane of the hologram as demonstrated by Leach *et al.*^{17,18} The prism must have the opposite dispersion to that of the hologram grating. Figure 5.8 shows the setup used to compensate dispersion using a prism and Figure 4.14 illustrates the general process in more detail. The spatial dispersion was compensated, and the wavelength components were overlapped to produce a single ‘white light’ beam. Using a computer program, it is possible to alter the grating spacing of the hologram. This allows fine tuning of the dispersion compensation scheme.

5.3.2 The twin trap

The experimental setup used to produce the twin trap was the same as that in Figure 5.8 except that L3 and L4 had focal lengths of 630mm and 500mm respectively. This was in order to bring the conjugate plane of the SLM to the back aperture of the objective lens. The prism was placed directly before the back aperture of the objective lens to compensate the dispersion. The hologram used to produce the twin trap was a phase ramp grating of modulo 2π with a period of approximately $87\mu\text{m}$, and this was multiplied by a square wave grating with vertical rulings of amplitude π and a period of approximately $330\mu\text{m}$. The lines of the square wave grating were oriented at approximately 45° from the vertical direction. The lines of the phase ramp grating were oriented at approximately -35° from the vertical direction.

The hologram was displayed on the SLM, and a picture of the dispersion compensated twin trap produced is shown in Figure 5.10.

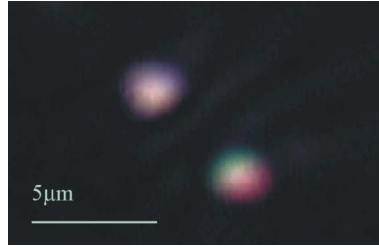


Figure 5.10. An image of the dispersion compensated twin trap is shown. The ‘upper’ and ‘lower’ trap sites are referred to in this section based on their position in this image.

To show that the wavelengths are well overlapped, cross-sections of the beams were taken and separated into their red, green and blue components. Figure 5.11 shows that these components are well overlapped. The intensity of each component has been normalized to show the overlap more clearly. Note that the lower trap is not as well compensated as the upper trap, and that the upper trap has approximately 1.1 times more power than the lower trap. This is due to the uneven diffraction efficiency of the hologram. The total power of both traps was 24mW. The beam waist for each trap is approximately $1.2\mu\text{m}$ (FWHM).

Images of some traps that were not well dispersion compensated are shown in Figure 5.12. Since the multiple trapping beams diffract from the SLM at different angles, each optical trap has different dispersion properties. Therefore, it is not a trivial task to compensate dispersion for more than two trap sites.

We can determine the dispersion induced by the prism by calculating the deflection angle of the beam as a function of wavelength using the equation $\theta_\lambda = (n_\lambda - 1)w$, where w is the wedge angle of the prism (18.97° as stated by the manufacturer), n_λ is the refractive index for wavelength λ and θ_λ is the deflection angle for wavelength λ . The dispersion caused by the grating can be calculated using the grating equation $\Lambda \sin \theta_m = m\lambda$, where Λ is the grating spacing, θ_m is the deflection angle for the m^{th} diffraction order and λ is the wavelength.

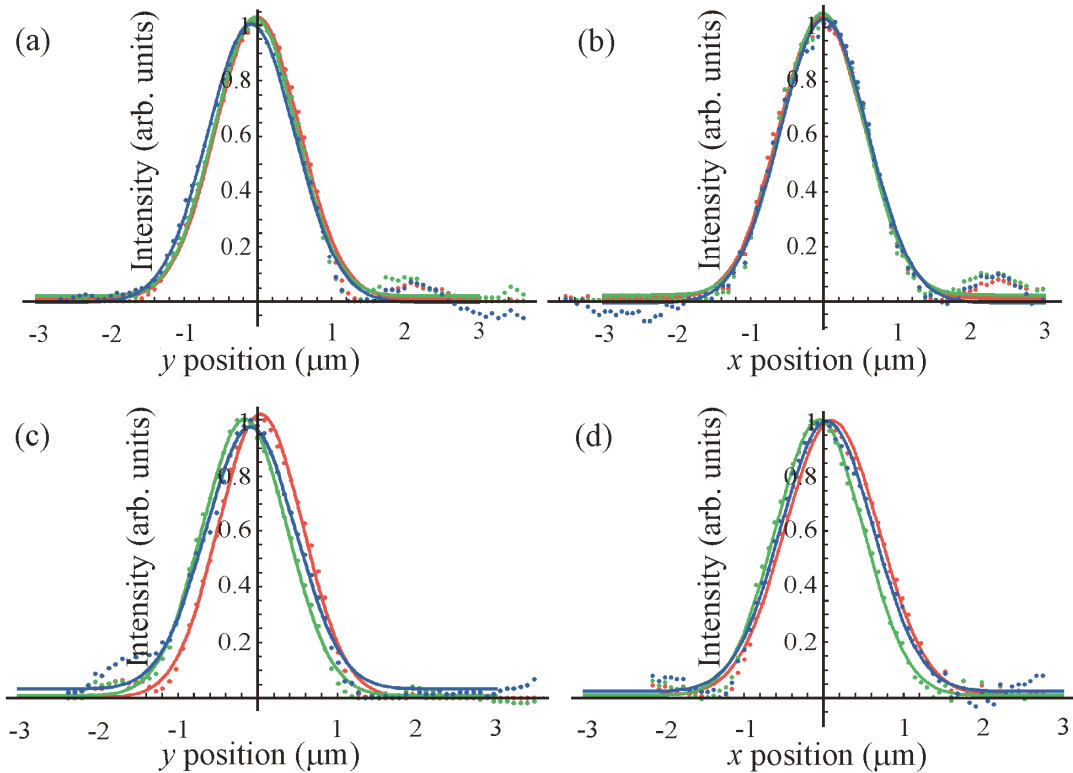


Figure 5.11. Graphs (a) and (b) show the RGB components of cross-sections taken for the upper trap seen in Figure 5.10. Graphs (c) and (d) show the RGB components of the cross-sections for the lower trap. Graphs (a) and (c) show the vertical cross-sections and graphs (b) and (d) show the horizontal cross-sections. The intensities of the RGB components were normalised so that the comparison can be seen clearly.

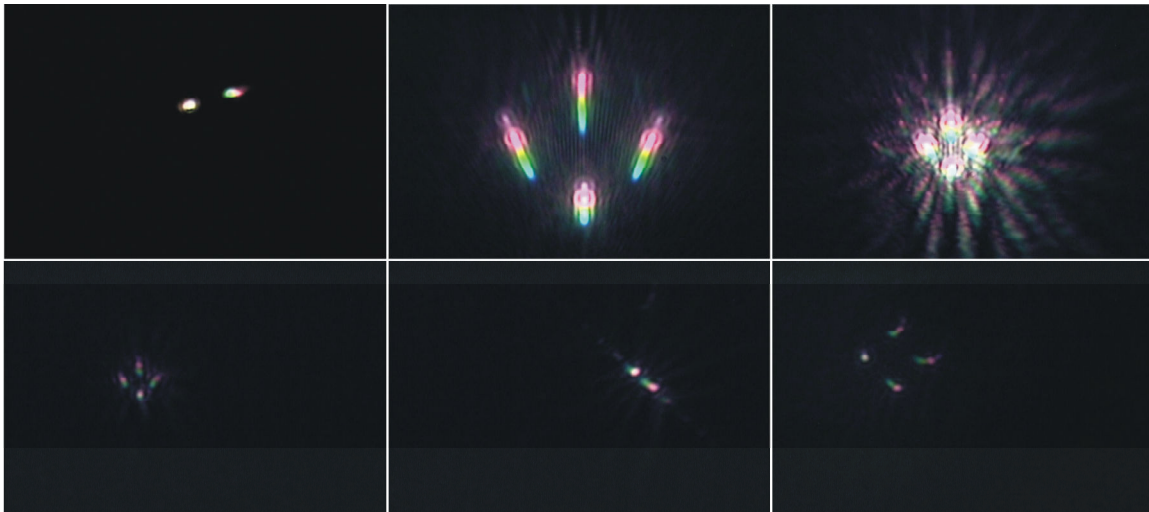


Figure 5.12. Images of multiple traps that were produced using a hologram with a grating spacing that was not optimal for dispersion compensation using the prism arrangement are shown.

The grating was imaged onto the prism. The grating spacing was then adjusted using a program until the best dispersion compensation was achieved. For this reason, the exact

grating spacing is not known. However, by looking at the hologram and counting the number of grating lines within a certain distance, we can determine that the grating spacing of the phase ramp grating was approximately $87\mu\text{m}$, as stated earlier, with the angle of the grating lines at approximately -35° from the vertical. The prism was oriented approximately perpendicular to the lines of the grating to compensate the dispersion. For the first diffracted order, the deflection angle can be calculated for wavelengths 480nm, 546nm and 706nm. Table 5.3 lists the refractive index of the prism as a function of wavelength, the deflection angle of the beam after propagating through the prism and the deflection angle of the beam after the grating for wavelengths 480nm, 546nm and 706nm.

Table 5.3

Wavelength (nm)	n_λ	Prism θ_λ	Grating θ_1
480	1.52283	9.918	0.315
546	1.51872	9.840	0.358
706	1.51289	9.730	0.463

The difference in deflection angle between 480nm and 706nm for the prism is 0.19° and for the grating is 0.15° . These calculations show that the prism used in our experiment with wedge angle 18.97° (deflection angle $\sim 10^\circ$) induces a larger dispersion angle than that produced at the grating. There is a 0.04° discrepancy between the dispersion angle produced by the experimentally optimized grating spacing and the theoretically predicted dispersion angle. In the experiment, these parameters were able to compensate the dispersion exactly for the upper trap shown in Figure 5.10. The imaging system may have introduced an angular magnification. This may have increased the angular dispersion from the grating which could account for the 0.04° discrepancy between the calculated dispersion angle and the observed dispersion angle. This could be investigated by measuring the angular dispersion immediately after the grating and before the prism. The transverse spatial separation between the different wavelength beams could be determined by taking an image of the beam after the grating and before the prism. Knowing the distance from the grating (or from the second imaging lens), trigonometry could then be used to determine the actual dispersion angles.

The square wave grating had a spacing of approximately $330\mu\text{m}$. The deflection angle of light at the grating for wavelength 706nm is 0.123° and for wavelength 480nm is 0.083° . The dispersion angle at the grating is then approximately 0.04° . Assuming that the angular dispersion induced by the lenses is equal to 0.04° as suggested above, the lower trap incident on the prism has a dispersion angle of 0.08° . Since the prism induces an opposite dispersion of 0.19° , the dispersion angle of the lower spot upon entering the objective lens is 0.11° .

We can now use the dispersion observed in Figure 5.11(c) and Figure 5.11(d) to calculate back and determine the dispersion angle of the lower beam in the sample plane i.e. after propagating through the objective lens. We can use Figure 5.11(c) and Figure 5.11(d) to calculate the angle between the ‘red’ and ‘green’ components in the sample (since these are the two wavelength components that are spatially separated by the largest distance). The working distance of the objective lens is $130\mu\text{m}$ and the distance between the ‘red’ and ‘green’ components is $0.25\mu\text{m}$. Using trigonometry we can determine that the angle between the ‘red’ and ‘green’ components of the beam emerging from the objective lens is 0.11° . This is in good agreement with the predicted dispersion angle of the lower trap calculated above for the square wave grating with grating spacing $330\mu\text{m}$.

The hologram used to generate the twin trap was produced using an existing Labview program and is different from the ideal hologram for this task. The phase of a grating hologram is given by

$$\psi(x, y) = \text{mod}\left(\frac{2\pi}{\Lambda_x}x + \frac{2\pi}{\Lambda_y}y, 2\pi\right), \quad (5.3)$$

where $\text{mod}(a, b)$ gives the remainder of a/b , Λ_x is the grating spacing in the x axis and Λ_y is the grating spacing in the y axis. The complex function applied to the incident beam is then $\exp(i\psi(x, y))$. Multiple optical traps can be produced by summing up the complex functions and taking the argument of the resulting complex function. The ideal hologram for multiple traps can then be described by¹⁹

$$\psi(x, y) = \arg\left(\sum_j \exp(i\psi_j(x, y))\right). \quad (5.4)$$

This generates a hologram that is the superposition of two gratings.

Now we look at the difference between the diffraction patterns of the two holograms. A phase ramp grating deflects the incident beam as discussed in Section 4.6. A square wave grating produces multiple diffraction orders, but since the amplitude of the phase modulation is π , there is no zero order and the first diffraction orders are the most intense. Therefore, the diffraction pattern from the hologram used in the experiment is the convolution of the diffraction pattern of the two gratings, so multiple orders from the square wave grating are deflected by the phase ramp grating. The diffraction pattern arising from the hologram of Equation 5.4 is two sets of diffracted orders produced by the two superimposed gratings. Therefore, the use of the hologram from Equation 5.4 is preferable.

I then progressed on to see if it was possible to optically trap polymer microspheres in this arrangement and to determine the trap stiffness values. A solution of $2\mu\text{m}$ polymer spheres in water (Duke Scientific 4202A, refractive index $n_s = 1.59$) was used, and optical confinement of the spheres in two dimensions was achieved. Again, the top coverslip of the sample chamber confined the spheres in the axial direction. Images of the trapped spheres are shown in Figure 5.13. The trap stiffness values were determined using the optical potential analysis method, which was described in Section 3.3.2.2. The resultant position probability histograms are presented in Figure 5.14.

The upper trap had a higher trap stiffness value because it is better compensated for dispersion and has more power than the lower trap. The lower trap has non-symmetric values because the dispersion compensation is better in the x axis than in the y axis.



Figure 5.13. The three images show the optically trapped spheres as the sample is translated, first upwards (middle image) and then to the right (right image). The two optically trapped spheres are indicated by the white circles. A stationary sphere is indicated by the black circles for reference. The sample stage was translated and the two optically trapped spheres remained confined in the trap.

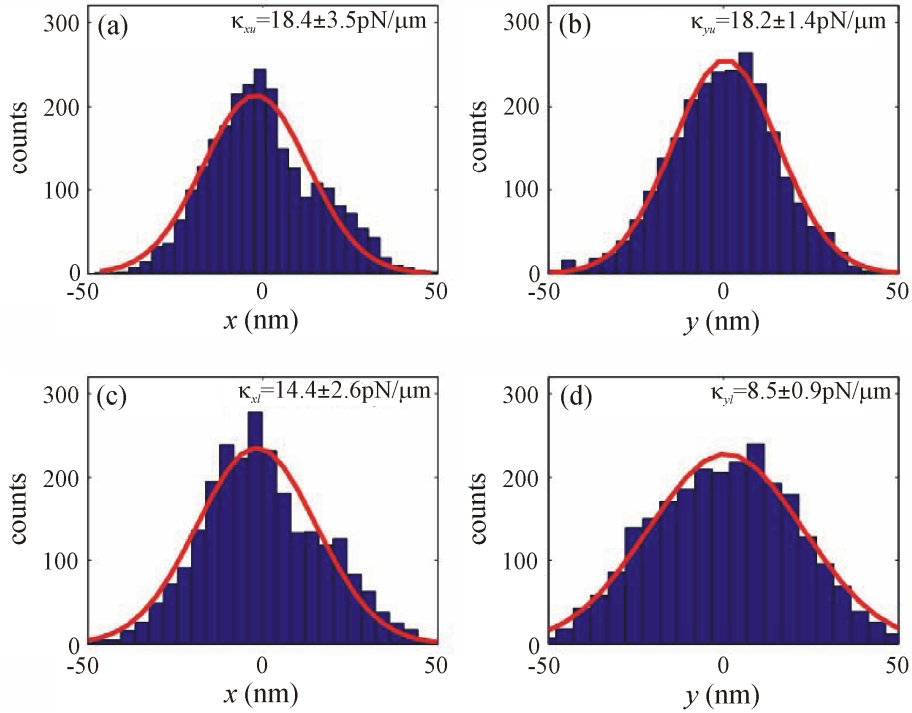


Figure 5.14. The position probability histograms are shown for both traps. Histograms (a) and (b) were obtained from the upper trap site and histograms (c) and (d) were obtained from the lower trap site. The graphs on the left are for the horizontal direction and the graphs on the right are for the vertical direction. The uncertainty in the fit was determined using a Matlab nonlinear regression function.

5.4 Multiple optical manipulation using a parabolic micromirror array

5.4.1 Introduction

Parabolic mirrors have properties that make them ideal for use with broad bandwidth sources. A collimated beam of broadband light incident on a parabolic mirror has all of its constituent wavelengths focused to a single point. This is ideal for optical manipulation. The focal length of a parabolic mirror is only dependent on the dimensions of the mirror. Therefore, no dispersion compensation techniques are required. When a laser is incident on an array of parabolic micromirrors, optical trap sites are produced at the foci of the mirrors. Therefore, the use of the micromirror array offers an alternative method to diffractive optics for generating multiple broad bandwidth optical traps.

The parabolic micromirror array also offers the possibility to develop lab-on-a-chip devices. The use of a spatial light modulator¹⁶ to generate multiple optical trap sites is very effective for many applications but is not conducive to the development of micrometer sized devices. To make multiple individual 3D trap sites, micrometer sized optical components with a very high numerical aperture are required. One of the few successful cases where a high N.A. micrometer sized component was manufactured was a tapered fibre.²⁰ The parabolic micromirror array offers a solution. Laser light incident on the array is focused by the mirrors to produce optical trap sites. The medium surrounding the micromirrors increases the numerical aperture of the system to appropriately high values to facilitate tight focusing for the three dimensional optical confinement of objects. In traditional multiple trapping setups, the field of view is limited by the high N.A. of the objective lens. This limitation is removed when using a micromirror array.

When the micromirror array was first introduced, it was useful for the detection of fluorescence from multiple trapped objects.²¹ A mixture of fluorescent spheres was allowed to flow through the device. Two excitation lasers were coincident on the micromirror array along with the trapping laser. A CCD camera was used to view the fluorescence of the trapped spheres. The same research group showed that the axial trap stiffness values, obtained for narrowband traps created using a micromirror array, can be higher than those achieved when a high N.A. objective lens is used to generate an optical trap site.²²

5.4.2 The parabolic micromirror array

The parabolic micromirror array used in the experiments presented in this chapter was manufactured at École Polytechnique Fédérale de Lausanne in Switzerland by Fabrice Merenda *et al.*²¹ There are 400 parabolic micromirrors arranged in a hexagonal array. Each mirror is a 60nm layer of gold embedded inside UV curing resist ($n_{solid} = 1.56$). The distance between the centres of two adjacent mirrors is 250 μ m. Each mirror has a diameter of 240 μ m and a radius of curvature of 350 μ m. There is an 80 μ m thick coverslip attached on top of the UV curing resist. Glue is applied around the micromirror array to

attach a microscope slide (1mm thick) on top and seal the microfluidic channel. The microscope slide has two holes into which microfluidic tubes can be inserted. A syringe pump is used to flow a sample through the microfluidic tubes and into a channel above the micromirror array. Figure 5.15 illustrates the micromirror array.

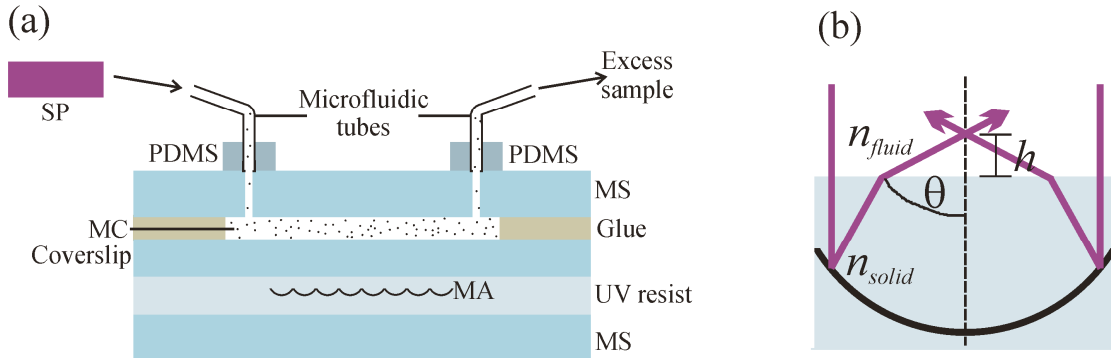


Figure 5.15. (a) Micromirror array illustration. Both microscope slides are 1mm thick and the coverslip is 80 μ m thick. MS is microscope slide, MA is micromirror array, MC is microfluidic channel, SP is syringe pump. (b) is an illustration of high numerical aperture focussing.

The numerical aperture of the micromirrors, taking into account that they are surrounded by UV curing resist, is 0.96. This value can compete with some of the best objective lenses and is high enough to tightly focus a laser beam for the three dimensional optical confinement of objects.

5.4.3 Broadband multiple optical manipulation using a parabolic micromirror array

The micromirror array reflects infrared wavelengths extremely well but transmits enough visible light to allow illumination light to be transmitted. We used a visible reflecting mirror (Comar 25MX02) to filter the visible wavelengths from the supercontinuum beam. The infrared beam (~700nm – 1700nm) was then directed onto the micromirror array from above producing trap sites at the focus of each parabolic micromirror. The sample was illuminated from above the array using an LED emitting at a wavelength of 450nm in a Köhler arrangement. The illumination light was collected using an objective lens (Mitutoyo $\times 100$, N.A. 0.7) placed below the micromirror array and directed onto a CCD camera using a mirror. The CCD camera was used to view the sample. An interference filter that transmits light at 450nm (bandwidth 40nm) was placed before the CCD camera

to block the supercontinuum beam. The sample consisted of polymer microspheres immersed in water. A syringe pump was used to flow the microspheres through the microfluidic chamber located above the micromirror array.

The total beam power incident on the micromirror array was 1.3W and the spot size was approximately 3mm. Separate samples of polymer spheres with diameters of 1 μ m, 2 μ m, 5 μ m and 10 μ m were injected into the micromirror device using the syringe pump. I was able to optically confine the spheres in three dimensions at the foci of the micromirrors. Figure 5.16 is a picture of 10 μ m diameter polymer spheres trapped using the micromirror array.

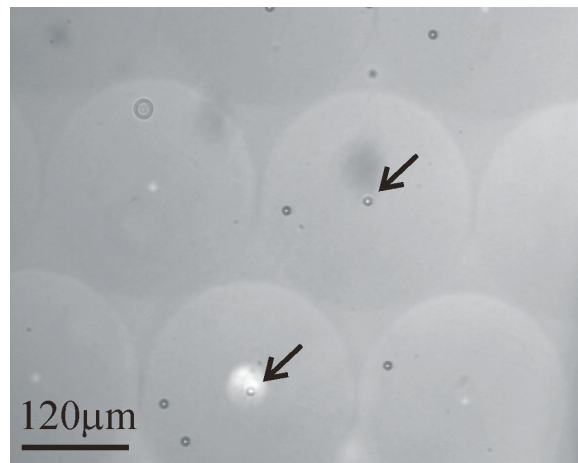


Figure 5.16. A picture of the micromirror array is shown with two microspheres optically confined by the traps produced at the foci of the micromirrors. The trapped microspheres, indicated by the black arrows, each have a diameter of 10 μ m.

Next, I investigated possible methods to determine the trap stiffness values using a quadrant photodiode. Some challenges had to be overcome to obtain a suitable signal for analysis by a QPD. The transmitted laser light from the optical traps could not be used as the QPD signal because the micromirrors are highly reflective at infrared wavelengths, so the transmitted light through the mirrors is extremely weak. Additionally, the high divergence of the micromirrors makes it difficult to collect all the reflected light from the mirrors for analysis. One proposed solution to this issue was to introduce a green helium-neon laser (Thorlabs, $\lambda = 543$ nm, 0.5mW) from below the micromirror array to act as a probe beam. The setup had to be carefully thought through to ensure that the probe beam, supercontinuum beam and illumination light were all transmitted to where they were

required and blocked from where they were not required. The experimental setup is shown in Figure 5.17.

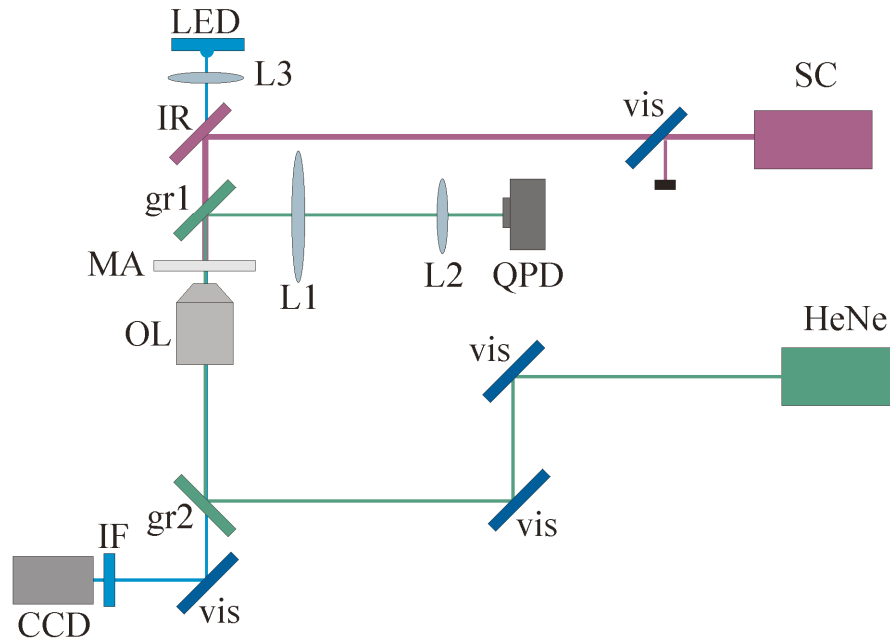


Figure 5.17. The experimental setup is shown. Three different types of mirrors were used: infrared reflecting, IR, (Comar 25MX05), visible reflecting, vis, (Comar 25MX02) and green reflecting, gr, (Thorlabs DMLP605). SC is supercontinuum, QPD is quadrant photodiode, HeNe is the green ($\lambda = 543\text{nm}$) helium-neon laser, OL is objective lens (Mitutoyo X50 N.A.=0.55) and MA is the micromirror array. The LED emitted light at 450nm. Lenses L1, L2 and L3 have focal lengths of 85mm, 50mm and 20mm respectively. Lens L1 was a large diameter lens (2 inches) in order to collect all the highly divergent probe light.

The helium-neon laser was focused into the sample from below using an objective lens (Mitutoyo $\times 50$, N.A. 0.55). The transmitted and scattered probe light was collected and imaged onto the QPD using lenses L1 and L2. It was necessary to use narrowband green reflecting mirrors (Thorlabs DMLP605) to direct the probe beam. This was to allow the transmission of both the supercontinuum beam and the illuminating light whilst the green mirrors reflected only the probe beam. An infrared mirror (Comar 25MX05) was used to direct the supercontinuum beam onto the micromirror array. Lens L1 had to be chosen carefully so that the N.A. was approximately matched to that of the objective lens. However, the focal length of the lens had to be large enough to allow space for the micromirror array and green mirror to fit between the objective lens, OL, and lens L1. Additionally, the green reflecting mirror had to be large enough to collect the diverging probe beam light. The numerical aperture of a lens can be calculated using Equation 5.5.

$$N.A._L = \frac{n_{lens} D_{lens}}{2f_{lens}}, \quad (5.5)$$

where n_{lens} is the refractive index of the lens material, D_{lens} is the diameter of the lens and f_{lens} is the focal length. The N.A. of lens L1 ($f_{lens} = 85\text{mm}$, $D_{lens} = 75\text{mm}$, $n_{lens} = 1.52$) was calculated to be 0.67. This is close to the N.A. of the original objective lens used (Mitutoyo $\times 100$, N.A. 0.7). However, the probe beam diverged too rapidly from this objective lens and all of the light could not be collected by the green mirror, gr1. I therefore switched to an objective lens with N.A. = 0.55.

At this time the trapped spheres were only confined very weakly in the optical traps. The UV curing resist above the micromirror array had blistered. Figure 5.18 is an image of the blistering of the UV curing resist layer. Although no trap stiffness values were obtained, the optical confinement of multiple polymer microspheres in three dimensions was achieved using the supercontinuum beam and the micromirror array.

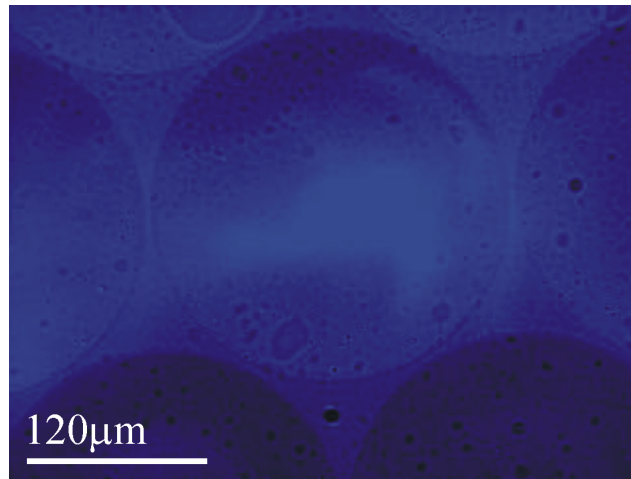


Figure 5.18. This picture shows the blistering of the UV curing resist layer above the micromirror array.

5.5 Discussion

In this chapter, a method to allow the simultaneous optical manipulation and observation of microspheres using a supercontinuum source has been presented. Polymer spheres of diameter $1\mu\text{m}$, $2\mu\text{m}$, $3\mu\text{m}$, $5\mu\text{m}$ and $10\mu\text{m}$ were confined in a broadband optical trap and Q values were measured. Although Q values are useful for obtaining information about the momentum transfer from a laser to a trapped object, Q values do not give a measure

of the forces involved in the optical trap. For biological applications, such as single molecule studies, it is necessary to obtain information about the forces in optical tweezers. The force can then be compared to other forces measured in different situations, whereas the Q value cannot because it is a dimensionless number. Trap stiffness values are a measure of the forces in an optical tweezers.

I obtained trap stiffness values for both polymer and silica spheres confined in a broadband optical trap. I was able to optically tweeze silica spheres (970nm, 780nm and 1.28 μ m) immersed in water. However, only optical trapping (not tweezing) was achieved for polymer spheres (1 μ m) immersed in water. It is known from Equation 3.2 that, due to the higher refractive index of polymer compared to silica, the scattering forces acting on polymer spheres are larger than those acting on silica spheres. Therefore, polymer spheres experience more radiation pressure in the direction of beam propagation than silica spheres. It can then be surmised that the reason the polymer spheres were not optically confined in three dimensions is because the radiation pressure was greater than the axial gradient force.

Additionally, a computer generated hologram displayed on a spatial light modulator has been used to generate two broadband optical trap sites. Dispersion in the generated beams arising from the hologram diffraction grating was compensated using a prism placed in the image plane of the hologram. In the dispersion compensated twin traps, I was able to optically trap two polymer microspheres each with a diameter of 2 μ m. Producing more than two broadband optical traps in this way is challenging because dispersion compensation becomes more complicated as the number of trap sites increases. It was observed that the dispersion of each trap site produced is different, so a single prism cannot be used to compensate the dispersion for all of the traps generated. This is a limitation of the prism dispersion compensation method for this application. However, other methods may be more successful. For example, it may be possible to use a second spatial light modulator to counter the dispersion for multiple broadband optical traps using a technique similar to that used by Mariyenko *et al.*²³

The transverse trap stiffness value per mW obtained for the single beam Gaussian trap was around 10 times less than the values obtained for the twin trap. A difference between the values in the two cases is expected because the beam parameters are not exactly the same and the sphere size was different. However, this is a larger difference than would be expected if these were the only factors considered. One possible explanation is that the sphere in the single beam trap was not at the focus of the beam, which would result in a low trap stiffness value. Additionally, it is possible that aberrations in the beam arising from a misalignment may have reduced the trap stiffness value in the single beam trap.

The micromirror array has shown great promise for generating broadband multiple optical trap sites. The micromirror array is not as versatile as an SLM for generating multiple optical trap sites. However, it offers a simpler way to generate multiple trap sites than using an SLM. Additionally, the micromirror array can easily be integrated into a lab-on-a-chip device. With the use of a supercontinuum source as the trapping beam, a lab-on-a-chip device that could spectrally analyse biological items might be developed.

Using the micromirror array and the supercontinuum source, I successfully achieved the three dimensional optical confinement of polymer microspheres with diameters ranging from $1\mu\text{m}$ - $10\mu\text{m}$. It is clear that the spheres were optically confined in three dimensions because the trapped spheres were far away from the top of the sample chamber. An experimental setup was also developed that could be used to characterise the forces of the optical traps. This setup overcomes the challenges arising due to the high divergence of the micromirrors. It is thought that the cause of the blistering of the UV curing resist was most likely due to heating over time from the high power infrared radiation incident on the array. The group at École Polytechnique Fédérale de Lausanne have observed a similar effect.

The work presented in Sections 5.2.4 up to and including Section 5.3.2 was published in Optics Express.²⁴

Acknowledgements

Pascal Fischer worked with the Author to solve the illumination problem. Peter Reece helped the Author set up the QPD and his Labview program was used in conjunction with the QPD for the work presented in Section 5.2.3. Tomáš Čížmár used his existing particle tracking program to analyse the Brownian motion videos that were obtained by the Author in Sections 5.2.4 and 5.3.2. An existing Labview program was used for the twin trap and was written by Daniel Burnham and David McGloin. For Section 5.4, the micromirrors were fabricated by Fabrice Merenda. The Author setup all the experiments and obtained all the results.

References

1. Fischer, P. et al. Enhanced optical guiding of colloidal particles using a supercontinuum light source. *Optics Express* **14**, 5792-5802 (2006).
2. Li, P., Shi, K. B. & Liu, Z. W. Manipulation and spectroscopy of a single particle by use of white-light optical tweezers. *Optics Letters* **30**, 156-158 (2005).
3. Lindfors, K., Kalkbrenner, T., Stoller, P. & Sandoghdar, V. Detection and spectroscopy of gold nanoparticles using supercontinuum white light confocal microscopy. *Physical Review Letters* **93** (2004).
4. Guillon, M., Dholakia, K. & McGloin, D. Optical trapping and spectral analysis of aerosols with a supercontinuum laser source. *Optics Express* **16**, 7655-7664 (2008).
5. Gherardi, D. M., Carruthers, A. E., Cizmar, T., Wright, E. M. & Dholakia, K. A dual beam photonic crystal fiber trap for microscopic particles. *Applied Physics Letters* **93** (2008).
6. Bustamante, C., Bryant, Z. & Smith, S. B. Ten years of tension: single-molecule DNA mechanics. *Nature* **421**, 423-427 (2003).
7. Bishop, A. I., Nieminen, T. A., Heckenberg, N. R. & Rubinsztein-Dunlop, H. Optical microrheology using rotating laser-trapped particles. *Physical Review Letters* **92**, 198104 (2004).
8. Yao, A., Tassieri, M., Padgett, M. & Cooper, J. Microrheology with optical tweezers. *Lab Chip* **9**, 2568-75 (2009).
9. Enger, J., Goksör, M., Ramser, K., Hagberg, P. & Hanstorp, D. Optical tweezers applied to a microfluidic system. *Lab Chip* **4**, 196-200 (2004).
10. Eriksson, E. et al. A microfluidic system in combination with optical tweezers for analyzing rapid and reversible cytological alterations in single cells upon environmental changes. *Lab Chip* **7**, 71-76 (2007).
11. Meiners, J.-C. & Quake, S. R. Direct measurement of hydrodynamic cross correlations between two particles in an external potential. *Physical Review Letters* **82**, 2211 LP - 2214 (1999).

12. Lacey, A. J. *Light microscopy in biology* (IRL press, 1989).
13. Ghislain, L. P., Switz, N. A. & Webb, W. W. Measurement of small forces using an optical trap. *Review of Scientific Instruments* **65**, 2762-2768 (1994).
14. Rohrbach, A. Stiffness of optical traps: quantitative agreement between experiment and electromagnetic theory. *Phys Rev Lett* **95**, 168102 (2005).
15. Neuman, K. C. & Block, S. M. Optical trapping. *Review of Scientific Instruments* **75**, 2787-2809 (2004).
16. Curtis, J. E., Koss, B. A. & Grier, D. G. Dynamic holographic optical tweezers. *Optics Communications* **207**, 169-175 (2002).
17. Leach, J. et al. Generation of achromatic Bessel beams using a compensated spatial light modulator. *Optics Express* **14**, 5581-5587 (2006).
18. Leach, J. & Padgett, M. J. Observation of chromatic effects near a white-light vortex. *New Journal of Physics* **5** (2003).
19. Liesener, J., Reicherter, M., Haist, T. & Tiziani, H. J. Multi-functional optical tweezers using computer-generated holograms. *Optics Communications* **185**, 77-82 (2000).
20. Liu, Z., Guo, C., Yang, J. & Yuan, L. Tapered fiber optical tweezers for microscopic particle trapping: fabrication and application. *Opt. Express* **14**, 12510-12516 (2006).
21. Merenda, F., Rohner, J., Fournier, J. M. & Salathe, R. P. Miniaturized high-NA focusing-mirror multiple optical tweezers. *Optics Express* **15**, 6075-6086 (2007).
22. Merenda, F., Grossenbacher, M., Jeney, S., Forro, L. & Salathe, R. P. Three-dimensional force measurements in optical tweezers formed with high-NA micromirrors. *Optics Letters* **34**, 1063-1065 (2009).
23. Mariyenko, I. G., Strohaber, J. & Uiterwaal, C. Creation of optical vortices in femtosecond pulses. *Opt. Express* **13**, 7599-7608 (2005).
24. Morris, J. E. et al. Optical micromanipulation using supercontinuum Laguerre-Gaussian and Gaussian beams. *Optics Express* **16**, 10117-10129 (2008).

Chapter 6

Transfer of orbital angular momentum from a ‘white light’ optical vortex to trapped microspheres

6.1 Synopsis and motivation

In Chapter 3, the use of a tightly focused Gaussian beam to optically confine microscopic objects was described. Using the same principles, novel beams are also able to exert forces on microscopic objects. Optical vortices have a spiral phase front, which gives rise to orbital angular momentum. This orbital angular momentum can be transferred to microscopic objects making them rotate.¹ Spin angular momentum arises due to the circular or elliptical polarization of light and can be used to rotate birefringent objects.² Using a beam with both spin and orbital angular momentum, it has been demonstrated³ that the spin and orbital angular momentum components can add or subtract from each other. The use of a broadband, low temporal coherence source to generate a ‘white light’ optical vortex opens up opportunities to further investigate the fundamental properties of light.

A forked diffraction hologram can be used to generate a ‘white light’ optical vortex in the first diffracted order. However, the dark central cores of the different wavelength vortices are laterally displaced due to dispersion, so there is not a dark core in the centre of the ‘white light’ vortex. In 2003, a dispersion compensation method designed to overlap the different wavelength vortices was presented.⁴ A halogen ‘white light’ source was incident on a computer generated hologram. The hologram imparted the required $2\pi l$ phase shift on the first order diffracted beam. The transverse chromatic dispersion was compensated using a prism placed in the image plane of the hologram. The first truly ‘white’ optical vortex was born. The first use of a supercontinuum source to generate an optical vortex was in 2006 by Stzul *et al.*⁵ The use of a high power white light source, such as a supercontinuum source, to generate an optical vortex opens up the opportunity to carry out optical manipulation. This allows an investigation into whether an optical vortex generated using a source with low temporal coherence can transfer orbital angular momentum to microscopic objects.

In this chapter, a supercontinuum source is used to generate an optical vortex. The transfer of orbital angular momentum from the ‘white light’ vortex to polymer microspheres is demonstrated. The rotation rate of three microspheres in a ‘white light’ vortex is measured for different laser powers. Additionally, the effect on the rotation rate of the trapped spheres when varying the azimuthal index of the vortex was investigated. More information about optical vortices can be found in Section 4.2.

6.2 Transfer of orbital angular momentum

6.2.1 Experimental setup and method

I investigated the transfer of orbital angular momentum from a ‘white light’ vortex to trapped polymer microspheres (refractive index $n_s = 1.59$). The visible part of the supercontinuum spectrum, see Figure 6.1, was selected using a mirror that reflected only the visible wavelengths. The beam was expanded to fill the hologram, which was displayed on a spatial light modulator, using lenses L1 and L2. A forked grating hologram (see Section 4.2.3) converted the Gaussian beam into an optical vortex with

azimuthal index $l = 3$ and radial mode index $p = 0$ (the reason for the addition of a grating to the hologram is explained in Section 4.6). Due to the wavelength dependent diffraction angle, the different wavelength vortices were spatially dispersed after the hologram. Dispersion compensation was achieved by imaging the hologram, using lenses L3 and L4, onto a prism of opposite dispersion (refer to Section 4.7 and Figure 4.14 for more detail on dispersion compensation). An aperture was used after lens L3 to select the +1 order diffracted beam (refer back to Section 4.6). Adjusting the grating spacing of the hologram helped to fine tune the dispersion compensation. An objective lens (Nikon $\times 100$, N.A. 1.4) was used to focus the optical vortex into a sample of microspheres ($1\mu\text{m}$ diameter). Wavefront correction was applied to the beam as described in Appendix A. This was to correct for aberrations in the beam and improve the beam profile. As described in Section 5.2.1, illumination was achieved from above the sample using an LED emitting at 950nm . Figure 6.1 shows the experimental setup, a picture of the $l = 3$ ‘white light’ vortex beam and the spectrum of the beam taken after the objective lens.

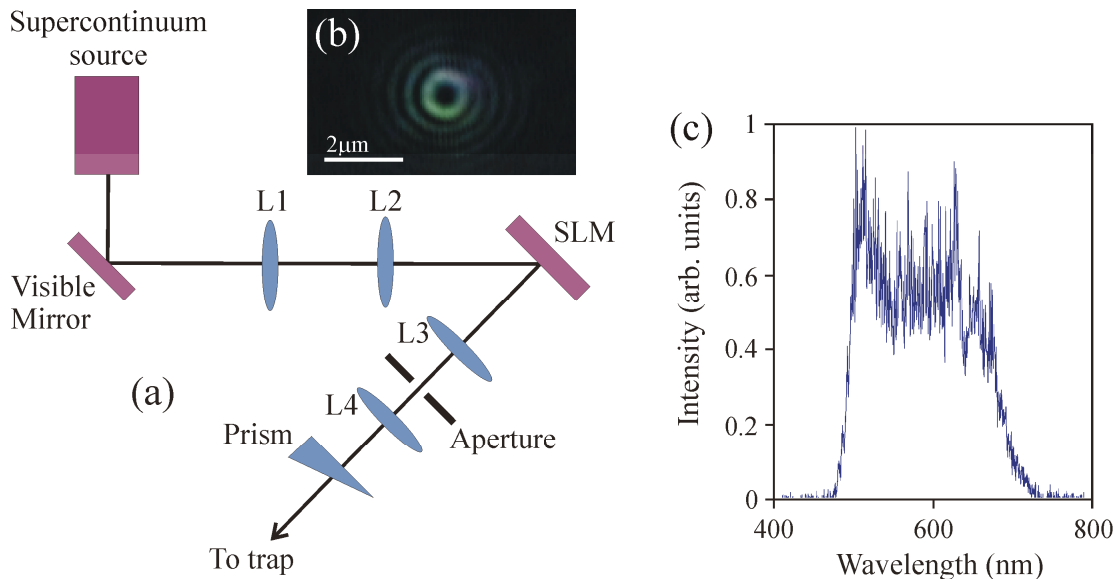


Figure 6.1. The setup is shown in diagram (a). A mirror reflecting the visible wavelengths was used to select the visible spectrum of the supercontinuum beam for the experiment. Achromatic lenses L1 (50mm) and L2 (250mm) were used to expand the beam to fill the hologram displayed on the spatial light modulator (SLM). Achromatic lenses L3 (200mm) and L4 (160mm) were used to image the hologram onto the prism (Comar 10JW25) to compensate the dispersion. An objective lens ($\times 100$ N.A. 1.4) focused the beam into the sample. An aperture was used to select the +1 order diffracted beam. Image (b) is a picture of the $l = 3$ vortex beam and (c) is the spectrum of the beam taken using an AVASPEC 3648 spectrometer in the trapping plane. The specifications for the SLM (Holoeye 2500) are given in Table 4.1.

Although a single microsphere was drawn into the high intensity region of the optical vortex, reliable rotation of the single sphere around the intensity ring of the vortex was not observed. This is because the azimuthal intensity of the optical vortex was not uniform. A single sphere in the high intensity ring of the vortex became optically trapped at the place with the highest intensity. Intensity cross-sections of the ‘white light’ vortex in the horizontal and vertical axes are shown in Figure 6.2. The intensity cross-sections show that there is an intensity variation of up to 30% around the ring of the vortex.

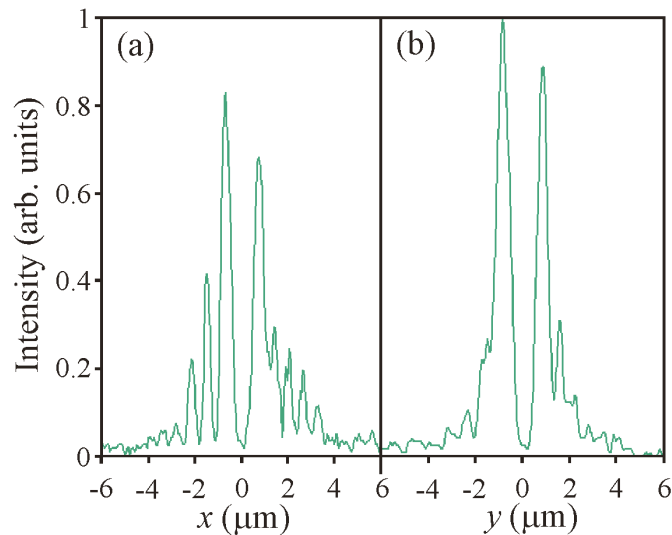


Figure 6.2. Horizontal (a) and vertical (b) transverse intensity cross-sections of the optical vortex pictured in Figure 6.1(b) are shown. It is clear that there are intensity variations of up to 30% around the circumference of the optical vortex.

When multiple spheres were drawn into the vortex, rotation of the ensemble of spheres was observed. The spheres help to ‘push’ each other through the regions of lower intensity allowing all the spheres to make complete rotations around the vortex intensity ring. For the experiments, an ensemble of three polymer spheres of 1μm diameter was used. The spheres were trapped and rotated in the ‘white light’ vortex trap. Optical trapping was achieved, and the spheres were pushed up against the top coverslide of the sample chamber. A high frame rate CCD camera (Basler pl640-210gm) was used to record the rotation, and the videos were analysed using a computer program. The videos were broken down into picture frames, which were then imported into the program. The program fitted a triple Gaussian over the ensemble of three spheres for each frame of the video. The parameters that were fitted were x_p and y_p , which determined the co-

ordinates of the centre of the sphere ensemble, α_{rot} which is the angle that the three Gaussian sphere ensemble had rotated since the first frame of the video, a which determined the starting z position of the fit and b which determined the amplitude of the fitted function. A graph was then plotted of α_{rot} as a function of video frame number (N_{fr}). The frame rate of the camera was f_{rate} and the final value of α_{rot} is denoted by α_{final} . The number of complete rotations of the sphere ensemble per second was determined to be

$$\Omega = \frac{\alpha_{final}}{2\pi} \left(\frac{f_{rate}}{N_{fr}} \right). \quad (6.1)$$

Figure 6.3(a) is an example of the function fitted to the sphere ensemble. Figure 6.3(b) is an example of an output graph from the program. Figure 6.3(c) shows the first 12 frames of a video of the rotating spheres with the corresponding computer generated density plots.

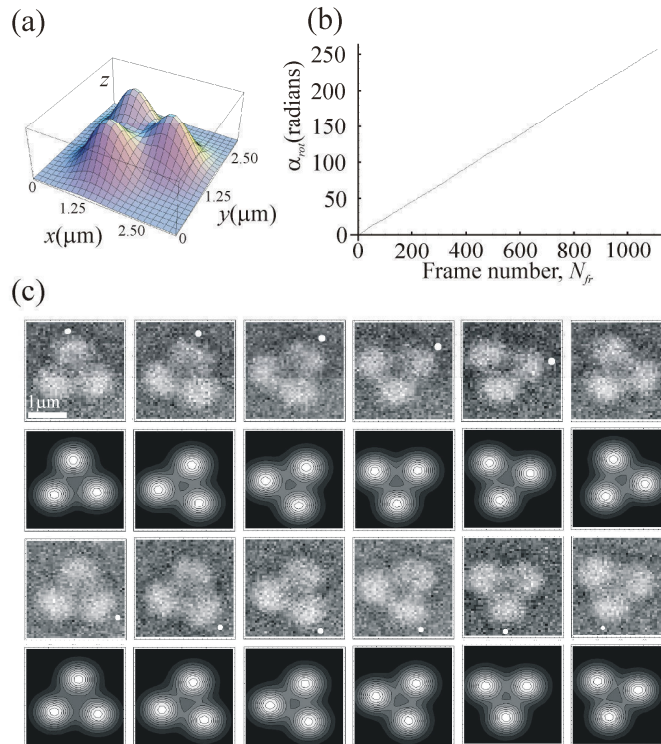


Figure 6.3. An example of the three-Gaussian function that the program fitted over the sphere ensemble is shown in image (a). Image (b) is an example output graph of N_{fr} vs α_{rot} . The first and third rows of image (c) show 12 consecutive frames from a video taken of the rotating spheres, the corresponding density plots are shown underneath each frame. The white dot was added to the images for reference. The laser power in the trapping plane for the data shown in images (b) and (c) was 22mW.

6.2.2 Results

Six videos of the rotating spheres were taken at each power, and the rotation rate of the spheres in each case was determined. The highest rotation rate from the six videos was taken in each case and plotted against the laser power. The results can be seen in Figure 6.4 along with an insert of a density plot of the trapped spheres. The rotation rate per mW was determined to be $0.194 \pm 0.008\text{Hz/mW}$, where the uncertainty in the gradient of the graph was obtained using the method described in reference [6].⁶ At least 50 rotations of the ensemble were averaged over for each point presented. Due to variations in the surface friction between measurements, some of the points lie outside the error bar range. The microspheres were confined in the transverse plane by the optical vortex. Confinement in the axial direction was due to the spheres being pushed up against the top of the sample chamber by radiation pressure from the beam.

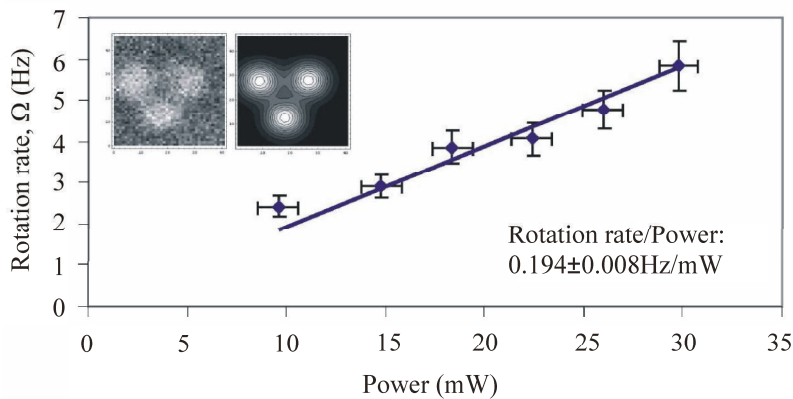


Figure 6.4. The graph shows that there is a linear relation between the rotation rate of the spheres and the laser power. The insert shows the three trapped spheres and the corresponding density plot produced by the computer program. The uncertainty in the rotation rates was $\pm 10\%$ and the uncertainty in the power was $\pm 1\text{mW}$.

Looking at Figure 6.1(b), we can see that some of the power in the vortex beam was lost to higher order p modes. These higher order modes had azimuthal index $l = 3$ and radial mode index $p = 1, 2, 3 \dots$ ⁷ A transverse cross-section was taken of the beam profile of the vortex shown in 6.1(b). A program written by Michael Mazilu was used to find the best fit parameters of a superposition of Laguerre Gaussian modes to the beam cross-section. The beam waist and percentage of power in the $p = 0$ mode were determined using this program. The beam waist of the vortex with $l = 3$ was 780nm and approximately 50% of the total measured power was attributed to the $p = 0$ mode. When

taking the lower power into account, the actual rotation rate is 0.39Hz/mW. This is comparable to the theoretical value of 0.44Hz/mW calculated in Appendix B. The theoretical graphs showing how the rotation rate per unit power and the centripetal force per unit power vary with wavelength are shown in Figure 6.5.

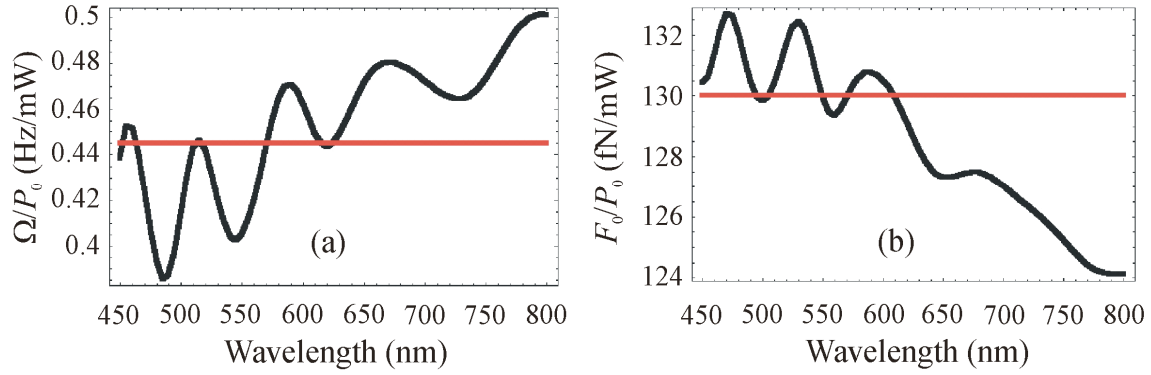


Figure 6.5. Calculations are based on three polymer spheres in a vortex with $l = 3$, $p = 0$ and a beam waist of $w_0 = 640$ nm. The resultant values are displayed in the above graphs. Graph (a) shows how the rotation rate per unit power (Ω / P_0) varies as a function of wavelength. Graph (b) shows how the centripetal force per unit power (F_0 / P_0) varies with wavelength. In both (a) and (b) the red line represents the value calculated by averaging over the supercontinuum spectrum.

Next, we were interested in finding out how the rotation rate of the three spheres trapped in an optical vortex would vary with the l value of the beam. The trapping power was kept constant at 15mW and rotation rates were determined for beams with $l = 2, 3, 4$ and 5. Again, optical trapping was achieved and the spheres were pushed up against the top of the sample chamber. The beam waists of the vortices with different l values were determined by finding the best fit to the profile of the beam.

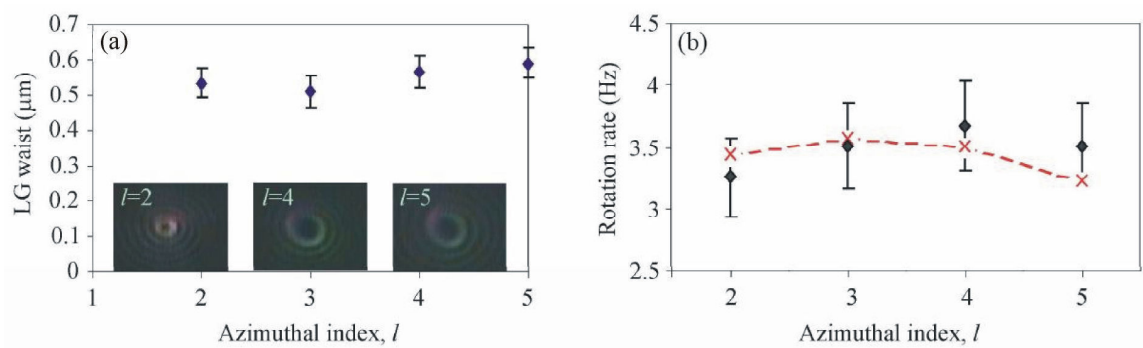


Figure 6.6. The beam waists for the $l = 2, 3, 4$ and 5 vortex beams are plotted in image (a) along with pictures of the $l = 2, 4$ and 5 vortices. A picture of the vortex with $l = 3$ is shown in Figure 6.1(b). A graph of the rotation rate of the sphere ensemble as a function of l is shown in graph (b). The error bars are $\pm 10\%$ for each point. The power in the trapping plane was 15mW. The theoretical points are indicated by the red crosses and a dashed line has been added to guide the eye.

Figure 6.6 shows how the beam waist and rotation rate varied with l value. The maximum rotation rate of the group of spheres was found to occur when $l = 4$. The beam waists for the vortices with different l values were determined in the same way as the beam waist for the vortex with $l = 3$ as described above. Figure 6.6(a) is a graph of the beam waists as a function of l value. Figure 6.6(b) shows the rotation rate of the ensemble of three spheres (each sphere was $1\mu\text{m}$ in diameter) in vortices with l values of 2, 3, 4 and 5.

6.3 Discussion

It has been shown that orbital angular momentum can be transferred from a supercontinuum ‘white light’ optical vortex to an ensemble of three polymer spheres. The spheres were confined along the beam propagation axis by the coverslip at the top of the sample chamber during rotation. Transverse confinement of the spheres was achieved using the optical gradient force. The sphere ensemble rotation was non-uniform. This may be due to the intensity variation around the optical vortex ring and the interaction of the spheres with the top coverslip. This is why the average rotation rate was taken over at least 50 complete rotations of the ensemble.

The rotation of a single sphere was not achieved due to an uneven intensity profile around the ring of the vortex. A single sphere became trapped in the most intense part of the vortex ring. The intensity fluctuated by up to 30% around the ring of the vortex. This is why an ensemble of three spheres was chosen for the experiments. The spheres helped to ‘push’ each other through the lower intensity regions of the vortex ring. Using the maximum intensity gradient around the vortex, the force due to the intensity gradient can be calculated using Equation 3.1 and was found to be $9.32 \times 10^{-12} \text{N}$. To find the torque due to the intensity variation, the gradient force is multiplied by the radius of maximum intensity of the vortex, which is $0.78\mu\text{m}$. This gives a torque of $7.27 \times 10^{-18} \text{Nm}$. The torque due to the orbital angular momentum of the beam can be calculated using Equation 4.10, where the centre frequency of the spectrum is $5.17 \times 10^{14} \text{Hz}$. The torque due to OAM for a beam with a power of 9.6mW is $8.83 \times 10^{-18} \text{Nm}$. The torque due to the

OAM of the beam is of a similar magnitude to the torque resulting from the intensity gradient in the beam. This demonstrates why a single object rotating in the beam may become ‘stuck’ in a high intensity region around the ring of the vortex.

When investigating the variation of rotation rate with azimuthal index, the rotation rate of the sphere ensemble did not show significant variation with l value from $l = 2$ to $l = 5$. If the spheres were not trapped at the optimum axial position in the vortex, the maximum possible rotation rate would not be achieved. The radius of maximum intensity of the vortex increases with l value. For a vortex with $l = 6$, I observed that the spheres were no longer rotating as an ensemble. The spheres were separated from each other due to the large radius of the vortex intensity maximum. The situation for $l = 6$ was therefore not comparable to the other data. As a result, data obtained using an optical vortex with $l = 5$ was the highest value that was included in the investigation.

I have demonstrated that orbital angular momentum can be transferred from a broadband ‘white light’ optical vortex to trapped microspheres. The experiments presented in this chapter demonstrate that an optical vortex generated using a light source with low temporal coherence has orbital angular momentum, and that this momentum can be transferred to trapped objects. Related work has been carried out by Wright *et al.*⁸ To further this work, it would be interesting to investigate the effect of low spatial coherence on the transfer of orbital angular momentum to microspheres.

The work in this chapter was published in Optics Express⁹ along with the work presented in Chapter 5.

Acknowledgements

The program used to generate the holograms was written by Daniel Burnham and David McGloin. The program used to apply the wavefront correction was written by Tomáš Čižmár. The program used to analyse the microsphere rotation videos was written by Michael Mazilu. The Author set up the experiment and obtained and analysed all data.

References

1. Ladavac, K. & Grier, D. Microoptomechanical pumps assembled and driven by holographic optical vortex arrays. *Opt. Express* **12**, 1144-1149 (2004).
2. Beth, R. A. Mechanical detection and measurement of the angular momentum of light. *Physical Review* **50**, 115-125 (1936).
3. Simpson, N. B., Dholakia, K., Allen, L. & Padgett, M. J. Mechanical equivalence of spin and orbital angular momentum of light: An optical spanner. *Optics Letters* **22**, 52-54 (1997).
4. Leach, J. & Padgett, M. J. Observation of chromatic effects near a white-light vortex. *New Journal of Physics* **5** (2003).
5. Sztul, H. I., Kartazayev, V. & Alfano, R. R. Laguerre-Gaussian supercontinuum. *Optics Letters* **31**, 2725-2727 (2006).
6. Experimental errors and graphs. *University of St Andrews undergraduate lab script*, 32-35.
7. Arlt, J., Dholakia, K., Allen, L. & Padgett, M. J. The production of multiringed Laguerre-Gaussian modes by computer-generated holograms. *Journal of Modern Optics* **45**, 1231-1237 (1998).
8. Wright, A. J., Girkin, J. M., Gibson, G. M., Leach, J. & Padgett, M. J. Transfer of orbital angular momentum from a super-continuum, white-light beam. *Optics Express* **16**, 9495-9500 (2008).
9. Morris, J. E. et al. Optical micromanipulation using supercontinuum Laguerre-Gaussian and Gaussian beams. *Optics Express* **16**, 10117-10129 (2008).

Chapter 7

Propagation characteristics of Airy beams

7.1 Synopsis and motivation

The existence of the Airy wavepacket was predicted in 1979 by Berry *et al.*¹ The experimental realisation of the optical Airy beam was in 2007 when a finite Airy solution to the paraxial wave equation was discovered.² Similar to the Bessel beam, the finite Airy beam can propagate ‘diffraction-free’ over a finite distance. The parabolic trajectory of the Airy beam is particularly noteworthy because it is a unique property that is shared only with the parabolic beam.^{3,4} Parabolic beams have a cubic phase front like the Airy beam and are another finite solution to the paraxial wave equation. Since the Airy beam properties had not yet been investigated in detail, I set out to characterise them. In particular, I looked at how the Airy beam properties vary with wavelength and spatial coherence. The experimental procedure and results of this investigation are presented in this chapter. Additionally, the first ever ‘white light’ Airy beam was generated. Without dispersion compensation optics, the ‘white light’ Airy beam has a smeared out transverse intensity profile. However, I show that it is possible to overlap the wavelength components and generate a ‘white light’ Airy beam. More information about the Airy beam is presented in Section 4.4.

7.2 Investigating the properties of Airy beams

7.2.1 Experimental setup and methods

Experiments were carried out to investigate the propagation characteristics of the Airy beam. How the wavelength and spatial coherence of the source affects the Airy beam properties, which are b_0 , x_0 and a_0 , was determined. The deflection coefficient, b_0 , characterises the parabolic propagation of the beam. The characteristic length, x_0 (or y_0 in the y axis) is related to the spacing between the lobes in the beam's transverse intensity profile. The aperture coefficient, a_0 , limits the propagation distance of the beam. There is more information in Section 4.4.3.

First, a 'white light' Airy beam was generated. A mirror that reflects light at visible wavelengths (Comar 25MX02) was used to select the visible spectrum from the supercontinuum source (Fianium Ltd. 4ps, 10MHz). These wavelengths were selected because the SLM (Holoeye 2500) can only produce a 0 to 2π phase shift in the wavelength range 400nm - 700nm. The beam was expanded to fill the face of the SLM using lenses L1 and L2. Filling the hologram with the incident Gaussian beam produces the best quality Airy beam. The experimental setup is shown in Figure 7.1 along with the spectrum of the beam.

A hologram displayed on an SLM imposed a cubic phase shift on the incident beam. This beam must then be Fourier transformed by a lens to generate the Airy beam. Lens L5 acted as the Fourier lens in the 'white light' Airy beam case. A Labview program was used to generate and control the SLM hologram. A diffraction grating was incorporated onto the hologram to spatially separate the different order beams (refer to Section 4.6 and Figure 4.13). The spatial dispersion arising from the wavelength dependent diffraction angle of the beam from the hologram had to be compensated. The +1 diffracted order beam was selected using an aperture placed in the focal plane of lens L3. Refer to Figure 4.13(c) for an illustration of an aperture being used to select the +1 diffracted order beam from a hologram. The hologram was imaged onto a prism (Comar 10JW25) with opposite dispersion using lenses L3 and L4. The grating spacing was then adjusted so that the

prism exactly compensated the spatial dispersion from the hologram. Additionally, wavefront correction was applied to the hologram, see Appendix A, to improve the quality of the beam by compensating the wavefront aberrations.

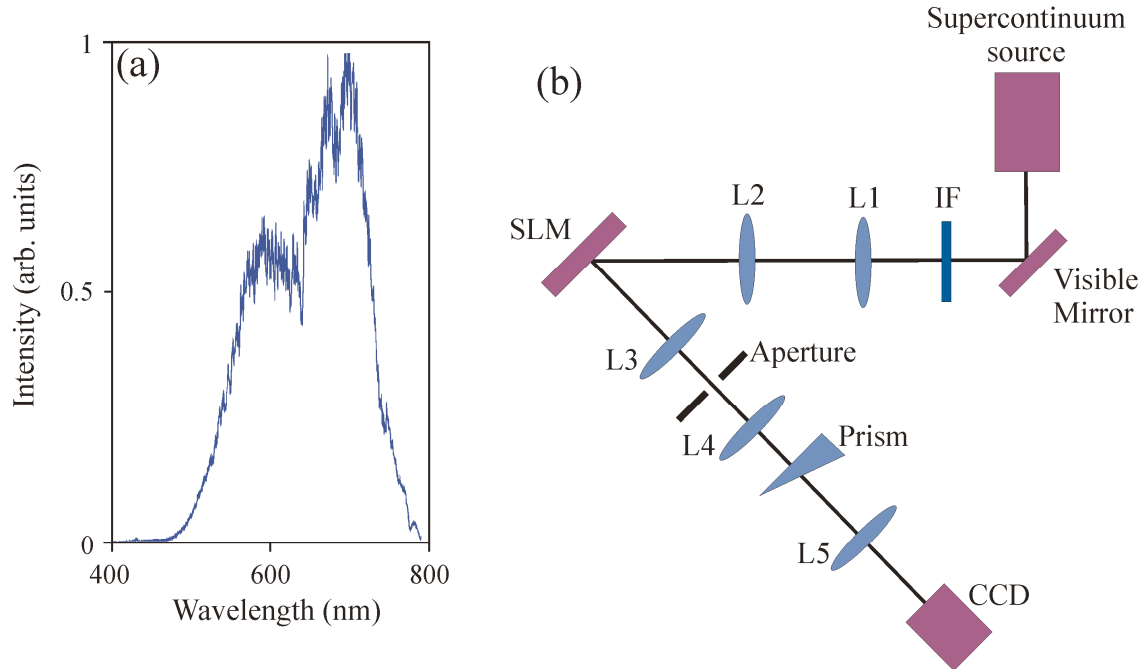


Figure 7.1. The spectrum taken after lens L5 (using an AVASPEC 3648 spectrometer) is shown in image (a) along with the experimental setup in image (b). The visible mirror reflects the visible wavelengths of the supercontinuum source. Lenses L1, L2, L3, L4 and L5 are achromatic doublet lenses with respective focal lengths of 50mm, 500mm, 500mm, 200mm and 250mm. The deflection angle of the prism is 10°. IF denotes the interference filters used to select the wavelengths for the wavelength dependent study. The specifications for the SLM (Holoeye 2500) are given in Table 4.1.

I then moved on to study the effect that varying the wavelength and spatial coherence of the source had on the properties of the Airy beam. Since narrowband Airy beams were now being used, the dispersion compensation equipment was no longer required. Therefore, lenses L4 and L5 were removed from the setup along with the prism. The Fourier lens is now lens L3 for all the following work.

First, the effect of the wavelength of the source on the parabolic trajectory of the beam was investigated. This property can be characterised by the deflection coefficient, b_0 . Interference filters (3nm bandwidth) were used to select wavelengths at 515nm, 546nm, 578nm and 633nm from the supercontinuum beam. Since each wavelength is deflected at a different angle at the hologram, the grating spacing was changed for each beam to

maintain the beam path through the centre of lens L3. The CCD camera (Basler PLA640-210gc) was placed on a rail parallel to the propagation axis of the beam. Images of the beam were taken at around 15 positions along the propagation axis, including before and after the parabola apex ($z = 0$). In order to compensate for any mismatch between the axis of the rail and the propagation axis of the beam, I took data for two beams propagating on opposite parabolic paths. The data from these two beams, oriented at 90° and 270° , could then be averaged.

The position of the main lobe of the beam was obtained from each image and the distance that the beam had travelled across the camera screen, d , using the $z = 0$ position of the main lobe as a reference, was determined using Equation 7.1.

$$d = \sqrt{(x - x_c)^2 + (y - y_c)^2}, \quad (7.1)$$

where (x_c, y_c) are the co-ordinates of the central lobe in the image taken at the apex of the parabola ($z = 0$), and (x, y) are the co-ordinates of the beam's central lobe in each image for $z \neq 0$. A graph of the main lobe displacement as a function of z position was plotted for both the 90° and 270° oriented Airy beams. The blue squares in Figure 7.2 represent the data taken from the Airy beam oriented at 270° . The magnitudes of these deflection values were added to the values of the 90° beam. The combined data is shown by the red circles. The best parabolic fit to the combined data was found and is shown by the red line. The coefficient of the z^2 term of the fit was halved to find the deflection coefficient of the Airy beam.

In order to determine the characteristic length x_0 of the beams, cross-sections of the images taken at the apex of the parabola for each beam (oriented at 90° and 270°) were obtained, and the best fit Airy function was found using a computer program. Values of x_0 were thus obtained from the best fit for the horizontal and vertical lobes of both beams. The average value was determined to be the characteristic length. This process was used to determine x_0 for beams with wavelengths of 515nm, 546nm, 578nm and 633nm.

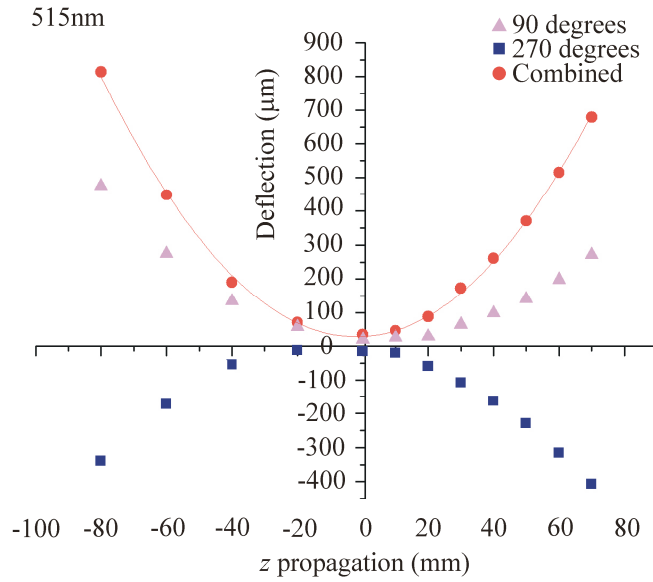


Figure 7.2. The blue squares represent the data taken for the 270° beam, the pink triangles represent data taken with the 90° beam and the red circles represent the magnitude of the points added together at each z position. A parabola was fitted to the combined data and is shown by the red line. The deflection coefficient of the Airy beam could be determined by halving the value of the z^2 coefficient of the fitted parabola.

Similarly, the aperture coefficients were determined by finding the a_0 values of the best fit to the cross-sections of the Airy beam lobes, for both the 90° and 270° oriented beams. The average value was then determined. This was done only for the horizontal lobes because the a_0 values of the vertical lobes were affected by coherence issues due to the diffraction at the hologram. Further explanation of this issue is given in the discussion section of this chapter. Figure 7.3 shows a fit made to the horizontal lobes of the 633nm beam.

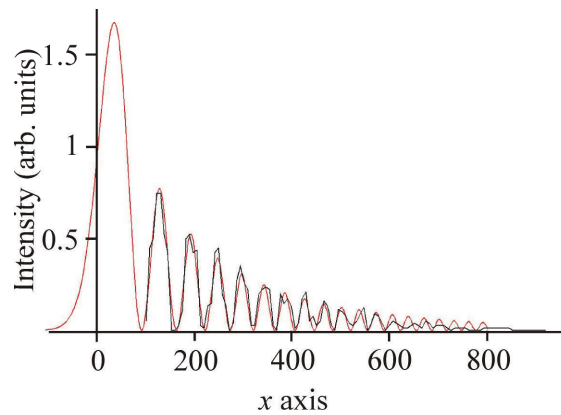


Figure 7.3. The red line is the fitted finite Airy function and the black line is the horizontal cross-section of the 633nm beam's lobes at $z = 0$. The x axis units are in microns, and the intensity axis is measured in arbitrary units.

Next, I investigated how spatial coherence is related to the parameters of the Airy beam. The spatial coherence of a beam is related to the M^2 value, so I measured the M^2 value of each narrowband beam. The Gaussian beam was incident on the SLM face, but no hologram was displayed. The reflected beam was then focused using a lens with a focal length of 500mm. A beam profiler was used to determine the waist of the beam at a number of z positions before and after the focal point. The data was plotted in a graph of $w(z)$ vs z position. A hyperbola was fitted to the data and the best fit parameters for the beam waist, w_0 , and Rayleigh range, z_r , were determined. The hyperbola equation is

$$w(z) = w_0 \sqrt{1 + \frac{(z - z_0)^2}{z_r^2}}, \quad (7.2)$$

where z_0 was the z position of the beam waist. The M^2 value for the beam was then determined with the best fit parameters using Equation 7.3.

$$M^2 = \frac{\pi w_0^2}{\lambda z_r}. \quad (7.3)$$

7.2.2 Results

An image of the ‘white light’ Airy beam and a cross-section of its lobes are shown in Figure 7.4. Two images of the beam were taken at $z = 0$, one when the main lobe was not saturated on the camera and one when the main lobe of the beam was saturated. The saturated picture was taken so that more of the side lobes could be seen clearly in the cross-section. In Figure 7.4, the solid line is the cross-section taken from the saturated picture and the dashed line is a cross-section of the main lobe taken from the unsaturated picture. The intensity of the main lobe cross-section was normalized and overlapped with the cross-section of the side lobes.

The distance between the main peak and the first lobe is equal to $2.25x_0$. The x_0 value for the ‘white light’ beam was determined from the image taken at $z = 0$. The distance was measured between the main peak and the first lobe and divided by 2.25. This gave a value for the characteristic length of $47.25\mu\text{m}$. The cross-section profile shows that the

lobes are clearly defined. The wavelengths are well overlapped confirming that the prism dispersion compensation method was successful.

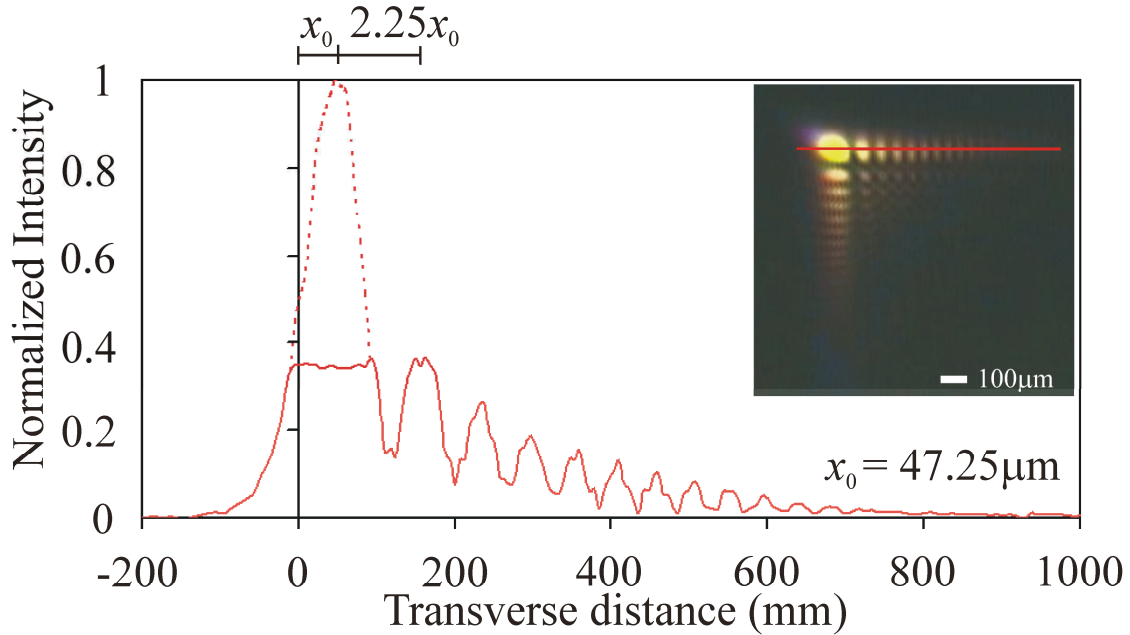


Figure 7.4. A cross-section of the ‘white light’ Airy beam lobes is shown. The insert is an experimentally obtained image of the ‘white light’ Airy beam. The red line in the insert indicates where the cross-section was taken. The dashed main lobe was added by taking the profile from an unsaturated image and overlaying it. The uncertainty in x_0 is $\pm 7.4\mu\text{m}$ (one camera pixel is $7.4\mu\text{m}$).

It is interesting to note that adjusting the grating spacing of the hologram allows control over the dispersion of the Airy beam. It is therefore possible to control the offset of the different wavelength Airy beams, see Figure 7.5.

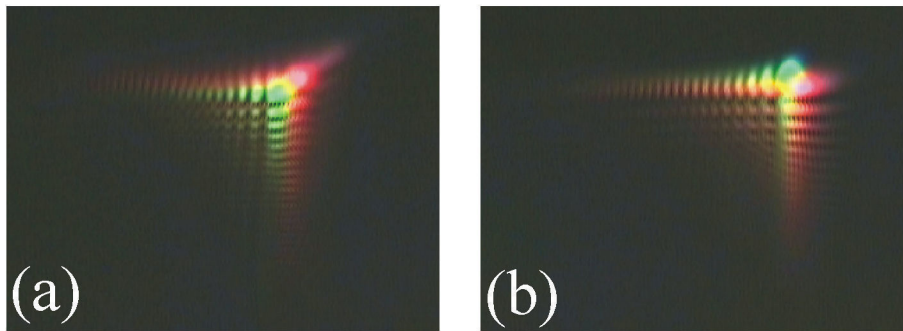


Figure 7.5. Picture (a) shows how the beams are offset when the x axis grating spacing is changed to emphasize dispersion effects, and picture (b) shows the beams when the y axis grating spacing is changed.

Next, an investigation into how the parabolic propagation of the Airy beam varies with wavelength was carried out. This was done by looking at the deflection coefficient, b_0 , of

the beam's parabolic trajectory. Figure 7.6 shows how the beam deflection varies with wavelength. Also shown are pictures of each beam taken at $z = 0$.

The shorter wavelength components were found to have a larger deflection coefficient than the longer wavelength components. Although Equation 7.4 suggests that the deflection coefficient should increase with λ^2 , this is not the case since x_0 also varies with wavelength as per Equation 7.5. Appendix C contains the theoretical background to the work in this chapter.

$$b_0 z^2 = \frac{\sqrt{2}\lambda^2}{16\pi^2 x_0^3} z^2, \quad (7.4)$$

$$x_0 = \frac{c_0 f_{lens}}{2\pi} \lambda, \quad (7.5)$$

where b_0 is the deflection coefficient, λ is the wavelength, x_0 is the characteristic length and $c_0 = \sqrt[3]{3\varphi}/l_h$ where φ is the maximal phase shift on the SLM, l_h is the side length of the hologram and f_{lens} is the focal length of the Fourier lens. The phase was imposed diagonally across the hologram from $-20 \times 2\pi$ to $+20 \times 2\pi$, therefore the maximal phase shift across the hologram is $\varphi = 40 \times 2\pi$. The side length of the hologram was $l_h = 0.0146\text{m}$, so the value of c_0 for our experiment was calculated to be 785.9m^{-1} .

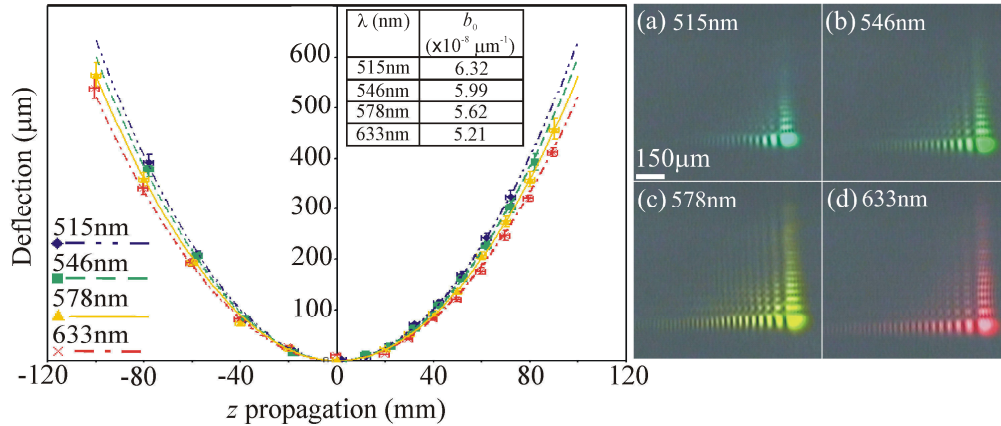


Figure 7.6. The parabolic trajectory of the Airy beam as a function of wavelength is shown. The table insert gives the values of the deflection coefficients. On the right are images of the beams taken at the parabola apex. The uncertainty in the deflection was determined by taking the uncertainty in the position of the Airy beam main lobe to be ± 1 pixel ($7.4\mu\text{m}$) and combining the uncertainties from both the 270° and 90° beams. The uncertainty in the z position is $\pm 2\text{mm}$.

The x_0 values were determined by three methods and are shown in Table 7.1. Firstly, the values were obtained from the fitted Airy beam function to the lobe cross-section of the beam. The values are shown in the column labelled ‘Direct fit’ in Table 7.1. Secondly, I took the values of the deflection coefficients, b_0 , that were determined previously and calculated the expected x_0 values from this information using Equation 7.4. Finally, the information about the phase imposed on the incident beam by the hologram, φ , and the focal length of the Fourier lens, f_{lens} , was used to calculate the expected x_0 values with Equation 7.5. Good agreement is observed between the x_0 values obtained from all three methods. It is clear that x_0 increases with increasing wavelength. Table 7.1 shows all the determined x_0 values.

Table 7.1.

λ (nm)	x_0 (μm) Direct fit	x_0 (μm) Equation (7.4)	x_0 (mm) Equation (7.5)
515	32.77±1.46	33.49	32.21
546	34.34±1.58	35.45	34.15
578	36.60±0.81	37.60	36.15
633	39.67±1.41	40.99	39.59

The uncertainty in the ‘Direct fit’ data is the standard deviation of the values that were averaged to obtain the stated x_0 value. Using the images of the beams at the parabola apex, the aperture coefficient was determined by fitting the Airy function to the beam cross-sections. The aperture coefficient does not vary with wavelength but it does vary with the spatial coherence of the beam. The M^2 values of the different wavelength beams incident on the SLM were measured to determine the spatial coherence, see Equation 7.7. The method used to measure the M^2 values was described at the end of Section 7.2.1. The M^2 value was different for each wavelength beam, which meant that the aperture coefficient was different in each case. By measuring the properties of the beam incident on the SLM, Equation 7.6 can be used to calculate the expected a_0 value for each beam.

$$a_0 = \frac{1 + (M^2)^2}{2c_0^2 w_{SLM}^2}, \quad (7.6)$$

$$\sigma_{\mu} = \frac{w_0^2}{(M^2)^2 - 1}, \quad (7.7)$$

where σ_{μ} is the spatial coherence of the beam, c_0 is as described earlier and w_{SLM} is the waist of the beam incident on the SLM. The determined a_0 values are shown in Figure 7.7. The blue points were determined by fitting the Airy function to cross-sections of the beam, a dashed line is shown to guide the eye. The red points were calculated using Equation 7.6.

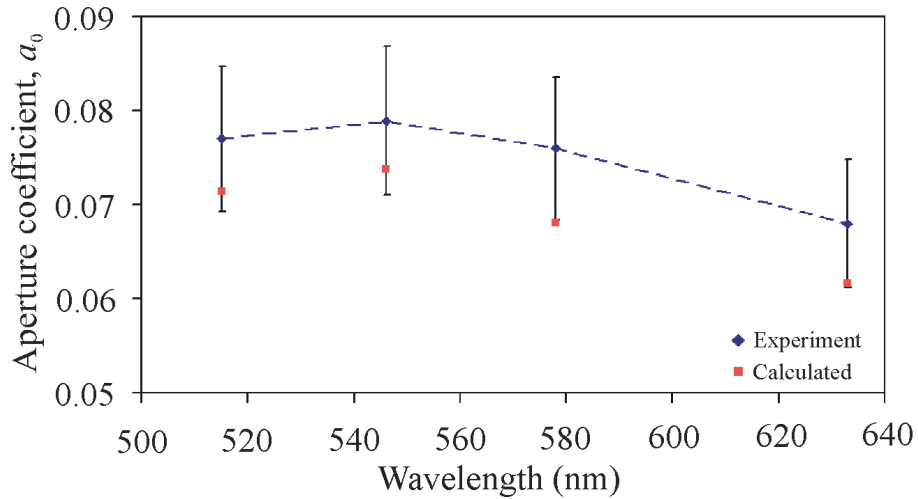


Figure 7.7. The blue points were determined by fitting an Airy function to a cross-section of the horizontal beam lobes at the focus. The red points show the decay constant values predicted by Equation 7.6. The uncertainty in the a_0 value is $\pm 10\%$.

Table 7.2.

λ (nm)	w_{SLM} (mm)	M^2	a_0	
			Direct fit	Equation (7.6)
515	5.44	1.27	0.077	0.071
546	5.33	1.26	0.079	0.074
578	5.31	1.17	0.076	0.068
633	5.66	1.20	0.068	0.062

Table 7.2 shows the measured beam waists incident on the SLM, the M^2 values and the aperture coefficients. The aperture coefficients in the column labelled ‘Direct fit’ were determined from the beam images and those in the column labelled ‘Equation 7.6’ were determined using Equation 7.6.

7.3 Discussion

A computer generated hologram was used to impose a cubic phase shift on an incident supercontinuum beam. The resultant beam was transmitted through a lens and a ‘white light’ Airy beam was generated. After the hologram the different wavelength beams were spatially dispersed due to diffraction. The dispersion was compensated using a prism with opposite dispersion similar to the method used in the experiments presented in Chapters 5 and 6.

Narrowband interference filters were then placed in the beam path to select wavelengths of 515nm, 546nm, 578nm and 633nm. An investigation into the dependence of the Airy beam properties on wavelength and spatial coherence was then carried out. The results show that the parabolic trajectory of the beam depends on wavelength. The trajectory is steeper for beams with a short wavelength. The lobe spacing of the Airy beam is also wavelength dependent, where shorter wavelength beams have smaller lobe spacing. The aperture coefficient, which affects the propagation distance of the beam, was dependent on the spatial coherence of the source but was not dependent on wavelength.

A grating was added to the hologram to spatially separate the different order beams. As a result, the a_0 value of the Airy beam lobes was different for the horizontal and vertical axes. It is thought that this was because of a coherence issue. The deflection due to diffraction from the hologram was only in the vertical axis, and this deflection introduced a path difference between the different rays across the beam. As a consequence, the spatial coherence of the beam was reduced in the vertical axis. It is thought that, since the beam was not deflected in the horizontal axis, the spatial coherence was not affected. Therefore, the a_0 value determined for the lobes on the vertical axis was higher than that determined for the lobes on the horizontal axis. Since the M^2 values for each beam, which were used to calculate the theoretical values, did not take into account this reduction in coherence, only the horizontal values were used in order to compare them with the theory.

The characteristic length was determined in a different way for the ‘white light’ Airy beam than for the narrowband Airy beams. Although the Airy beam lobes were well defined, it was not possible to fit an Airy function to the cross-section of the ‘white light’ Airy beam lobes. This is because some of the Airy beam properties vary with wavelength. The spacing between the main lobe and the first lobe of an Airy beam is $2.25x_0$. This was determined by studying simulated plots of the Airy beam. This relation was used to determine the x_0 value for the ‘white light’ Airy beam.

Since a detailed characterisation of the Airy beam had not yet been carried out, the work in this chapter is important for setting the groundwork for future studies using this beam. Of particular interest is the wavelength dependent trajectory of the beam. In the ‘white light’ Airy beam, the ability to offset the different wavelength beams enhances the difference in their trajectories. This may then provide optical sorting applications if nanoparticles with different properties could be selectively guided by the different wavelength beams. Optical guiding has already been achieved using a narrowband Airy beam.⁵

The work presented in this Chapter was published in Optics Express.⁶

Acknowledgements

The Labview program used to generate the holograms was written by Jörg Baumgartl. Tomáš Čižmár’s program was used to carry out the wavefront correction. The theoretical background presented in Appendix C was carried out by Michael Mazilu. The program used to find the best fit to cross-sections of the beams was written by Michael Mazilu. The experimental setup was constructed by the Author, and all data was obtained and analysed by the Author.

References

1. Berry, M. V. & Balazs, N. L. Non-spreading wave packets. *American Journal of Physics* **47**, 264-267 (1979).
2. Siviloglou, G. A., Broky, J., Dogariu, A. & Christodoulides, D. N. Observation of accelerating airy beams. *Physical Review Letters* **99**, 213901 (2007).
3. Bandres, M. A. Accelerating parabolic beams. *Opt. Lett.* **33**, 1678-1680 (2008).
4. Davis, J. A., Mintry, M. J., Bandres, M. A. & Cottrell, D. M. Observation of accelerating parabolic beams. *Opt. Express* **16**, 12866-12871 (2008).
5. Baumgartl, J., Mazilu, M. & Dholakia, K. Optically mediated particle clearing using Airy wavepackets. *Nat Photon* **2**, 675-678 (2008).
6. Morris, J. E., Mazilu, M., Baumgartl, J., Cizmar, T. & Dholakia, K. Propagation characteristics of Airy beams: dependence upon spatial coherence and wavelength. *Optics Express* **17**, 13236-13245 (2009).

Chapter 8

Characterisation of spiralling and snaking Bessel beams

8.1 Synopsis and motivation

In the previous chapter we were introduced to the Airy beam, which is a beam that propagates along a parabolic path. The Airy beam led us to consider other non-straight propagating beams. The idea of generating a ‘diffraction-free’ beam that can rotate about the optic axis as it propagates was first proposed by Paterson *et al.*¹ By fabricating a hologram that produces a superposition of two Bessel beams with different spatial frequencies, they demonstrated that such a beam can exist. In 2005, Alonzo *et al.*² proposed a beam that has a transverse intensity profile in the form of a spiral and called it a ‘helico-conical’ beam. However, the specific work that is built upon in this chapter was published by Jarutis *et al.*³ in 2009. They presented a theoretical study discussing the possibility of generating a zero order Bessel beam whose transverse intensity profile spirals around the optic axis as it propagates. The ability to design such unusual beam propagations could be a powerful tool that is useful for the guiding of particles along complex trajectories and around obstructions. Related work has also been carried out recently.^{4,5}

This chapter presents the experimental realization of a Bessel beam that propagates along a spiralling path (SpBB) and the characterisation of the propagation of this beam. By varying the parameters of the beam, a variety of non-straight trajectories for Bessel beams are possible. For example, a beam that propagates along a ‘snaking’ path was generated. The central core of a snaking Bessel beam (SnBB) deviates from the optic axis in only one transverse axis. I characterise the propagation of the snaking Bessel beam and demonstrate that such a beam can propagate around obstructions placed on the propagation axis. The beam parameters were able to be controlled by adjusting the input variables when generating the holograms.

8.2 Background to spiralling and snaking Bessel beams

An ordinary zero order Bessel beam can be generated using a conical lens called an axicon. Section 4.3.2 describes how to generate an ‘ordinary’ Bessel beam using an axicon and Figure 4.6(b) illustrates this method. To generate a spiralling Bessel beam in a similar way, some adjustments would have to be made to the axicon. Jarutis *et al.*³ suggested that an axicon could be cut into slices and each consecutive segment displaced to create a spiral of segments around the optic axis. This concept is illustrated in Figure 8.1. A Gaussian beam propagating through such an optical element would then propagate along a spiralling path.

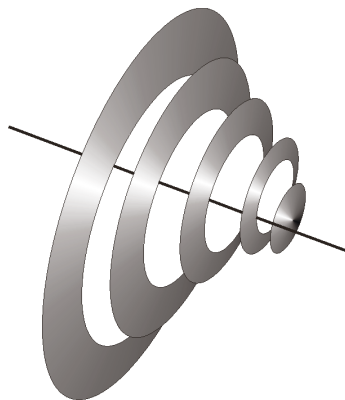


Figure 8.1. An illustration of slices of axicon that have been displaced relative to each other in a spiral. Such an optical element could be used to generate a spiralling Bessel beam without the use of a hologram.

The main parameters of the spiralling Bessel beam are the maximum displacement of the beam from the propagation axis, the pitch of the spiral propagation and the size of the central core of the beam.

A hologram can be used to generate a Bessel beam by simulating the effect of an axicon on an incident Gaussian beam. The effect of the axicon can be described by the following transfer function:

$$F(r) = \exp(-ik\gamma r), \quad (8.1)$$

where r is the radial distance from the apex of the axicon and is related to the transverse co-ordinates x and y by $r = \sqrt{x^2 + y^2}$, k is the wavevector and γ is the angle of the deflected wavevectors after the axicon. If the base angle of the axicon is α and the refractive index of the axicon material is n_x , then $\gamma \approx (n_x - 1)\alpha$.

To generate a spiralling Bessel beam, the transfer function in Equation 8.1 can be modified such that³

$$F_{\Delta, \Gamma}(r, \phi) = \exp\{-ik\gamma r + ik\gamma\Delta \cos(\phi - \Gamma r)\}, \quad (8.2)$$

where Δ is the deviation of the beam from the propagation axis and has a small value. The period of the Bessel beam's spiral path is given by $2\pi/(\Gamma\gamma)$ and $\Gamma = 2\pi/P$, where P is the period of the spiral phase applied to the beam.⁵ When the phase from Equation 8.2 is imposed on an incident Gaussian beam, it simulates an axicon that is rotating around the beam's propagation axis and is displaced from that axis by Δ . This causes the position of the generated Bessel beam to rotate as it propagates. Experimentally, a hologram simulating the phase given by Equation 8.2 can be displayed on a spatial light modulator. A Gaussian beam incident on the hologram will then become a Bessel beam that propagates along a spiralling path. Relating to Equation 4.12, we have

$$\psi(r) = \text{mod}\left(\frac{2\pi}{\lambda} r\gamma - \frac{2\pi}{\lambda} \gamma\Delta \cos(\phi - \Gamma r), 2\pi\right), \quad (8.3)$$

where $\text{mod}(a, b)$ gives the remainder of a/b .

A snaking Bessel beam oscillates in one transverse axis as it propagates. Such a beam can be thought of as a superposition of two spiralling phase terms with opposite helicity to each other. The two spiralling phase terms are $k\gamma\Delta \cos(\phi - \Gamma r)$ and $k\gamma\Delta \cos(\phi + \Gamma r)$. The resulting transfer function is

$$F_{\Delta,\Gamma}(r, \phi) = \exp(-ik\gamma r + 2ik\gamma\Delta \cos(\phi) \cos(\Gamma r)). \quad (8.4)$$

In accordance with Equation 4.12, we have

$$\psi(r) = \text{mod}(k\gamma r + 2k\gamma\Delta \cos(\phi) \cos(\Gamma r), 2\pi). \quad (8.5)$$

There is now a discussion of how the propagation of the beam was modelled. The electric field at $z = 0$ (the SLM plane) is given by the product of the incident Gaussian beam, with beam waist, w_{inc} , and the hologram phase (Equation 8.2 for the spiralling beam) imposed by the hologram, which is

$$E(r, \phi, z = 0) = \exp\left(-\left(\frac{r}{w_{inc}}\right)^2 - 2\pi i(k\gamma r + k\gamma\Delta \cos(\phi - \Gamma r))\right). \quad (8.6)$$

For a monochromatic source, the angular spectrum plane waves method⁶ can then be used to determine the transverse electric field at a position $z > 0$. We multiply the Fourier transform of Equation 8.6, which gives us the angular spectrum at $z = 0$, by the propagator $\exp(-ik\gamma_d z)$. The initial field (at $z = 0$) splits into plane wave components as it propagates a distance z . The direction cosines of these plane wave components is represented by γ_d . The inverse Fourier transform of this then gives the electric field at the transverse plane at position z .

Using different parameters to generate the holograms, spiralling beams that had different core sizes, axial deviations and number of rotations could be produced. The parameter α represents the base angle of an axicon and determines the grating spacing of the hologram, and the core size of the beam produced. The deviation of the central core from the propagation axis is determined by Δ , and the pitch of the spiral is $2\pi/\Gamma\gamma$. Γ is stated in pixels^{-1} throughout this chapter but can be converted to units of mm^{-1} by dividing the pixel value of Γ by the size of an SLM pixel (0.02mm). Likewise, the deviation Δ is given in SLM pixels but can be converted to millimetres by multiplying Δ

by 0.02mm. When choosing the parameters for the beam, the trade off between Δ and Γ must be taken into consideration. If Δ is increased, then the value of Γ must be reduced. However, this results in fewer complete spirals of the beam during propagation.

8.3 Experimental realisation of spiralling and snaking Bessel beams

8.3.1 Experimental setup

A ytterbium fibre laser (IPG photonics) emitting at 1070nm was used for the experiments. The experimental setup is shown in Figure 8.2 and was used to generate both the spiralling and snaking Bessel beams. The holograms used to generate the beams were displayed on a spatial light modulator (Hamamatsu LCOS x10468, refer to Table 4.1 for more detail). The laser beam, which had a waist of 5mm, was expanded to fill the face of the SLM using lenses L1 and L2. The Bessel beam was then imaged onto a CCD camera (Basler plA640-210gm) via lenses L3 and L4. The zero order diffracted beam manifested as a bright spot at the centre of concentric rings of light, which are formed by higher order diffracted beams. Figure 8.2(b) shows the diffracted beams in more detail.

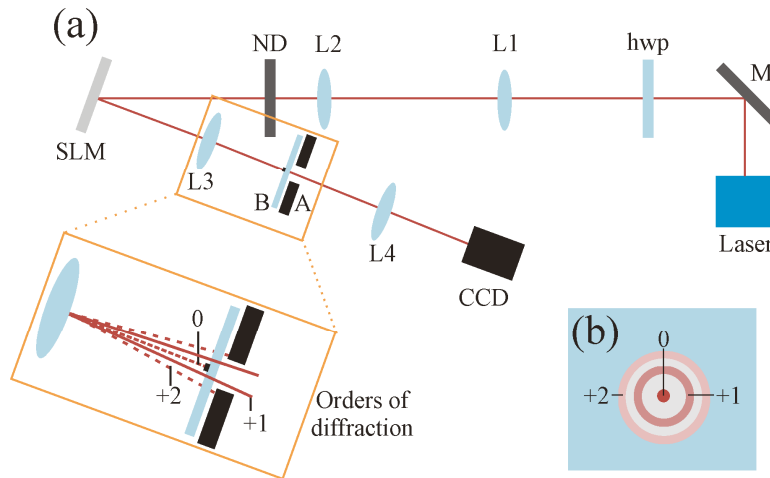


Figure 8.2. The experimental setup is illustrated in image (a). M is a mirror that reflects infrared radiation (Comar 25MX05), hwp is a half waveplate used to control the orientation of the beam's polarization, ND represents the neutral density filters and SLM is the spatial light modulator. Lenses L1, L2, L3 and L4 had focal lengths of 200mm, 250mm, 150mm and 150mm respectively. B represents the spatial filter used to block the zero order diffracted beam, which was an opaque target placed in the centre of a coverslip. CCD is the camera used to record images of the beam and A is the aperture that blocked higher diffracted order beams (+2 and above). The specifications for the SLM (Hamamatsu x10468-03) are given in Table 4.1. Image (b) illustrates the transverse view of the diffracted beams at the Fourier plane of lens L3. Higher diffracted orders exist but are not illustrated.

An aperture was used in conjunction with a spatial filter to select only the first order diffracted beam at the Fourier plane of lens L3. A half waveplate was used to control the polarization direction of the laser beam and select the optimum polarization to direct the maximum possible power into the +1 diffracted order beam. The CCD camera was attached to a rail so that it could be easily translated along the beam's propagation axis.

8.3.2 Spiralling Bessel beams

A spiralling Bessel beam was generated using a hologram displayed on an SLM. Images were taken of the spiralling beam and the corresponding ordinary (non-spiralling) Bessel beam at 20mm intervals along the propagation axis. The images were analysed using a computer program written by the Author that determined the position of the brightest pixel in the central core of the Bessel beam in each image. The difference between the position of the spiralling beam's central core and the ordinary beam's central core was determined at each z position. This corrected for any mismatch between the beam propagation axis and the angle of the rail on which the CCD camera was placed.

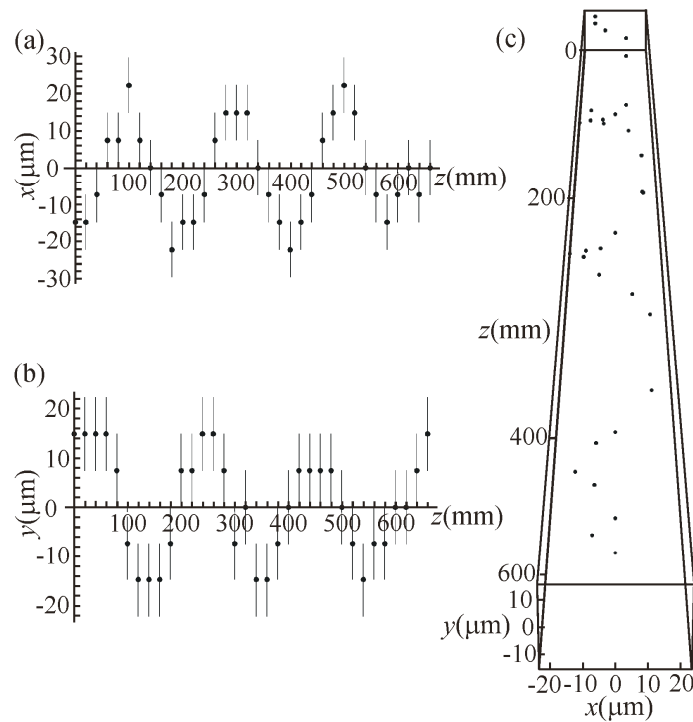


Figure 8.3. SpBB with parameters $\alpha = 0.25^\circ$, $\Delta = 1$ pixel and $\Gamma = 0.08$ pixel⁻¹. Graphs (a) and (b) show the deviation of the beam's central core from the x and y propagation axes respectively. The uncertainty in the plots is ± 1 camera pixel ($\pm 7.4\mu\text{m}$). Graph (c) visualises the 3D propagation. The propagation distance of the beam was $645\text{mm} \pm 20\text{mm}$.

The data taken for some of the beams that were generated is shown in Figures 8.3, 8.4 and 8.5. The size of the central core diameter for all of these beams was $105 \pm 6\mu\text{m}$ (the uncertainty is the random uncertainty taken from the horizontal and vertical core sizes).

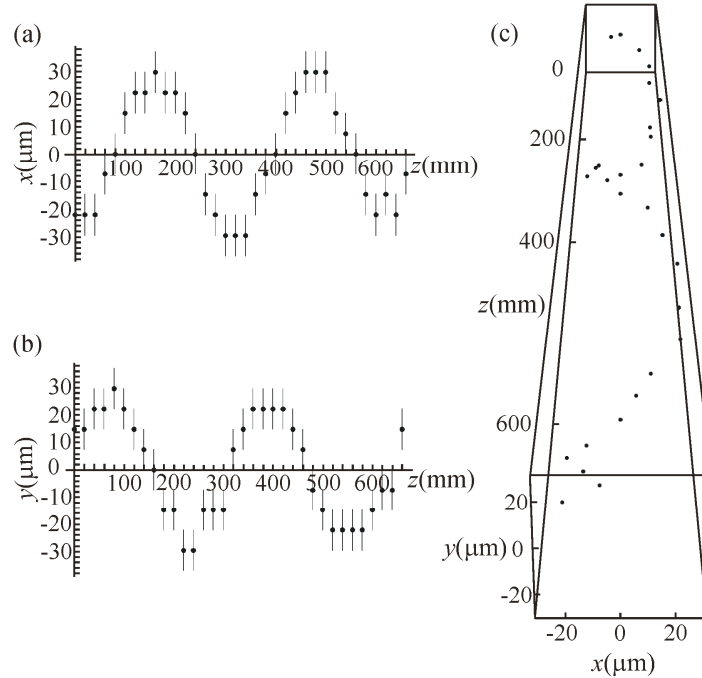


Figure 8.4. SpBB with parameters $\alpha = 0.25^\circ$, $\Delta = 1.5$ pixels and $\Gamma = 0.05 \text{ pixel}^{-1}$. Graphs (a) and (b) show the deviation of the beam's central core from the x and y propagation axes respectively. The uncertainty in the plots is ± 1 camera pixel ($\pm 7.4\mu\text{m}$). Graph (c) visualises the 3D propagation. The propagation distance of this beam was $645\text{mm} \pm 20\text{mm}$.

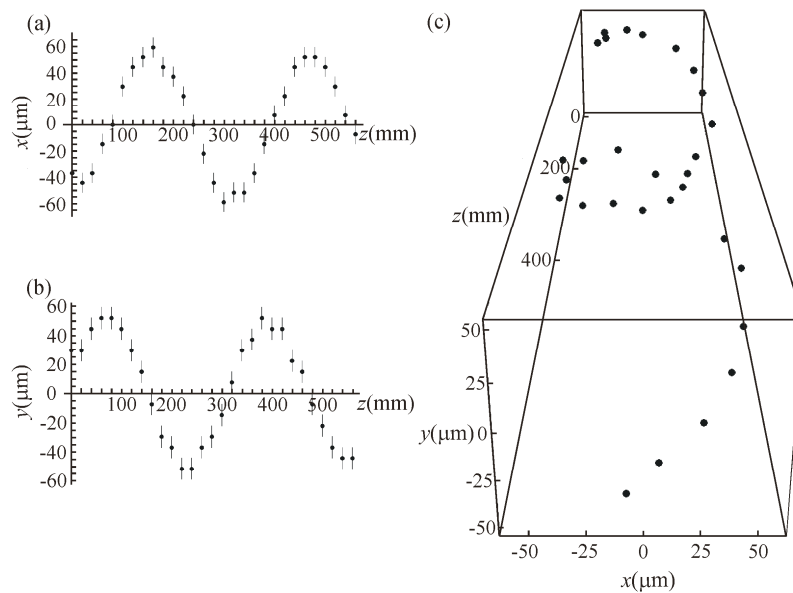


Figure 8.5. SpBB with parameters $\alpha = 0.25^\circ$, $\Delta = 3$ pixels and $\Gamma = 0.05 \text{ pixel}^{-1}$. Graphs (a) and (b) show the deviation of the beam's central core from the x and y propagation axes respectively. The uncertainty in the plots is ± 1 camera pixel ($\pm 7.4\mu\text{m}$). Graph (c) visualises the 3D propagation. The propagation distance of this beam was $560\text{mm} \pm 20\text{mm}$.

The maximum deviation from the optic axis for the beams shown in Figures 8.3 - 8.5 is $60\mu\text{m}$. For many applications, a large deviation from the axis may not be required. However, the aim of this experiment was to show that the central core of a snaking Bessel beam can propagate around obstructions placed on the propagation axis. For this to be possible, it is necessary to produce a beam that deviates from the propagation axis by at least the diameter of the beam's central core. The aim was also to ensure that at least one full oscillation of the beam would be achieved during propagation. The decision was made to reduce the central core size as much as possible and maximize the deviation of the beam's central core from the propagation axis. In order to do this, I had to increase the value of α and make Δ as large as possible. There is a trade off between the values of Δ and Γ . Increasing Δ requires a decrease in Γ otherwise the overall propagation distance of the beam will be reduced.

A program written by Heather Dalgarno and Tomáš Čižmár was used to simulate the spiralling beam. By varying the parameters in the program and studying the simulations, I decided to generate two beams, one with $\alpha = 0.5^\circ$ and the other with $\alpha = 0.6^\circ$. I found that a beam with $\alpha = 0.5^\circ$ had a central core diameter of about $60\mu\text{m}$, and a beam with $\alpha = 0.6^\circ$ had a central core diameter of about $50\mu\text{m}$. The hologram used to generate the beam with $\alpha = 0.6^\circ$ had a grating spacing of just 3 pixels. The use of such a small grating spacing results in more aberrations in the generated beam. However, the generated beam had a good transverse profile after a wavefront correction was applied (see Appendix A). The final chosen beam parameters were $\alpha = 0.6^\circ$, $\Delta = 3$ pixels and $\Gamma = 0.03 \text{ pixel}^{-1}$. These parameters were chosen because the resultant beam deviated from the optic axis by more than the central core diameter, and the beam achieved one full spiral rotation.

Plots of the propagation of the generated beam are shown in Figure 8.6. Images of the beam at intervals along its propagation are shown in Figure 8.7. The position of the centre of the ordinary Bessel beam is indicated by a white cross. The theoretically predicted propagation distance of the beam was $380\text{mm} \pm 10\text{mm}$ (obtained from computer simulations of the beam profile). A simulated image of the beam was produced at 10mm intervals along the propagation axis. Simulated transverse intensity profiles of

the beam were studied, and the end of propagation was taken to be at the z position where the central core was no longer the brightest part of the transverse intensity profile of the beam. The experimental propagation distance achieved was 250mm, and the core size of the beam was $48.5 \pm 1\mu\text{m}$. The experimental propagation distance was less than the theoretically predicted distance because of aberrations in the wavefront.

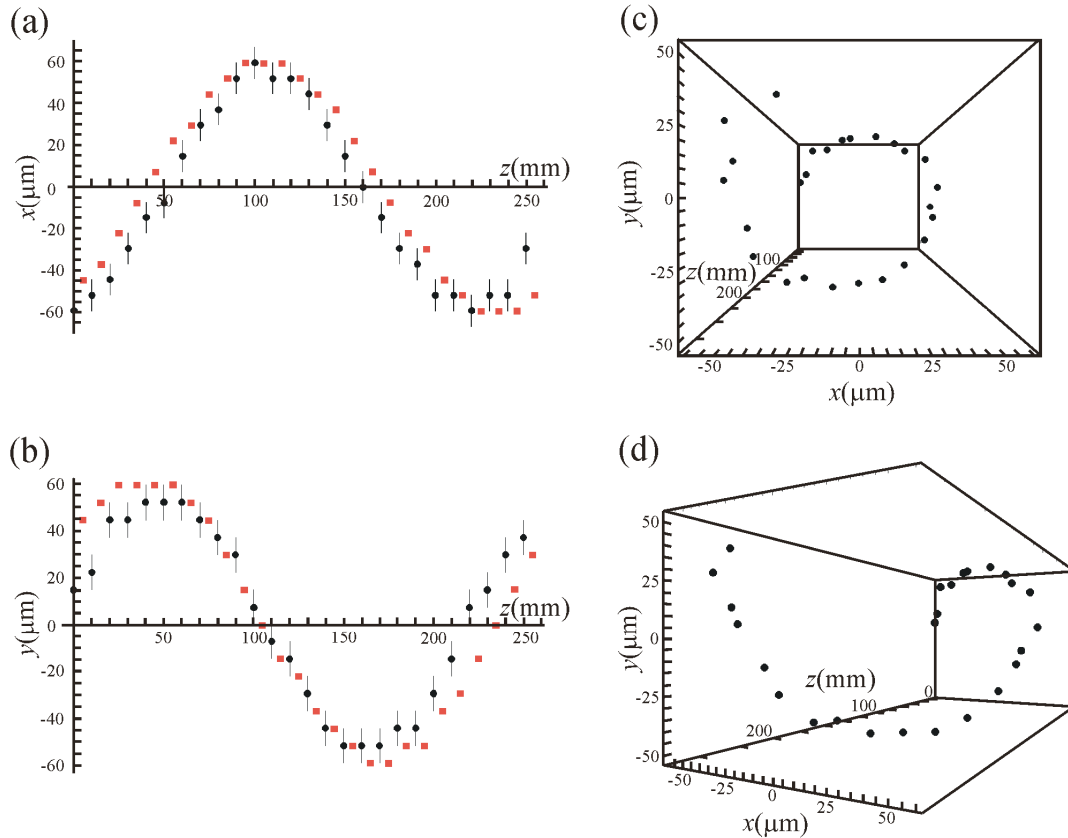


Figure 8.6. The black circles indicate the experimental data and the red squares indicate the theoretically determined points. Plots (a) and (b) show the variation in position of the spiralling beam along the x and y axes as a function of z . Plots (c) and (d) show 3D plots of the beam's propagation from two different viewpoints. The uncertainty in z position was $\pm 10\text{mm}$ and the uncertainty in the x and y position was ± 1 pixel ($\pm 7.4\mu\text{m}$). The theoretical points have been shifted by -25mm to match with the experimental points. This is necessary because of a mismatch between the start position of the theoretical beam and the experimental beam.

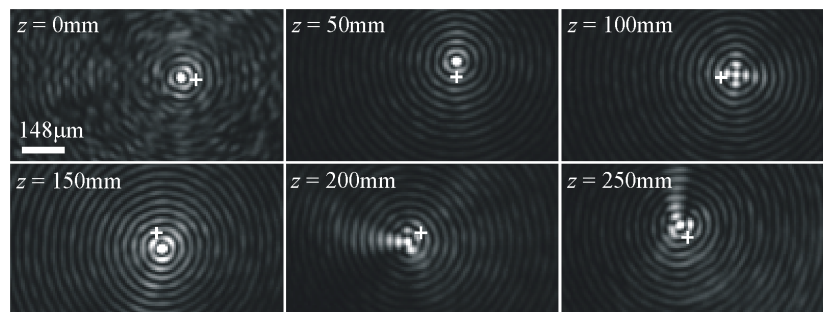


Figure 8.7. Experimental images of the spiralling Bessel beam are shown above. The white cross indicates the position of the ordinary Bessel beam's central core at each z position for reference.

8.3.3 Snaking Bessel beams

In this research, a beam that has an oscillation applied in only one transverse axis is referred to as a snaking Bessel beam. Such a beam was generated using the experimental setup shown in Figure 8.2(a). An objective lens ($\times 10$, N.A. 0.25) was used to image the beam onto the CCD camera, which allowed the imaging of the effect of the obstructions on the transverse beam profile. A hologram that matched the core size and deviation of the snaking beam to those of the spiralling beam presented in Figures 8.6 and 8.7 was displayed on the SLM. Images of the snaking beam and the equivalent ordinary beam were taken at 3mm intervals along the propagation axis. The difference in the position of the central core of the snaking Bessel beam and the central core of the ordinary Bessel beam was determined at each z position and the results were plotted. These plots are shown in Figure 8.8. The snaking beam clearly propagates along a curved path in the y axis but does not deviate from a straight path in the x axis. The maximum deviation from the axis was $60\mu\text{m}$. The core size of the snaking Bessel beam was $49.5 \pm 1\mu\text{m}$ and the propagation distance was $252 \pm 3\text{mm}$. A beam that has a larger deviation than core size has now been successfully generated.

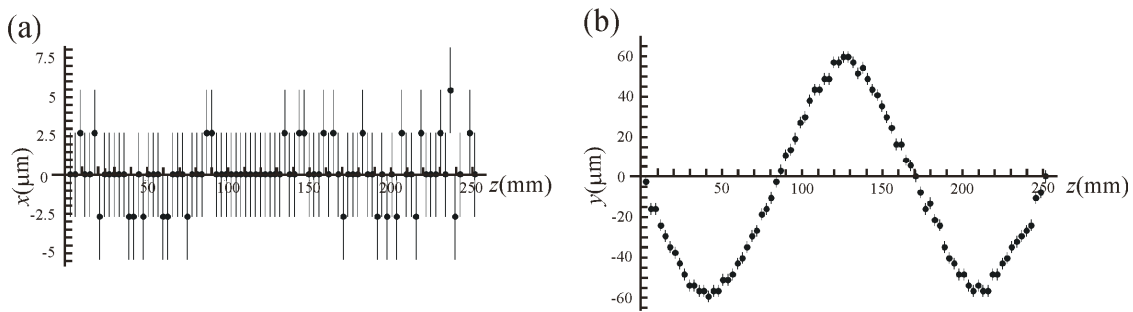


Figure 8.8. The variation of the snaking beam in the x and y axes as a function of z are shown. The uncertainty is ± 1 camera pixel (i.e. $\pm 2.7\mu\text{m}$).

To demonstrate the ability of the snaking Bessel beam to propagate around obstructions, two $50\mu\text{m}$ diameter obstructions were placed in the beam path such that the central core of the ordinary Bessel beam was completely obscured. The obstructions were placed on the propagation axis at $z = 36\text{mm}$ and $z = 123\text{mm}$. Images were taken along the propagation axis of both the ordinary and snaking Bessel beams. The intensity profiles of both beams, with and without the obstructions in place, are shown in Figure 8.9.

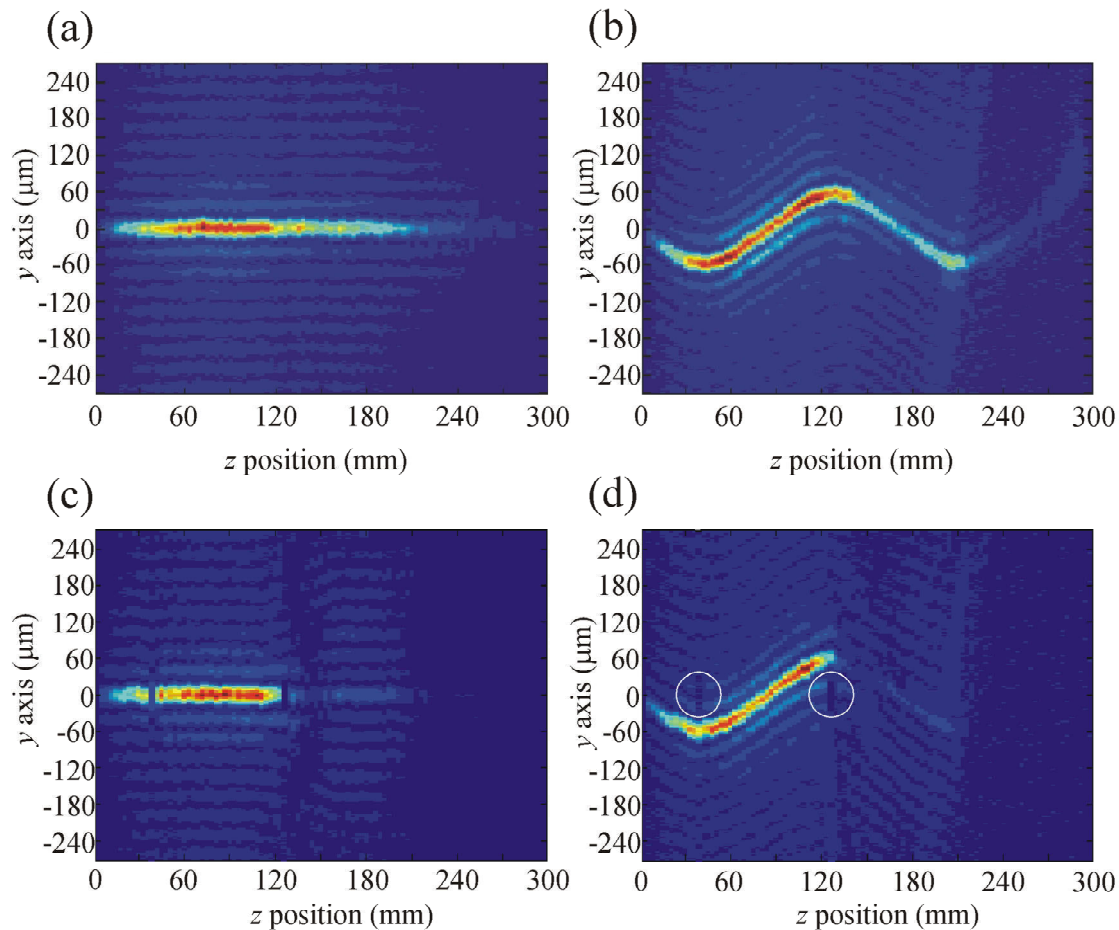


Figure 8.9. Images (a) and (b) show the experimentally determined ordinary and snaking Bessel beam propagations without obstructions respectively. Images (c) and (d) show the experimentally determined intensity profiles of the ordinary and snaking beams when the two obstructions were in place. White circles indicate the position of the two obstructions in image (d) for clarity. Images were taken every 3mm and reconstruction in (c) occurred within 3mm. Therefore, the resolution is too low to determine the reconstruction distance accurately from this image. Please see Figure 8.13 for a more detailed look at the reconstruction of the beam.

Comparing Figures 8.9(a) and (b) with Figures 8.9(c) and (d), it is clear that the propagation distance of the Bessel beams with the obstructions in place is less than when there were no obstructions in place. This is because the obstructions used were surrounded by an opaque area that blocked the outer rings of the Bessel beams. This resulted in a shortened propagation distance of the beam. Images showing how the intensity profiles of the beams were affected by this aperture problem are shown in Figure 8.10. The experiment was repeated using obstructions that were not surrounded by an opaque region. The two new obstructions were manufactured by depositing a $50\mu\text{m}$ nickel-chrome spot onto 1mm thick coverslides using electron beam evaporation. Figure

8.10 also shows images of the beams taken when these ‘non-apertured’ obstructions were in place.

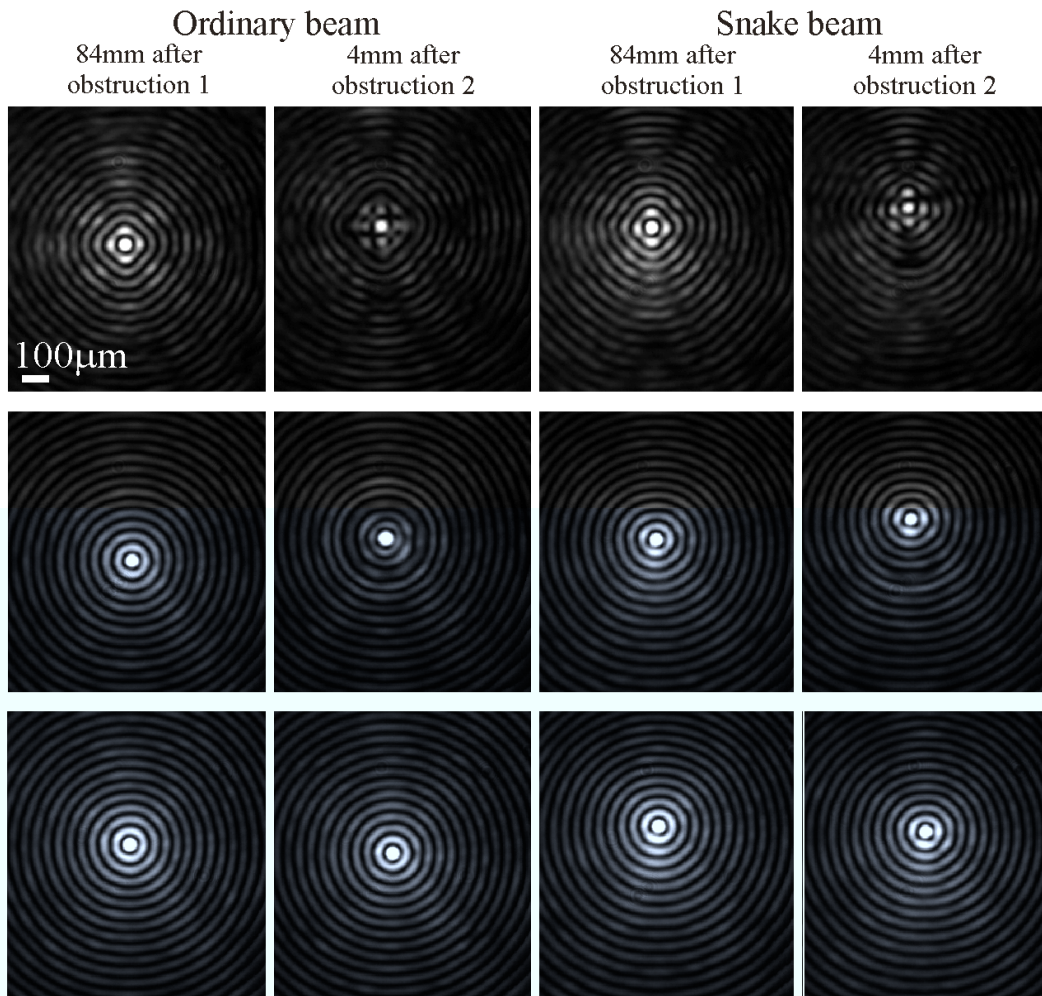


Figure 8.10. The first two columns (left) show the ordinary Bessel beam and the third and fourth columns (right) show the snaking Bessel beam. The top row shows images taken using the original obstructions that were surrounded by an opaque area causing an aperture affect on the profile of the beams. The second row shows images of the beams taken when obstructions were used that did not have an aperture surrounding them. The lower row shows images of the beams when there were no obstructions placed on the propagation axis. In each case, images were taken at a z position of 84mm after obstruction 1 and 4mm after obstruction 2. When the ‘apertured’ obstructions were used, aperture effects became apparent at 84mm beyond obstruction 1 and after propagating only 4mm beyond obstruction 2.

Figure 8.11 shows images of both the ordinary Bessel beam and the snaking Bessel beam with the ‘non-apertured’ obstructions in place and clearly shows that the central core of the snaking beam is not obscured. Figure 8.12 shows the side view intensity profiles of the ordinary beam and snaking beam with the obstructions in place. In the absence of

aperturing, the overall propagation distance of the beams is not affected by the obstructions.

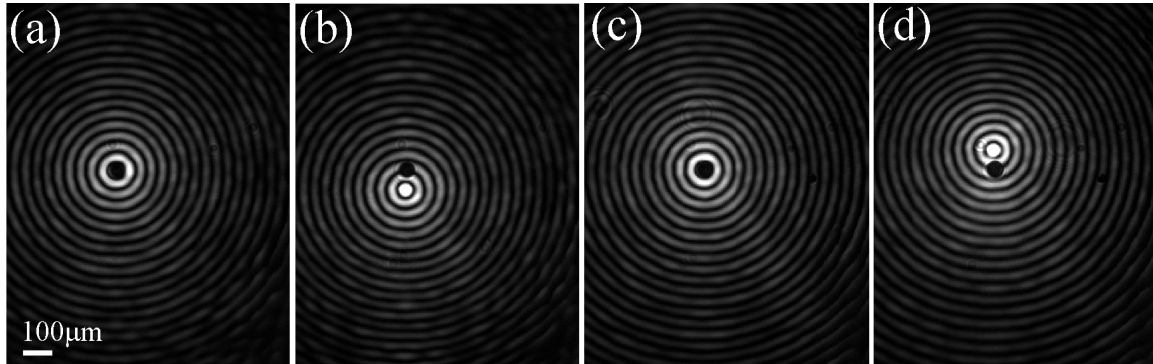


Figure 8.11. Image (a) shows the first obstruction blocking the central core of the ordinary Bessel beam (image taken at $z = 36\text{mm}$). Image (b) shows that the central core of the snaking Bessel beam was not obscured by the first obstruction (image taken at $z = 36\text{mm}$). Images (c) and (d) show the ordinary and snaking beams respectively at the position where the second obstruction was placed ($z = 123\text{mm}$).

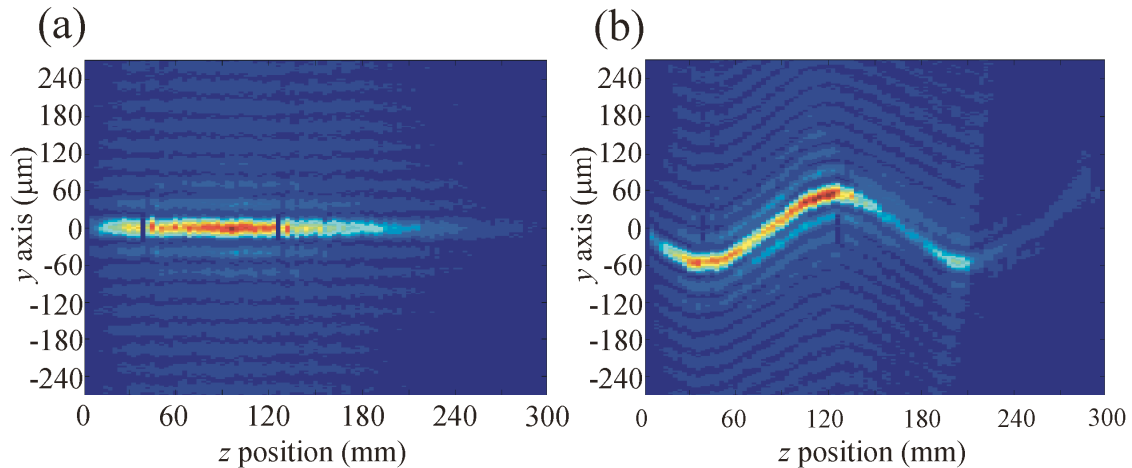


Figure 8.12. The propagation of the ordinary (a) and snaking (b) Bessel beams are shown with two ‘non-apertured’ obstructions placed on the propagation axis. The first obstruction was placed at $z = 36\text{mm}$ and the second was placed at $z = 123\text{mm}$.

When the obstructions were in place, the ordinary Bessel beam reconstructed around them, but the snaking beam was able to propagate around the obstructions unhindered. This demonstrates the ability of the beam to propagate around obstructions placed on the optic axis.

Additionally, images were taken at intervals of $150\mu\text{m}$ after the first obstruction to show the reconstruction of the ordinary Bessel beam in more detail. Figure 8.13 shows the reconstruction of the beam.

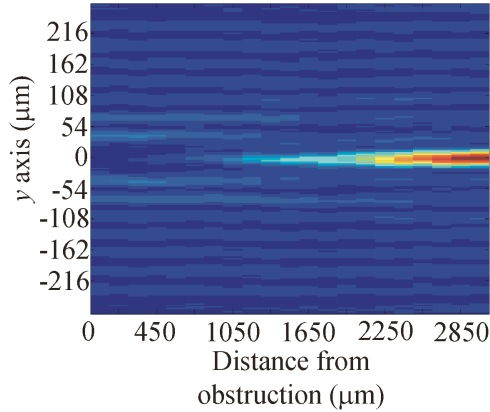


Figure 8.13. The reconstruction of the ordinary Bessel beam after encountering obstruction 1 is shown.

Theoretically, the minimum reconstruction distance, z_{\min} , can be calculated using the equation $z_{\min} \approx r_{obs} / \gamma$, where r_{obs} is the radius of the obstruction placed at the beam centre and γ is the cone angle of the wavevectors. The theoretically predicted propagation distance of the beam was $380\text{mm} \pm 10\text{mm}$ (obtained from computer simulations of the beam profile). Knowing that the beam waist incident on the hologram is approximately $6\text{mm} \pm 1\text{mm}$ (300 pixels), we can calculate the cone angle of the wavevectors using the equation $z_{\max} \approx w_{inc} / \gamma$. This gives $\gamma = 0.016\text{ radians} \pm 0.003\text{ radians}$. Since the radius of the obstruction is $25\mu\text{m} \pm 2\mu\text{m}$, the calculated minimum reconstruction distance of the beam is $1500\mu\text{m} \pm 300\mu\text{m}$. Although it is difficult to tell the exact reconstruction distance from Figure 8.13, it appears that the reconstruction distance is slightly larger than the calculated value at around $2500\mu\text{m}$. The discrepancy might be explained if the beam incident on the hologram was not well collimated. If the beam was diverging when it was incident on the hologram, the value of γ would be lower than the above calculated value and the reconstruction distance would be larger than the above calculated value.

8.4 Discussion

It has been shown that spiralling and snaking Bessel beams can be generated and that their properties can be varied by adjusting the parameters used to produce the holograms. Beams have been generated that can complete multiple spirals within the range of propagation. However, the deviation of these beams from the optic axis was small

compared to the diameter of the central core. Since the aim in this chapter was to generate a beam that could propagate around obstructions placed on the optic axis, a beam was required that deviated from the optic axis by at least the diameter of the beam's central core. I was able to generate a beam with the aforementioned qualities by adjusting the beam parameters. The core size of the beam was reduced by increasing the value of α . The deviation of the beam from the propagation axis was increased by increasing the value of Δ , and consequently the value of Γ was reduced.

Decreasing the core size of the beam resulted in a reduction in the grating spacing of the hologram. The limitation on the parameters of the beams produced arises from the resolution of the SLM. The beam shown in Figure 8.6 was generated using a hologram with a grating spacing of just three SLM pixels. Aberrations in the beam increase when using holograms with such fine detail. This is because the liquid crystals in the SLM struggle to align themselves appropriately so that a complete 0 to 2π phase shift can occur over such a short range. Additionally, the phase change from 0 to 2π is not smooth when it occurs over very few pixels. For three pixels, the first pixel must have a phase of 0 , the second pixel must have a phase of π and the third pixel must have a phase of 2π .

I then generated a snaking Bessel beam with similar parameters to the spiralling Bessel beam presented in Figure 8.6. Obstructions with a similar diameter to the diameter of the snaking beam's central core were manufactured. The obstructions were then placed on the propagation axis, and it was shown that the central core of the snaking Bessel beam could propagate around the obstructions.

Some of the experimental images in Figure 8.7 show the beam's transverse intensity profile with the first intensity ring broken into four bright spots. This is most likely due to aberrations in the optical system. A wavefront correction was applied to the hologram to improve the beam profile but it was not able to prevent this effect. Wavefront correction is explained in Appendix A. Additionally, it is thought that the mismatch between the experimental and theoretical propagation distances was due to wavefront aberrations, which is not taken into account in the theoretical model.

The intensity of the snaking Bessel beam along the propagation axis can be seen in Figures 8.9 and 8.12. During the first half of the beam's propagation, the central core has a high intensity. However, during the second half of the beam's propagation, the central core has a relatively low intensity. I suggest that this is due to wavefront aberrations and the finite aperture (and finite energy) of the system.

The work presented in this chapter has been accepted for publication in the *Journal of Optics*.⁷

Acknowledgements

The theoretical background, hologram generating program and beam simulation program were produced by Heather Dalgarno and Tomáš Čižmár. The wavefront correction software was designed by Tomáš Čižmár. Rob Marchington manufactured the 'non-apertured' 50 μ m obstructions. All of the experimental work and data analysis was carried out by the Author.

References

1. Paterson, C. & Smith, R. Helicon waves: Propagation-invariant waves in a rotating coordinate system. *Optics Communications* **124**, 131-140 (1996).
2. Alonzo, C. A., Rodrigo, P. J. & Glückstad, J. Helico-conical optical beams: a product of helical and conical phase fronts. *Opt. Express* **13**, 1749-1760 (2005).
3. Jarutis, V., Matijosius, A., Di Trapani, P. & Piskarskas, A. Spiraling zero-order Bessel beam. *Optics Letters* **34**, 2129-2131 (2009).
4. Lee, S.-H., Roichman, Y. & Grier, D. G. Optical solenoid beams. *Opt. Express* **18**, 6988-6993 (2010).
5. Matijošius, A., Jarutis, V. & Piskarskas, A. Generation and control of the spiraling zero-order Bessel beam. *Opt. Express* **18**, 8767-8771 (2010).
6. Goodman, J. W. in *Introduction to Fourier Optics* 55-61 (McGraw-hill, 1996).
7. Morris, J. E. et al. Realization of curved Bessel beams: propagation around obstructions. *Journal of Optics* (accepted 2010).

Chapter 9

Summary and outlook

9.1 Summary and outlook

In Chapter 5, a traditional optical tweezers experimental setup was adapted to facilitate the use of a supercontinuum source. The use of a broad bandwidth source, and not a narrowband source, for optical manipulation requires a different approach to achieve illumination of the sample. The spectrum of the supercontinuum beam was filtered and the sample was illuminated with an LED emitting at a wavelength that was filtered out of the supercontinuum beam. An interference filter that transmitted only the wavelength of the illumination light was placed before the CCD camera. This allowed the trapped object to be viewed via the CCD camera. The supercontinuum beam was focused into a sample of silica spheres. The three dimensional optical confinement of silica spheres of 780nm, 970nm and 1.28 μ m diameter was achieved. Trap stiffness values were measured as a function of optical power in the trap. For all three sphere sizes, the axial trap stiffness values were significantly lower than the transverse values. I found that whilst the optical forces in the transverse plane of a broadband optical trap are comparable to those in a narrowband optical trap,¹ the axial forces for the broadband optical trap are significantly weaker due to chromatic aberration. Indeed, when optically manipulating polymer spheres, only confinement in two dimensions was achieved with axial confinement obtained using the top of the sample chamber.

Next, holographic techniques were used to produce multiple broadband optical trap sites. A grating was added to the holograms in order to spatially separate the different order beams produced. However, the grating caused lateral chromatic dispersion due to the wavelength dependent diffraction angle. Dispersion compensation was achieved by imaging the hologram onto a prism of opposite dispersion. A maximum of two dispersion compensated optical trap sites could be produced in this way. Producing a larger number of dispersion compensated traps would require a different approach because each beam emerging from the hologram has different dispersion characteristics. The total trapping power of both traps was 24mW, although this power was not divided evenly between the trap sites because of the efficiency of the hologram. The upper trap site had 1.1 times more power than the lower trap site. Additionally, the upper trap site was better compensated for dispersion than the lower trap site as seen in Figure 5.10. A polymer microsphere with a diameter of $2\mu\text{m}$ was confined in each trap site and trap stiffness values were measured. The upper trap had similar trap stiffness values for the x and y axes. For the less well dispersion compensated trap, the measured trap stiffness values were different for the x and y axes.

Next, I investigated an alternative method to generate multiple broadband optical trap sites. A supercontinuum beam was incident on an array of parabolic micromirrors. The reflected light produced an optical trap at the focal point of each mirror. The focal length of a parabolic mirror is independent of wavelength, so dispersion compensation techniques were not required. I was able to confine polymer microspheres of diameters ranging from $1\mu\text{m}$ to $10\mu\text{m}$ in three dimensions in the optical trap sites. This is known to be the case because the spheres were tweezed away from the edges of the sample chamber.

The use of a broadband source for optical manipulation opens up the possibility for the development of optical spectroscopy applications. The use of a computer generated hologram to produce multiple trap sites results in lateral chromatic dispersion. However, the use of a different method to compensate the dispersion produced by a hologram grating may result in the ability to generate more broadband optical trap sites. If an SLM

with a grating hologram is used to generate multiple broadband trap sites, it could be possible to use a second SLM to display a grating hologram with opposite dispersion. The second SLM could then be used to compensate the dispersion produced at the first SLM to form a large number of broadband ‘white light’ optical traps. Mariyenko *et al.*² have demonstrated that this technique works for compensating the dispersion of a broadband optical vortex.

Additionally, more work could be carried out using the micromirror array. The use of a micromirror array to generate multiple trap sites does produce a large number of broadband optical traps. An experimental setup was suggested to allow a characterisation of the optical trapping forces. Using a new array of parabolic micromirrors, the experimental method described at the end of Chapter 5 might allow trap stiffness values to be obtained. It would also be interesting to work towards developing a spectroscopic lab-on-a-chip device using the micromirror array. Since the array is already designed to be part of a microfluidic device, it may be possible to extend this technology to obtain spectroscopic measurements of the trapped objects.

In Chapter 6, the use of holographic techniques to generate a ‘white light’ optical vortex was described. I was able to optically trap microspheres in the high intensity ring of the optical vortex. The rotation of a single microsphere trapped in the vortex was not observed. This is because the azimuthal intensity of the optical vortex was not uniform. However, a group of three microspheres could be trapped and rotated in the vortex. Therefore, the transfer of orbital angular momentum from the ‘white light’ vortex to a group of three polymer microspheres has been demonstrated. Rotation rates for the three spheres were also determined for optical vortices with $p = 0$ and $l = 2, 3, 4$ and 5 . Although the rotation rate did not vary greatly with l value, the maximum rotation rate was 3.7Hz and was achieved using the vortex with $l = 4$ and a trapping power of 15mW. Further work relating to the optical vortex could involve an investigation into the effect of low spatial coherence on the transfer of orbital angular momentum to trapped microspheres.

After the optical vortex experiment, the investigation into novel beams continued. The supercontinuum source provided a unique opportunity to investigate the effect of wavelength and spatial coherence on the properties of the optical Airy beam using a single laser source. Holographic techniques were employed to generate the Airy beam. Interference filters were placed in the supercontinuum beam to investigate the effect of wavelength on the parabolic propagation, lobe spacing and aperture coefficient of the Airy beam. The interference filters were of varying optical quality, which allowed for an investigation into the effect of spatial coherence on the beam's properties. It was found that the parabolic propagation was steeper for beams generated using a beam with a shorter wavelength. The spacing between the lobes in the Airy beam's transverse intensity profile was less when the lasing wavelength was shorter. The wavelength did not affect the aperture coefficient of the beam. However, the spatial coherence of the optical beam affected only the aperture coefficient. A beam with lower spatial coherence had a higher aperture coefficient and therefore a shorter propagation distance. Additionally, using the prism dispersion compensation method, the first ever 'white light' Airy beam was generated. This work is presented in Chapter 7.

It has been demonstrated that the Airy beam is able to guide objects along a parabolic trajectory.³ Future experiments could include an investigation into the optical sorting applications of this beam. For spheres with different physical properties placed in an Airy beam, the force acting on each sphere varies. As a result, some spheres will propagate further along the parabolic trajectory than others thus allowing the optical sorting of objects. The varying trajectories of the different wavelength components of the 'white light' Airy beam might also be utilised for optical sorting applications. The optical forces acting on metallic nanoparticles depends on wavelength, so metal nanoparticles with different properties might be optically guided in the different wavelength components of the 'white light' Airy beam.

The parabolic propagation of the Airy beam inspired an investigation into other beams with non-straight propagation paths. In Chapter 8, Bessel beams that propagate along spiralling and snaking paths were generated. The parameters of these beams could be

altered to adjust the radius and pitch of the spirals/oscillations as well as the size of the Bessel beam's central core. It was also demonstrated that the central core of a snaking Bessel beam can propagate around obstructions placed on the optic axis. These obstructions were shown to obscure the central core of an ordinary Bessel beam. The next step to develop the work on the spiralling Bessel beam would be to optically guide objects using the central core of the beam. This may be beneficial for guiding objects around obstructions in microfluidic devices.

References

1. Ghislain, L. P., Switz, N. A. & Webb, W. W. Measurement of small forces using an optical trap. *Review of Scientific Instruments* **65**, 2762-2768 (1994).
2. Mariyenko, I. G., Strohaber, J. & Uiterwaal, C. Creation of optical vortices in femtosecond pulses. *Opt. Express* **13**, 7599-7608 (2005).
3. Baumgartl, J., Mazilu, M. & Dholakia, K. Optically mediated particle clearing using Airy wavepackets. *Nat Photon* **2**, 675-678 (2008).

Appendix A

A.1 Wavefront correction

To correct for aberrations in the wavefront of a beam, a wavefront correction phase hologram can be added to the beam shaping hologram. In this thesis, wavefront correction is used to improve the transverse intensity profiles of the novel beams. The original hologram that was designed to generate the novel beam was displayed on the SLM and the resultant beam profile was viewed using a CCD camera. A Labview program was then used to add the wavefront correction phase mask to the novel beam phase mask. Zernike polynomials are a basis set which are orthogonal over a unit circle, and they describe wavefront aberrations such as astigmatism and coma. Using the image of the beam from the CCD camera to observe the improvement in the intensity profile of the beam, the wavefront correction was applied in real time using a Labview program written by Tomáš Čížmár. A systematic approach was necessary to ensure that the best wavefront correction was found. Some of the most well known aberrations that occur in optics and their corresponding Zernike polynomials are listed below,¹ where r and ϕ are the cylindrical co-ordinates. Figure A.1 shows examples of some of the corresponding phase profiles.

Tip:	$\psi(r) = 2r \cos(\phi)$
Tilt:	$\psi(r) = 2r \sin(\phi)$
Defocus:	$\psi(r) = 2r^2 - 1$
Astigmatism:	$\psi(r) = r^2 \cos(2\phi)$
Astigmatism:	$\psi(r) = r^2 \sin(2\phi)$
Coma:	$\psi(r) = (3r^2 - 2)r \sin(\phi)$
Coma:	$\psi(r) = (3r^2 - 2)r \cos(\phi)$
Spherical aberration:	$\psi(r) = 6r^4 - 6r^2 + 1$
Trefoil:	$\psi(r) = r^3 \cos(3\phi)$
Trefoil:	$\psi(r) = r^3 \sin(3\phi)$

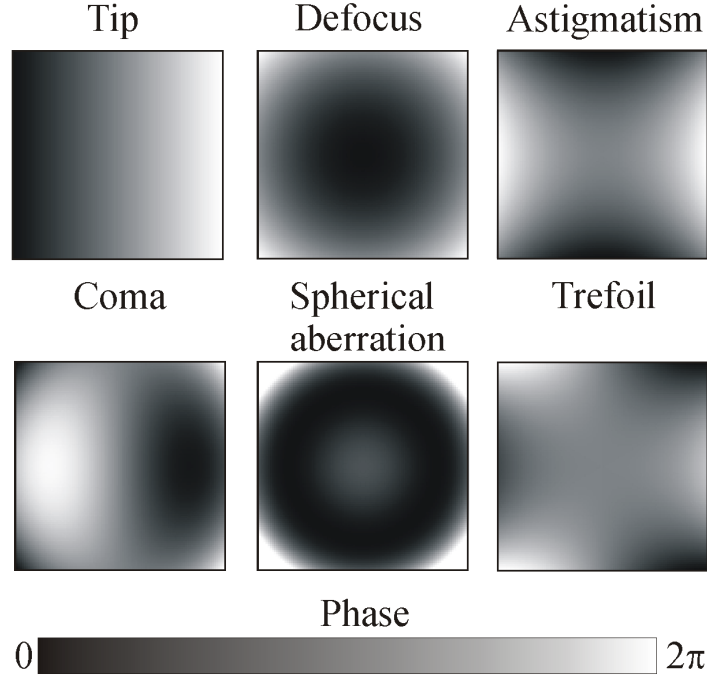


Figure A.1. Examples are shown of some of the wavefront corrections that can be applied to a computer generated hologram using Zernike polynomials.

An example is now given to demonstrate the addition of the Zernike polynomial for astigmatism to a vortex hologram. The phase hologram that produces an optical vortex with $l = 3$ and $p = 0$ is

$$\psi(r) = \text{mod}\left(l\phi - \frac{2\pi}{\Lambda} r \cos\phi, 2\pi\right), \quad (\text{A.1})$$

where r and ϕ are the cylindrical co-ordinates, l is the azimuthal phase and Λ is the grating spacing. The addition of the Zernike polynomials for astigmatism yields

$$\psi(r) = \text{mod}\left(l\phi - \frac{2\pi}{\Lambda} r \cos\phi + c_1 r^2 \cos(2\phi) + c_2 r^2 \sin(2\phi), 2\pi\right), \quad (\text{A.2})$$

where c_1 and c_2 are amplitude coefficients. Equation A.3 gives the scalar field of a beam after encountering a hologram that imposes a phase of $\psi(r)$ on an incident beam.

$$u(r) = u_0(r) \exp(i\psi(r)), \quad (\text{A.3})$$

where the scalar field of the beam incident on the hologram is $u_0(r)$.

Wavefront aberrations have a detrimental effect on the beam properties and the transverse intensity beam profile. Therefore, it can be very beneficial to apply a wavefront correction. Wright *et al.*² demonstrated the use of a spatial light modulator for wavefront correction. Whereas the wavefront correction process used in this research was a manual technique, Wright *et al.* used a feedback loop to automate the process.

References

1. Love, G. D. Wave-front correction and production of Zernike modes with a liquid-crystal spatial light modulator. *Appl. Opt.* **36**, 1517-1520 (1997).
2. Wright, A. J. et al. Dynamic closed-loop system for focus tracking using a spatial light modulator and a deformable membrane mirror. *Opt. Express* **14**, 222-228 (2006).

Appendix B

B.1 Laguerre Gaussian beam propagation

Laguerre Gaussian beams are a family of solutions to the paraxial equation and form a complete orthogonal set. Using the first order approximation paraxial equation¹ we look at the propagation of a Laguerre Gaussian beam. The numerical finite elements method is a way of solving difficult partial differential equations by breaking the problem up into smaller, more manageable elements and tying all the results together. In our case, we split the surface of the trapped object into small sections and determine an equation for each section. This leads to a set of simultaneous equations that can be solved to determine the scattering field around the trapped object. The Maxwell stress tensor is then used to describe the transfer of linear and angular momentum to the spheres from the Laguerre Gaussian beam.

The complex solution of the paraxial equation is given below. It describes the amplitude and phase of the electromagnetic wave at any position in space.

$$u'_{p=0}(x, y, z) = \frac{u_0}{(z + iz_r)^{l+1}} (x + iy)^l \exp\left(-in_0k_0 \frac{x^2 + y^2}{2(z + iz_r)}\right), \quad (\text{B.1})$$

where u_0 is the amplitude coefficient, n_0 and k_0 are the refractive index of the surroundings and the vacuum wavevector respectively. The Rayleigh range z_r is given by $z_r = n_0k_0w_0^2/2$, where w_0 is the beam waist. Equation B.1 describes the longitudinal shape and decay of the beam as well as describing the Gouy phase shift.

The electric and magnetic fields, \mathbf{E} and \mathbf{H} , can be given in terms of the vector potential for a beam of a single wavelength \mathbf{A}_ω , Z_0 is the vacuum impedance of a beam polarized linearly along the x axis and \mathbf{e}_x is the x axis unit vector.

$$\mathbf{A}_\omega = \begin{pmatrix} \mathbf{e}_x \\ 0 \\ 0 \end{pmatrix} u'_{p=0}(x, y, z) \exp(-in_0k_0z) \quad (\text{B.2})$$

$$\mathbf{E} = \frac{1}{n_0^2 k_0^2} \nabla(\nabla \cdot \mathbf{A}_\omega) + \mathbf{A}_\omega, \quad (\text{B.3})$$

$$\mathbf{H} = \frac{i}{Z_0 k_0} \nabla \times \mathbf{A}_\omega. \quad (\text{B.4})$$

We next find the amplitude coefficient u_0 by first determining the total power P_0 of the beam and then using this to calculate u_0 . We can determine the total power of the beam by integrating the time averaged Poynting vector, $\langle \mathbf{S} \rangle$, over x and y , where $\langle \mathbf{S} \rangle = \text{Re}(\mathbf{E} \times \mathbf{H}^*)/2$, the asterisk indicates the complex conjugate and $\langle \rangle$ denotes the time average. The resulting equation for P_0 is then rearranged into Equation B.5 which gives the amplitude coefficient.

$$u_0 = \left(\frac{p_0 Z}{\pi w_0^2} \frac{(-1)^{l+1} s^{2-2l} z_r^2}{(1+s^2(l+1)(ls^2+2s^2-2))! 2^{l-2}} \right)^{\frac{1}{2}}, \quad (\text{B.5})$$

where the Gaussian order parameter is s and is given by $s = \frac{1}{n_0 k_0 w_0}$ and Z is the wave impedance.

In order to extend this to a supercontinuum source, we need to account for all of the wavelengths present in the source. We can do this by summing over all the spectral components in the beam. The spectral amplitude of the supercontinuum is denoted by $G(\omega)$. We then obtain the following vector potential integrated over the supercontinuum spectrum

$$\mathbf{A}_T = \int d\omega G(\omega) \begin{pmatrix} \mathbf{e}_x \\ 0 \\ 0 \end{pmatrix} u_{p=0}^l(x, y, z) \exp(-in_0 k_0 z) \exp(i\omega t). \quad (\text{B.6})$$

We now have the information we need to look at the forces acting on a sphere trapped in a supercontinuum laser beam. The electromagnetic force density describes the force exerted per unit volume on the trapped sphere by the EM field. We can find the forces acting on the sphere from the field by integrating the EM force density over the volume of the trapped sphere. We need to then average this over the pulse duration. The EM force density depends on the forces arising from the EM momentum density and the

divergence of the Maxwell stress tensor (which gives the momentum influx). The electromagnetic force density, f_i , the electromagnetic momentum density, g_i , and the Maxwell stress tensor^{2,3}, T_{ij} , are given below respectively.

$$f_i = -\frac{\partial}{\partial t} g_i - \frac{\partial}{\partial x_j} T_{ij} \quad (\text{B.7})$$

$$g_i = q_{ijk} D_j B_k^*, \quad (\text{B.8})$$

$$T_{ij} = E_i D_j^* + H_i B_j^* - \frac{1}{2} (E_k D_k^* + H_k B_k^*). \quad (\text{B.9})$$

where we sum over repeating indices. The electric field, electric displacement, magnetic field and magnetic flux are denoted by E_i , D_i , H_i and B_i respectively, where $D_i = \epsilon_r \epsilon_0 E_i$ and $B_i = \mu_r \mu_0 H_i$. Also ϵ_r is the dielectric constant, μ_r is the relative permeability, ϵ_0 is the permittivity of free space, μ_0 is the permeability of free space and q_{ijk} is the Levi-Civita anti-symmetric tensor.

We evaluate an integral on a closed surface around the trapped sphere. The normal surface vector is denoted by $n_j ds$, where $n_j ds$ has the magnitude of the surface area. We average over the pulse duration, Δt , to determine the total optical force on the sphere (see Equation B.10).

$$\langle F_i \rangle = \frac{1}{\Delta t} \iint f_i dV_{vol} dt = \frac{1}{\Delta t} \iint T_{ij} ds_j dt. \quad (\text{B.10})$$

Decomposing the pulse into a superposition of many monochromatic waves, the total average force can be calculated as follows

$$\langle F_i \rangle = \iiint |G(\omega)|^2 \tilde{T}_{ij} n_j ds d\omega, \quad (\text{B.11})$$

where the Maxwell stress tensor for each spectral component, \tilde{T}_{ij} (the tilda denotes the Fourier transform) is given by

$$\tilde{T}_{ij} = \tilde{E}_i \tilde{D}_j^* + \tilde{H}_i \tilde{B}_j^* - \frac{1}{2} (\tilde{E}_k \tilde{D}_k^* + \tilde{H}_k \tilde{B}_k^*). \quad (\text{B.12})$$

The torque acting on the trapped objects can be similarly determined by

$$\langle N_i \rangle = \iint |G(\omega)|^2 q_{ijk} x_j \hat{T}_{kl} n_l ds d\omega. \quad (\text{B.13})$$

The Levi-Civita anti-symmetric tensor is given by q_{ijk} .

B.2 Torques acting on microspheres in a Laguerre Gaussian beam

Equation B.13 is used to calculate the transfer of orbital angular momentum to a group of spheres trapped in an LG beam. The experiment used an ensemble of three polymer spheres of $1\mu\text{m}$ diameter. We consider that the spheres are rotating around the centre of gravity of the group of spheres. For a group of touching spheres rotating together, we need to use a multi-pole expansion of the flow velocity in a series of spherical harmonics.⁴ The drag torque due to the surrounding fluid is $T = -16\pi^2\eta a^3\Omega$ for a single sphere, where Ω is the sphere's rotation rate. The finite elements method is used to solve the incompressible Navier-stokes equations numerically. The drag coefficient of the three spheres rotating as a group is $-T/\Omega = 9.4 \times 10^{-20} \text{ NHz}^{-1}\text{m}$. This equation gives the same value that would be determined if only one sphere of diameter $1.77\mu\text{m}$ was experiencing the drag due to rotation.

To take into account the wall effects, the Navier Stokes equations for the moving spheres and the wall were solved and the force acting on the spheres for different distances to the wall were calculated. Taking the wall effects into account increases the drag coefficient by 5% for a distance of 500nm and by 20% for 100nm distance. There is also a centripetal force pulling the spheres towards the beam centre. This is what caused the three spheres to join together and rotate as one group. The theoretical rotation rate of the spheres was determined using the information about the torque and drag experienced by the group of spheres. Figure B.1 shows the calculated rotation rates per unit power for the three spheres rotating together as a function of wavelength. Also shown is the centripetal force per unit power. The red line shows the value determined in each case using the weighted spectrum from the supercontinuum source.

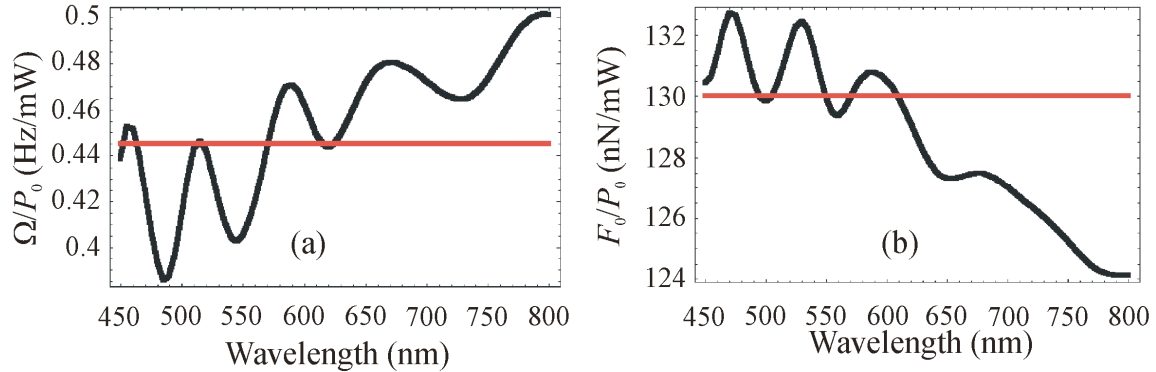


Figure B.1. (a) shown is the calculated rotation rates per incident power for three polymer spheres rotating together as a result of OAM transfer from the supercontinuum LG beam, $l = 3$, $p = 0$ and the beam waist $w_0 = 640 \text{ nm}$. The red line represents the value calculated from the weighted SC spectrum. (b) shows the centripetal force per incident power acting on the spheres. The red line again represents the value determined using the supercontinuum weighted spectrum.

The rotation rate per unit power for the three spheres in our setup is theoretically predicted to be 0.44 Hz/mW . The modelling of forces of a supercontinuum Laguerre Gaussian beam on a trapped sphere was carried out by Michael Mazilu.

References

1. Barton, J. P. & Alexander, D. R. Fifth-order corrected electromagnetic field components for a fundamental Gaussian beam. *Journal of Applied Physics* **66**, 2800-2802 (1989).
2. Jackson, J. D. *Classical electrodynamics* (Wiley, 1999).
3. Pfeifer, R. N. C., Nieminen, T. A., Heckenberg, N. R. & Rubinsztein-Dunlop, H. Colloquium: Momentum of an electromagnetic wave in dielectric media. *Reviews of Modern Physics* **79**, 1197-1216 (2007).
4. Filippov, A. V. Drag and torque on clusters of n arbitrary spheres at low Reynolds number. *Journal of Colloid and Interface Science* **229**, 184-195 (2000).

Appendix C

C.1 Coherent Airy beam propagation

The equivalence of the paraxial wave equation and the Schrödinger equation is what made the realization of the optical Airy beam possible. The optical Airy beam has a finite ‘non-diffracting’ propagation distance and a finite number of lobes. The ‘perfect’ Airy beam is only theoretical and has infinite energy and therefore an infinite non-diffracting propagation distance. The parameter that differentiates the two beams is called the aperture coefficient. It is the finite energy of the real Airy beam that results in its finite properties. The paraxial wave equation is shown below where $k = 2\pi n/\lambda$ is the wavevector, z is the propagation axis co-ordinate and $u_0(x, y, z)$ is the scalar field with a carrier plane wave of the form $\exp(i(\omega t - kz))$.

$$\left(\frac{\partial^2}{\partial x^2} + \frac{\partial^2}{\partial y^2} - 2ik \frac{\partial}{\partial z} \right) u_0(x, y, z) = 0. \quad (\text{C.1})$$

The Lorenz gauge conditions use the magnetic vector potential, \mathbf{A} , to determine the electric and magnetic fields, \mathbf{E} and \mathbf{H} respectively, associated with $u_0(x, y, z)$. The Lorenz gauge conditions are given in Equations C.3 and C.4.

$$\mathbf{A} = u_0(x, y, z) \exp(-ikz) \hat{\mathbf{x}}, \quad (\text{C.2})$$

$$\mathbf{E} = -ick\mathbf{A} - \frac{ic}{k} \nabla(\nabla \cdot \mathbf{A}), \quad (\text{C.3})$$

$$\mathbf{H} = \frac{1}{\mu_0} \nabla \times \mathbf{A}. \quad (\text{C.4})$$

To solve Equation C.1 we can separate the variables to find $u_x(x, z)$ and $u_y(x, z)$ from the following equations:

$$0 = -2ik \frac{\partial}{\partial z} u_x + \frac{\partial^2}{\partial x^2} u_x, \quad (\text{C.5})$$

$$0 = -2ik \frac{\partial}{\partial z} u_y + \frac{\partial^2}{\partial y^2} u_y, \quad (\text{C.6})$$

where

$$u_0(x, y, z) = u_x(x, z) u_y(y, z). \quad (\text{C.7})$$

When $z = b_0 x^2$ denotes the parabola of propagation, the scalar field at $z = 0$ is

$$u_x(x, z = 0) = Ai\left(\frac{x}{x_0}\right) \exp\left(\frac{a_0 x}{x_0}\right), \quad (\text{C.8})$$

where Ai is the Airy function, x_0 is the characteristic length of the beam and a_0 is the aperture coefficient. The scalar field in the y direction takes the same form as the equation above but x is replaced with y . The full scalar field is then the multiplication of u_x and u_y , see Equation C.7.

In order to determine the SLM hologram for the 2D Airy beam, we can take the Fourier transform of Equation C.8 to determine the field that needs to be present at the SLM plane. Passing this field through a lens to Fourier transform it again will produce the Airy beam. The field required in the SLM plane is therefore

$$\hat{u}_x(k_x, z = z_{SLM}) = x_0 \exp(-a_0 x_0^2 k_x^2) \exp\left(\frac{i}{3}(x_0^3 k_x^3 - 3a_0^2 x_0 k_x - ia_0^3)\right). \quad (\text{C.9})$$

This field is a Gaussian beam with a cubic phase shift imposed upon it by the hologram. The first exponential term describes the Gaussian and the second exponential term describes the cubic phase. The term k_x corresponds to the transverse x co-ordinate in the SLM plane and is the transversal K-space wavevector. We now establish that the aperture coefficient is $a_0 = w_0^2 / (4x_0^2)$, where x_0 is the characteristic length and w_0 is the waist of the beam that is incident on the SLM.

We use the free space Huygens integral with the Fresnel approximation² to solve for the initial conditions of the paraxial wave equation. The Huygens-Fresnel integral takes the sum of all the wavelets emanating from a source to determine the total field at a point away from the source. This determines the scalar field, u_x at any distance, z , along the propagation axis of the beam.

$$\begin{aligned}
u_x(x, z) &= \int \sqrt{\frac{ik}{2\pi z}} \exp\left(-i \frac{k}{2z} (x_1^2 - 2x_1x + x^2)\right) u_x(x_1, z=0) dx_1 \\
&= \int \sqrt{\frac{ik}{2\pi z}} \exp\left(-i \frac{k}{2z} (x_1^2 - 2x_1x + x^2)\right) Ai(x_1/x_0) \exp(a_0x_1/x_0) dx_1 \quad (C.10) \\
&= Ai\left(\frac{x - x_m(z)}{x_0} + i \frac{a_0z}{kx_0^2}\right) \exp\left(\frac{a_0(x - x_m(z))}{x_0} - i \frac{z^3}{12k^3x_0^6} + i \frac{a_0^2z}{2kx_0^2} + i \frac{zx}{2kx_0^3}\right)
\end{aligned}$$

The lateral position of the Airy beam is not constant due to the parabolic propagation so the lateral position of the main lobe is described by the coefficient $x_m(z)$, where $x_m(z) = z^2 / (4k^2x_0^3)$.

We now take into consideration the optics involved in the experiment. Using ABCD matrices, we can calculate the scalar field of the beam after it has propagated through a lens. The generalized Huygens-Fresnel integral is shown in Equation C.11. The initial field at position x_1 is denoted by $u_1(x_1)$ and the final field at position x_2 is denoted by $u_2(x_2)$. The values of A, B, C and D are determined by multiplying together, in order, the appropriate matrices representing the optics that the beam propagates through.

$$u_2(x_2) = \int \sqrt{\frac{ik}{2\pi B}} \exp\left(-i \frac{k}{2B} (Ax_1^2 - 2x_1x_2 + Dx_2^2)\right) u_1(x_1) dx_1. \quad (C.11)$$

Since we know that $u_1(x_1) = Ai(x_1/x_0) \exp(a_0x_1/x_0)$, we can put it in to Equation C.11 and determine the final field $u_2(x_2)$ to be

$$\begin{aligned}
u_2(x_2) &= \int \sqrt{\frac{ik}{2\pi B}} \exp\left(-i \frac{k}{2B} (Ax_1^2 - 2x_1x_2 + Dx_2^2)\right) Ai(x_1/x_0) \exp(a_0x_1/x_0) dx_1 \\
&= \frac{1}{\sqrt{A}} Ai\left(\frac{x_2}{Ax_0} - \frac{B^2}{4A^2k^2x_0^4} + i \frac{a_0B}{Akx_0^2}\right) \exp\left(-i \frac{kC}{2A} x_2^2\right) \quad (C.12) \\
&\exp\left(\frac{a_0x_2}{Ax_0} - a_0 \frac{B^2}{2A^2k^2x_0^4} - i \frac{B^3}{12A^3k^3x_0^6} + i \frac{a_0^2B}{2Akx_0^2} + i \frac{Bx_2}{2A^2kx_0^3}\right)
\end{aligned}$$

This result is similar to that found in reference [3].³

C.2 Partially coherent Airy beam propagation

We now use the Gaussian-Schell model⁴ to determine the propagation characteristics of a partially coherent Airy beam. The degree of coherence between transverse points \mathbf{r}_1 and \mathbf{r}_2 in a beam is described by the second order cross spectral density function $W(\mathbf{r}_1, \mathbf{r}_2, z_0)$, where $\mu_\lambda(\mathbf{r}_1 - \mathbf{r}_2) = \exp(-|\mathbf{r}_1 - \mathbf{r}_2|^2 / (2\sigma_\mu^2))$ is the spectral degree of coherence and the spatial coherence length of the beam is σ_μ . The spectral degree of coherence is therefore a Gaussian function with a waist equal to the spatial coherence length and has a value of 1 for a perfectly coherent beam. The spectral density function, Equation C.13, can be used to find the average intensity of a partially coherent beam to be $W(\mathbf{r}, \mathbf{r}, z)$.

$$W(\mathbf{r}_1, \mathbf{r}_2, z_0) = u(x_1, y_1, z_0)u^*(x_2, y_2, z_0)\mu_\lambda(\mathbf{r}_1 - \mathbf{r}_2). \quad (\text{C.13})$$

The scalar field at the SLM with an imposed cubic phase is given by Equation C.14. We can use the second order cross spectral density function with Huygens integral to propagate this scalar field through ABCD matrices, which again represent the optical system.

$$u_0(x, y, 0) = \exp\left(-\frac{(x^2 + y^2)}{w_0^2}\right)\exp\left(ic_0^3\frac{(x^3 + y^3)}{3}\right). \quad (\text{C.14})$$

Here $c_0 = \sqrt[3]{6\varphi/l_h}$, where l_h is the side length of the hologram and φ is the maximal phase shift imposed diagonally across the hologram. We want to propagate the beam through a lens to Fourier transform the above scalar field into an Airy beam. The ABCD matrix for propagating a beam through free space of distance f_{lens} , a lens of focal length f_{lens} and then free space of distance $f_{lens} + z$ is

$$\begin{pmatrix} -z/f_{lens} & f_{lens} \\ -1/f_{lens} & 0 \end{pmatrix} = \begin{pmatrix} 1 & f_{lens} + z \\ 0 & 1 \end{pmatrix} \begin{pmatrix} 1 & 0 \\ -1/f_{lens} & 1 \end{pmatrix} \begin{pmatrix} 1 & f_{lens} \\ 0 & 1 \end{pmatrix}. \quad (\text{C.15})$$

The intensity of the finite Airy beam can be found by integrating the Huygens integral to give

$$\begin{aligned}
I(x, y, z) \propto & \exp\left(2\frac{a_0}{x_0}(x - b_0 z^2)\right) Ai\left(\frac{x - b_0 z^2}{x_0} + \frac{ia_0}{kx_0^2}z + a_0^2\right) \times \\
& Ai\left(j^2\left(\frac{x}{x_0} - b_0 z^2 - \frac{ia_0}{kx_0^2}z + a_0^2\right)\right) \exp\left(2\frac{a_0}{x_0}(y - b_0 z^2)\right) Ai\left(\frac{y - b_0 z^2}{x_0} + \frac{ia_0}{kx_0^2}z + a_0^2\right), \quad (\text{C.16}) \\
& \times Ai\left(j^2\left(\frac{y}{x_0} - b_0 z^2 - \frac{ia_0}{kx_0^2}z + a_0^2\right)\right)
\end{aligned}$$

where $j^3 = -1$, Ai is the Airy function and the parameters b_0 , x_0 and a_0 can be defined as

$$b_0 = \frac{1}{4k^2 x_0^3}, \quad (\text{C.17})$$

$$x_0 = \frac{c_0 f_{lens} \lambda}{2\pi}, \quad (\text{C.18})$$

$$a_0 = \frac{w_0^2 + 2\sigma_\mu^2}{2c_0^2 w_0^2 \sigma_\mu^2}. \quad (\text{C.19})$$

We can see that whilst b_0 and x_0 depend on wavelength, a_0 does not. However, a_0 does depend on the spatial coherence length σ_μ . We can measure the beam quality factor M^2 to determine the spatial coherence of the beam. The equation used to determine the beam quality factor, and the relation between M^2 and σ_μ are

$$M^2 = \frac{\pi w_0^2}{\lambda z_r}, \quad (\text{C.20})$$

$$\sigma_\mu^2 = \frac{w_0^2}{((M^2)^2 - 1)}, \quad (\text{C.21})$$

where w_0 is the beam waist and z_r is the Rayleigh range.

The above theory was determined by Michael Mazilu for comparison with the experimental results that are presented in Chapter 7 and published in Optics Express.¹

References

1. Morris, J. E., Mazilu, M., Baumgartl, J., Cizmar, T. & Dholakia, K. Propagation characteristics of Airy beams: dependence upon spatial coherence and wavelength. *Optics Express* **17**, 13236-13245 (2009).
2. Siegman, A. E. *Lasers* (University Science Books, 1986).
3. Bandres, M. A. & Gutierrez-Vega, J. C. Airy-Gauss beams and their transformation by paraxial optical systems. *Optics Express* **15**, 16719-16728 (2007).
4. He, Q. S., Turunen, J. & Friberg, A. T. Propagation and imaging experiments with Gaussian Schell-Model beams. *Optics Communications* **67**, 245-250 (1988).